HOKKAIDO UNIVERSITY

Title	Study on the microscopic alteration of cementitious materials subjected to high temperature and water action using non-destructive integrated CT-XRD method
Author(s)	髙橋, 駿人
Degree Grantor	北海道大学
Degree Name	博士(工学)
Dissertation Number	甲第13708号
Issue Date	2019-06-28
DOI	https://doi.org/10.14943/doctoral.k13708
Doc URL	https://hdl.handle.net/2115/74975
Type	doctoral thesis
File Information	Hayato_Takahashi.pdf

Hokkaido University Collection of Scholarly and Academic Papers : HUSCAP

Study on the microscopic alteration of cementitious materials subjected to high temperature and water action using non-destructive integrated CT-XRD method

非破壊 CT-XRD 連成法を用いた高温および水の作用を受けたセメント系材料の微視的変質に関する研究

A DISSERTATION

Submitted in partial fulfillment of the requirement for the degree of

Doctor of Engineering
by
HAYATO TAKAHASHI

Laboratory of Environmental Material Engineering
Division of Field Engineering for Environment
Graduate School of Engineering
Hokkaido University
Sapporo, Japan

June 2019

DEDICATION

To

The author’s beloved family

ACKNOWLEDGEMENTS

The author would like to express his heartiest gratitude and appreciation to his supervisor, Professor Takafumi Sugiyama, for his patience, expertise, kindness, enthusiasm, and knowledge. His guidance helped him in all the time of research and writing of this thesis. He had the good fortunate to be able to work with a generous and encouraging supervisor. His constant support provided throughout his study in Hokkaido University proceeds him to the completion of his doctoral dissertation.

His sincerely thanks goes to the members of supervising committee: Professor Hiroshi Yokota, Professor Yoichi Watabe, and Associate Prof. Michael Henry, for their invaluable suggestions and critical comments that helped to refine the scope and content of this work.

The author wishes to acknowledge SPring-8, a large synchrotron radiation facility, lets him use the world leading apparatus, with the approval of the Japan Synchrotron Radiation Research Institute (JASRI) (Proposal Nos. 2012B1281, 2013B1511, 2014A1559, 2014A1782, 2014B1010, 2015A1002, 2015A1682, 2015B1569, 2015B1608, 2016A1133, 2016A1532, 2016B1256, 2017A1009, 2017A1552, 2017A1783, 2017B1021, 2017B1627, 2018A1565, 2018A1691, 2018B1017, 2018B1602). It is the most valuable experience to use the world's largest third generation synchrotron radiation facility throughout this study.

The author also wishes to express his greatest thanks to Dr. Takashi Hitomi, Dr. Kentaro Kajiwara, and their research group for the support of the measurements especially in SPring-8.

To all students and staff of concrete laboratories, Hokkaido University, the author wishes to express his sincere appreciation for friendly and supportive atmosphere that certainly helped him to carry out this study in a pleasant working environment.

The author was adopted as a Japan Society for the Promotion of Science Research Fellowship for Young Scientists from April 2017 to March 2019 and their financial support is gratefully acknowledged (JSPS KAKENHI grant number 17J01145). Thanks to this fund, his life in Ph.D course went smooth and could focus on study without any pressures.

Heartfelt gratitude is extended to Dr. Katsufumi Hashimoto, Dr. Tomoko Fukuyama, Dr. Taito Miura, Dr. Yuya Takahashi, Dr. Kohei Eguchi, Dr. Kentaro Koike, and Dr. Nozomu Someya, because they all gave him many stimulations as a young researcher whenever he met them in many academic conferences. Special thank goes to Dr. Takeru Kanazawa, who was the former Ph.D Japanese student in Hokkaido University and a good role model for me.

Finally, author cannot express his love and appreciation for his family by only words, whose love, support, and sacrifices have encouraged and guided him in all of his pursuits in life. Author would not be here without their all love.

ABSTRACT

One of the durability concerns for concrete structures is the exposure of high temperature like a fire event, which can shorten the service life. In addition, contact with water can also degrade the performance of concrete due to the leaching of calcium. Furthermore, a re-curing method with water for damaged concrete at high temperature can be an option for the recovery of the concrete performance. While the properties of cement pastes mainly account for the durability of concrete, exposure to high temperature and water action causes the alteration in the microstructure of the concrete. Thus, it is important to clarify the mechanisms of thermal decomposition at high temperature and leaching of hydrated cement system. Although research efforts have been made in the past it should be needed to observe the alteration mechanism from the microscopic point of view.

This research aims to investigate the alteration of cementitious materials subjected to high temperatures before and after intrusion of pure water by use of new micro-tomographic method, so-called non-destructive integrated CT-XRD method (hereinafter the CT-XRD). Compared with conventional techniques, this method is significantly beneficial in terms of performing the CT and XRD measurement on the same specimen repeatedly using a synchrotron white X-ray. The X-ray CT method can provide dataset about internal microstructure three-dimensionally, but the distribution of minerals is difficult to evaluate for a hydrated cement system due to the small difference of X-ray absorption characteristics. On the other hand, X-ray diffraction is useful to identify a crystalline mineral. However, this method limits the ability to understand the change of the microstructure of concrete over time because this is a destructive method. In order to solve this problem, the advantage of coupling CT and XRD measurements can be proposed, and thus the development and application have started.

Firstly, experimental works were designed to develop and improve this method. From CT image analysis of mortar samples with different aggregate types, phase segmentation algorithm was developed, which can separate the phases into aggregate, cement paste, and void space including cracking area. This segmentation process is applicable to direct physical simulation. According to XRD measurement, the verification was carried out by comparison with the conventional powder XRD technique. It revealed that the CT-XRD could evaluate the crystals properly with a given limitation for low energy band. In addition, the CT-XRD indicated the advantage that can detect the presence of crystals which cannot be detected after grinding in preparing sample for the conventional powder XRD technique.

Finally, the carbonated cement paste that was heated at 200, 400, 600 and 800 °C followed by immersion in pure water was evaluated by the CT-XRD. The results suggest that sample heated at 400 °C showed the resistance of leaching at most. In addition, rehydration of clinker minerals generated due to heating at 800 °C could be identified although the hydration products were easily dissolved into water. Moreover, the effect of re-curing in water or in air was investigated. Quantitative analysis of crack amount revealed that re-curing of cementitious materials subjected to heating was effective to restrain the crack propagation.

TABLE OF CONTENTS

DEDICATION ……i
ACKNOWLEDGEMENTS ……ii
ABSTRACT ……iii
TABLE OF CONTENTS ……iv
LIST OF TABLES ……vii
LIST OF FIGURES ……viii

CHAPTER 1 INTRODUCTION …… 1

1.1 GENERAL BACKGROUND ……1
1.2 LITERATURE REVIEW ……2
1.2.1 Effect of high temperature on cementitious material ……3
1.2.2 Change of structural performance due to high temperature ……6
1.2.3 Alteration of microstructures in cementitious materials subjected to water action ……8
1.2.4 Spalling mechanism ……9
1.3 RESEARCH OBJECTIVES ……9
1.4 SCOPE OF THIS RESEARCH ……10
1.5 THESIS STRUCTURE ……11
REFERENCES 12

CHAPTER 2 NON-DESTRUCTIVE INTEGRATED CT-XRD METHOD ……18

2.1 INTRODUCTION ……18
2.2 MICROSTRUCTURAL ANALYSIS METHODOLOGY ……18
2.2.1 Physical property analysis ……18
2.2.2 Chemical property analysis ……21
2.3 MOTIVATION TO DEVELOP THE METHOD ……24
2.4 NON-DESTRUCTIVE INTEGRATED CT-XRD METHOD ……25
2.4.1 Facility introduction ……25
2.4.2 Outline of non-destructive integrated CT-XRD method ……26
2.4.3 Details of CT measurement ……27
2.4.4 Details of XRD measurement ……27
2.4.5 Procedure of measurement ……28
2.4.6 Analysis method ……30
2.4.7 Application example ……36
2.5 SUMMARY ……36
REFERENCES 37

CHAPTER 3 IMPROVEMENT OF IMAGE ANALYSIS AND VERIFICATION OF NON-DESTRUCTIVE INTEGRATED CT-XRD METHOD ……42

3.1 INTRODUCTION ……42
3.2 EXPERIMENTAL OUTLINE ……42
3.2.1 Sample preparation ……42
3.2.2 Test procedure ……43
3.2.3 Setup conditions ……43
3.3 IMPROVEMENT OF IMAGE ANALYSIS ……45

3.3.1 Results of CT measurement 45
3.3.2 Results of Phase segmentation 47
3.3.3 Effect of heating on quantitative analysis of crack behavior 57
3.4 VERIFICATION OF THE RESULTS OF XRD 60
3.4.1 XRD target on this study 60
3.4.2 Results of XRD measurement 62
3.4.3 Discussion 67
3.5 SUMMARY 69
REFERENCES 70

CHAPTER 4 EVALUATION OF MICROSCOPIC ALTERATION BY WATER ATTACK 72

4.1 INTRODUCTION 72
4.2 EXPERIMENTAL OUTLINE 72
4.2.1 Sample preparation 73
4.2.2 Test procedure 73
4.2.3 Setup conditions 74
4.3 RESULTS OF CT MEASUREMENT 74
4.3.1 Cross section image 74
4.3.2 Evaluation of damage 75
4.4 RESULTS OF XRD MEASUREMENT 78
4.5 SUMMARY 80
REFERENCES 80

CHAPTER 5 EVALUATION OF MICROSCOPIC ALTERATION SUBJECTED TO HIGH TEMPERATURE AND WATER 82

5.1 INTRODUCTION 82
5.2 EXPERIMENTAL OUTLINE 82
5.2.1 Sample preparation 83
5.2.2 Test procedure 84
5.2.3 Setup conditions 85
5.3 EFFECT OF HEATING DURATION TIME 87
5.3.1 Cross section image 87
5.3.2 Mass loss and shrinkage 88
5.3.3 Results of XRD measurement 89
5.4 EFFECT OF TEMPERATURE BEFORE AND AFTER IMMERSION 90
5.4.1 Cross section image 90
5.4.2 Image processing 92
5.4.3 Evaluation of leaching front 94
5.4.4 Results of XRD measurement 96
5.5 EFFECT OF ENVIRONMENT AFTER HEATING 99
5.5.1 Cross section image 99
5.5.2 Quantitative analysis of crack generation 100
5.5.3 Results of XRD measurement 102
5.6 SUMMARY 104
REFERENCES 104

CHAPTER 6 CONCLUSIONS 106

6.1 GENERAL CONCLUSIONS 106
6.2 RECOMMENDATIONS FOR FUTURE RESEARCH 107

6.2.1 Application of non-destructive integrated CT-XRD method ..……107
6.2.2 Alteration of cementitious materials subjected to high temperature and continuous contact with water ……..……..…107

APPENDIX A IMAGE FILTERING ……....109
APPENDIX B EFFECT OF DURATION TIME OF HEATING ON LEACHING ……....119
APPENDIX C IMPROVEMENT OF CT-XRD SYSTEM ……123
APPENDIX D EFFECT OF AGGREGATE ON CRACK BEHAVIOR BY HEATING 125

LIST OF TABLES

Table 1-1 Chemical hydration formulas of main components
Table 1-2 The list of changes in cementitious materials by high temperature
Table 2-1 Details information of the CT-XRD used in this study
Table 2-2 Composition, notation, density, and linear attenuation coefficient of different phases on cement system
Table 3-1 Details information of the CT-XRD used in these experimental works
Table 3-2 The crystal phase for each sample identified by both P-XRD and the CT-XRD
Table 4-1 Details information of the CT-XRD used in this experimental works
Table 4-2 Volume of extracted crack
Table 5-1 Sample introduction in this experiment
Table 5-2 Details information of the CT-XRD used in these experimental works
Table 5-3 Quantitative results of aggregate and crack

LIST OF FIGURES

Figure 2-1 The photograph of inside the hutch
Figure 2-2 The photograph of the appearance of sample sitting on the stage
Figure 2-3 Schematic diagram of the system for non-destructive integrated CT-XRD method
Figure 2-4 Flowchart of non-destructive integrated CT-XRD method
Figure 2-5 Example of 3D imaging
Figure 2-6 Example of CT histogram of CT images and rescaling to 8bit gray scale images
Figure 2-7 Example of ROI and threshold determination
Figure 2-8 Example of phase segmentation
Figure 2-9 Monitor of simulation software; the way to output theoretical profile
Figure 2-10 Monitor of simulation software; the way to output background subtracted profile
Figure 2-11 Comparison of obtained data with theoretical data
Figure 2-12 Conceptual diagram of the gauge volume
Figure 3-1 Cross Sectional Images: C-400°C
Figure 3-2 Cross Sectional Images: C-600°C
Figure 3-3 Cross Sectional Images: M-400°C
Figure 3-4 Cross Sectional Images: M-600°C
Figure 3-5 Cross Sectional Images: M-800°C
Figure 3-6 Cross Sectional Images: S-400°C
Figure 3-7 Cross Sectional Images: S-600°C
Figure 3-8 Cross Sectional Images: S-800°C
Figure 3-9 XRD profile of each aggregate by temperature
Figure 3-10 CT histogram of the CT images and recalling to 8bit gray scale images
Figure 3-11 Comparison between raw image and binary image
Figure 3-12 Histograms of 600°C series' sample before and after anisotropic diffusion filtering
Figure 3-13 Comparison between filtered image and binary image
Figure 3-14 Effect of filtering (AD: Anisotropic Diffusion, UMS: Unsharp Mask Sharpening)
Figure 3-15 Comparison between filtered image and binary image
Figure 3-16 Binarization targeting aggregate
Figure 3-17 Method for extracting cracking area
Figure 3-18 Result of cluster labeling
Figure 3-19 Method for extracting aggregate for M and S
Figure 3-20 Segmentation procedure proposed in this study
Figure 3-21 3D imaging (green: aggregate, crack: red)
Figure 3-22 Crack width distribution
Figure 3-23 Relationship between aggregate ratio (Ra) and crack ratio (Rc)
Figure 3-24 Relationship between maximum temperature and mean crack width
Figure 3-25 Relationship between maximum temperature and maximum crack width
Figure 3-26 Cross Sectional Image: Non-heat
Figure 3-27 Cross Sectional Image: 200℃
Figure 3-28 Cross Sectional Image: 400℃
Figure 3-29 Cross Sectional Image: 600℃
Figure 3-30 Cross Sectional Image: 800℃
Figure 3-31 XRD profile: Non-heat
Figure 3-32 XRD profile: 200℃
Figure 3-33 XRD profile: 400℃
Figure 3-34 XRD profile: 600℃
Figure 3-35 XRD profile: 800℃
Figure 3-36 XRD profile: each aggregate type
Figure 3-37 Comparison of P-XRD between each aggregate type

Figure 4-1 Flowchart of this experiment
Figure 4-2 Schematic diagram of carbonation test
Figure 4-3 Schematic diagram of water flow test
Figure 4-4 Cross section image for each measurement
Figure 4-5 Example of extracting crack in a given sectional image at initial condition
Figure 4-6 3D images of extracted crack for each measurement
Figure 4-7 XRD profile: Point 1
Figure 4-8 XRD profile: Point 2
Figure 4-9 XRD profile: Point 3
Figure 4-10 XRD profile: Point 4
Figure 5-1 Overview of experimental program
Figure 5-2 Cross sectional image in this experiment
Figure 5-3 Results of mass loss ratio
Figure 5-4 Results of shrinkage
Figure 5-5 XRD profiles in this experiment
Figure 5-6 Cross sectional images at center heights of NH
Figure 5-7 Cross sectional images at center heights of 200℃
Figure 5-8 Cross sectional images at center heights of 400℃
Figure 5-9 Cross sectional images at center heights of 600℃
Figure 5-10 Cross sectional images at center heights of 800℃
Figure 5-11 Histograms of each sample before and after immersion and threshold determination for phase segmentation
Figure 5-12 Schematic diagram of alteration mechanism with calcium leaching
Figure 5-13 Visualization of leaching area: NH
Figure 5-14 Visualization of leaching area: 200℃
Figure 5-15 Visualization of leaching area: 400℃
Figure 5-16 Visualization of leaching area: 600℃
Figure 5-17 Visualization of leaching area: 800℃
Figure 5-18 Leaching front for each sample measured from segmented images
Figure 5-19 XRD profile: NH
Figure 5-20 XRD profile: 200℃
Figure 5-21 XRD profile: 400℃
Figure 5-22 XRD profile: 600℃
Figure 5-23 XRD profile: 800℃
Figure 5-24 Cross sectional images at 1st measurement
Figure 5-25 Cross sectional images at 2nd measurement
Figure 5-26 Cross sectional images at 3rd measurement
Figure 5-27 3D image of the ROI and aggregate and crack
Figure 5-28 XRD profile: Sample A
Figure 5-29 XRD profile: Sample W

CHAPTER 1 INTRODUCTION

1.1 GENERAL BACKGROUND

It is no doubt that concrete is fundamental materials for construction all over the world, which is the secondary resource after water. It can be said that concrete continues to be used in this 21th century, and it is required increasingly to improve the properties of concrete from various points of views, especially durability.

The degree of materials deteriorations depends on how external conditions trigger the damage. One of the concerns during the life cycle is exposure of high temperature like a fire event. Although it can be considered as an extreme accident and the cases are decreasing in the long term, many cases of fire accidents not only in buildings and in civil engineering structures were reported in the world as well as in Japan [1]. In domestic cases, about 40,000 cases occurred, and fire in buildings counted more than 20,000 cases. As for civil engineering infrastructures, cases damaging structures were increasing for the reasons of increase in stock, increase in transportation amount, extension of tunnel itself, and so forth. In recent days, it can be considered that nuclear waste-disposal facilities might be affected by heat from radioactive water at the beginning.

It is expected that concrete is fireproof material, and the legal systems and countermeasures against fire accident were developed in the long history. Recent structures have been, however, going to enlargement, diversification both materially and structurally, extension and so forth, and thus the risks at fire accidents are also diversifying and increasing. Exposure of high temperature surely causes severe deterioration, especially spalling of high strength concrete. Therefore, how to evaluate the performance after exposed to high temperature is important. Moreover, Japan is nowadays facing the population decrease and leveling off construction investment while the existing structures are aging. Hence, the structures are required to prolong its life span and carry out maintenance appropriately. RC structures are generally re-used by repairing damaged area after diagnosis. Therefore, it is expected to improve the quality of survey and diagnosis [2]. To do so, it should be needed to clarify the alteration mechanism properly.

Concrete exposed to high temperatures may suffer a deterioration of its integrity and physical properties due to a variety of physical and chemical reactions. In principal, the damage is caused by mainly three mechanisms; different in thermal characteristics between cement paste and aggregate, effect of pore pressure, and decomposition of cement hydration system. Heating

above 300 °C causes micro cracking to occur and propagate continuously; cracking becomes visible at approximately 400 °C, and then spalling occurs when the temperature is greater than 1200 °C [3]. When temperature is sufficiently high, the physical damage coincides with the decomposition of cement hydration products, leading to a decrease in material strength [4]. Consequently, the damage characteristics of cementitious material in fire problem should be more precisely understood in small scale.

Since the initial properties of cementitious materials vary with mix proportions including the cement content, type of aggregate, additives and so forth, the post-fire material properties should also vary with these factors. Many factors such as external thermal loading conditions and mineral structure of both cement paste and aggregates could affect the fire damage characteristics. Therefore, the main causes of deterioration should be categorized.

While the properties of cement pastes mainly account for the durability of concrete, exposure to high temperature causes the alteration firstly in cement paste, such as moisture transport in pore structures, dehydration of cement pastes, micro-cracking, and so forth. Therefore, it is very important to grasp the effect of the alteration on the change of microstructure and subsequently durability.

On the other hand, in macroscopic viewpoint, concrete is made by adding the coarse aggregate to mortar; therefore, the different in thermal characteristics between mortar and coarse aggregate may introduce the different response of concrete and mortar. Concrete with different types of aggregate could also show different degrees of deterioration in response to fire [5].

Moreover, concrete structures may suffer from high temperature like a fire event during their long service life. However, many research did consider the effect of only high temperature, not multiple effect. For example, carbonation surely occurs during their service life and has an effect on the properties of concrete structures. Moreover, in order to extinguish a fire, water or humid environment is required and leads to further alteration of concrete structures. Therefore, multiple mechanisms should be understood to assess the damage.

1.2 LITERATURE REVIEW

The literature review covers the relevant background information to alteration mechanisms by high temperature and water action. Firstly, cement hydration mechanism is introduced to sort out physical and chemical changes by high temperature; water evaporation, decomposition of hydration products, pore structure and microstructure, and aggregates. Moreover, basic mechanical properties changes are introduced. Then, the effects of alteration due to water were explained. Finally, spalling mechanism is briefly reviewed.

1.2.1 Effect of high temperature on cementitious material

(1) Cement hydration reaction

Ordinary Portland cement is made by heating a mixture of limestone and clay, or other material of similar bulk composition, to a temperature at which partial fusion occurs. The product, which is called clinker, is ground and mixed with a few percent of gypsum ($CaSO_4 \cdot 2H_2O$). The clinker contains four mineral phases: tricalcium silicate (C_3S), β-dicalcium silicate (C_2S), tricalcium aluminate (C_3A), and ferrite (C_4AF). Main components of cement hydration products is calcium silicate hydrate (C-S-H, [C_mSH_n]), portlandite (CH, [$Ca(OH)_2$]), ettringite (AFt, [$C_3A \cdot 3CaSO_4 \cdot 32H_2O$]), and monosulfate (AFm, [$3C_3A \cdot CaSO_4 \cdot 12H_2O$]), which are derived from the reaction formulas shown in Table 1. Gypsum plays a role in retarding flash set because it reacts with calcium aluminates to form either of two practically insoluble complex compounds: calcium aluminate tri-sulfate hydrate and calcium aluminate monosulfate hydrate. Assuming cement paste with a water to cement ratio of 0.5 at curing age of 1 year, volume ratio of each component is calculated as 40% of C-S-H, 10% of CH, 10% of AFm, 10% of unhydrated clinker, and 30% of pore space.

(2) Water evaporation

Free water exists in pore space and becomes water vapor inside concrete. Hence, there is a possibility that this evaporation causes the spalling of concrete. Moreover, the decomposition of cement hydration generates water vapor, which may induce the spalling [7]. It is surely important to grasp the existence of water inside the concrete.

Hydration products lose their free water and physically absorbed water completely. They start to lose their chemically bonded water at 105°C [8]. Capillary water is lost completely at 400°C [9]. Up to 300°C, hydration of unhydrated cement grains is improved due to an internal autoclaving condition derived from the high temperature and evaporation of water inside cement matrix [10].

Table-1.1 Chemical hydration formulas of main components [6]

$C_3A + 3CaSO_4 \cdot 2H_2O + 26H_2O \rightarrow C_3A \cdot 3CaSO_4 \cdot 32H_2O$
$2C_3A + C_3A \cdot 3CaSO_4 \cdot 32H_2O + 4H_2O \rightarrow 3C_3A \cdot CaSO_4 \cdot 12H_2O$
$C_3A + CaSO_4 \cdot 2H_2O + 10H_2O \rightarrow C_3A \cdot CaSO_4 \cdot 12H_2O$
$2C_3S + 7H_2O \rightarrow C_3S_2H_4 + 3Ca(OH)_2$
$2C_3S + 5.3H_2O \rightarrow C_{1.7}SH_4 + 1.3Ca(OH)_2$
$2C_2S + 5H_2O \rightarrow C_3S_2H_4 + Ca(OH)_2$
$C_2S + 4.3H_2O \rightarrow C_{1.7}SH_4 + 0.3Ca(OH)_2$

This is particularly true for high strength concrete as its low permeability resists moisture flow and can be used to explain the constant compressive strength when the temperature is below 300°C [11]. The process of removing water that is chemically bound with cement hydration system is the last to be initiated. The evaporation of water between C-S-H gel sheets strongly affects the mechanical properties of the cement paste [12], because the mechanical properties of cement paste are strongly affected by chemical bonds and cohesion forces between sheets of C-S-H gel.

(3) Decomposition and rehydration of hydration products

As discussed in 1.2.1, the main components of cement hydration products are C-S-H, CH, AFt, and AFm. Many research pointed out that the chemical changes of each cement hydration products are dominant to the maximum temperature. AFt/AFm dehydrates at 110-150 °C [13]. As for CH, Mendes et al. [14] revealed that the critical temperature of its dehydration is 400 °C and chemical bonded water evaporates or CH further converts into C-S-H due to the accelerated pozzolanic reaction at a high temperature [15-17]. The decomposition of CH has no critical influence on the reduction of strength for concrete. However, if concrete was cooled in water after exposure to high temperature, the rehydration of lime will cause a great reduction of strength for concrete due to a considerable expansion will be caused due to such a reaction [18].

The dehydration process of the C-S-H gel reduces its volume, which in turn increases the porosity of the cement matrix. Moreover, during heating, the cement paste experiences a slight expansion up to temperature of approximately 200°C [19] although the intense shrinkage begins as soon as this temperature is exceeded. This significantly contributes to the porosity evolution of the cement paste. Due to heating, total pore volume increases, as does the average pore size. C-S-H starts to decompose structurally at around 560°C [20] and it decomposes into β-C_2S at around 600-700°C [13, 16]. C-S-H (I) decomposes at 800°C, which, however, only results in a slight reduction of strength for concrete [18]. During 580-900°C, decarbonation of carbonates occurs [20]. Moreover, heating the cement paste with a C/S ratio around 1.5 to temperature above 100°C produces several forms of calcium silicates, in general highly porous and weak. When the C/S ratio is close to 1.0 and the temperature is above 150°C, a 1.5 to 1.0 tobemorite gel can form. At temperature between 180°C and 200°C, other silicates such as xonolite and hillebrandite may be formed [9].

Recently, microstructural changes of heated cement pastes have been studied by neutron diffraction [21]. This research demonstrates the temperature at which the main products of hydration of Portland cement, including portlandite, ettringite, calcite, lime, larnite, and C-S-H gel, are present. During heating, ettringite decomposes first, even before the temperature reaches 100 °C; The C-S-H gel slightly decreases as it gets hydrated and disappears at temperature

around 450 °C and contributes to increase the concentration of calcite and larnite. In addition, this indicated that uptake of water vapour from the atmosphere takes place to form portlandite from generated lime while AFt and C-S-H gel are not recovered during cooling.
Moreover, re-curing fire-damaged concrete in water or a high humidity environment can lead to performance recovery and it is suggested that water supply on fire damaged concrete is an environmental and economic procedure to recover its strength because of rehydration of calcium hydroxide [22, 23]. On the other hand, it is concerned that volume increase with the reaction may reduce performance due to the expansion of cracks [24, 25]; therefore, the effect of re-curing is still unclear.

(4) Change of pore structure and microstructure
As a result of the water evaporation and chemical changes of hydration products, elevation of temperature increases porosity and pore size of cement and concrete [26-29]. This is fundamentally derived from the decomposition of cement hydration systems, as explained in previous section. However, the effect of aggregate is also not negligible because thermal mismatch may take place cracking in interfacial transition zone (ITZ). The coarsening of the pore structure is mainly responsible for the reduction of the mechanical properties. Up to 200°C, no micro-cracks are observed in either hardened cement matrix or ITZ [30]. When the temperature rises to 400°C, micro-cracks in cement matrix and ITZ start to propagate, and their intensity increases with temperature increase [31, 32]. It is considered that the different thermal strains for hardened cement matrix and aggregates have resulted in the development of the micro-cracks at high temperature. With the increase of temperature, the hardened cement matrix expands until 100°C and then starts to shrink itself as a result of the loss of water, while aggregates keep expansion during the whole heating. Similar results have also been found by Ref. [33]. Such different strains will produce a stress between cement matrix and aggregates, causing micro-cracks in the ITZ. This is also responsible for the reduction of the mechanical properties of concrete at high temperatures. When temperature is very high, such as above 1000°C, porosity and microstructure of concrete are smaller and better than those at a lower temperature due to concrete has been sintered at such a high temperature [34]. However, it does not indicate that the mechanical properties of concrete at the very high temperature was better than those at a lower temperature as the relationship between mechanical properties and pore structure is not true any further due to the fact that sintering has changes the characteristic of concrete material [34].

(5) Effect of aggregates
Ref. [35] indicated that calcareous aggregates' thermal expansion seems to increase at around

350 ℃ and discontinuity of expansion rate can be observed, which happens at around 550 ℃. Below 300 ℃, siliceous aggregates' thermal expansion is generally more important than calcareous' one. Besides the difference of expansion and shrinkage behavior between aggregate and cement matrix, the alteration of aggregate itself causes deterioration. At around 573 ℃, siliceous aggregates transform α-phase to β-phase and subsequently cause expansion of concrete [36]. Disintegration of calcareous aggregates, such as limestone, occurs at a high temperature above 600 ℃ [37], which leads to coarsen its structure followed by deterioration.

The above mentioned in Section 1.2.1 can be summarized briefly in Table 1-2.

1.2.2 Change of structural performance due to high temperature

(1) Compressive strength

It is unavoidable that there is a reduction for compressive strength of concrete when it is exposed to high temperature. In spite of concrete mixture proportions, test modalities, such as

Table-1.2 The list of changes in cementitious materials by high temperature [9]

Temp. range	Chemical changes
20-200℃	Slow capillary water loss and reduction in cohesive forces as water expands; 80-150℃ ettringite dehydration; C-S-H gel dehydration; 150-170℃ gypsum decomposition; Physically bound water loss;
300-400℃	Approx. 350℃ break up of some silicieous aggregates (flint); 374℃ critical temperature of water
400-500℃	460-540℃ Portlandite decomposition $Ca(OH)_2 \rightarrow CaO+H_2O$;
500-600℃	573℃ quartz phase change β→α in aggregates and sands;
600-800℃	Second phase of the C-S-H decomposition and sands;
800-1000℃	930-960℃ calcite decomposition CaCO3→CaO+CO2, carbon dioxide release; ceramic binding initiation which replaces hydraulic bonds;
1000-1200℃	1050℃ basalt melting;
1300℃	Total decomposition of concrete, melting;

specimen size, stressed/unstressed conditions and hot/residual states, also influence the mechanical properties of concrete at high temperature. Chan et al. [38] carried out the test up to 1200 °C using normal (NSC) and high strength concrete (HSC) specimens. This demonstrates that the mechanical strength of HSC decreases in a similar manner to that of NSC except in the range of 20-400 °C. Ergun et al. [39] also indicated that significant strength loss could be identified more than 400 °C. Husem [40] pointed out that not only the heating but also cooling type affects the residual compressive strength. In case of using blended cement, such as fly ash, silica fume, similar trend to ordinary Portland cement was significant [41-44]. Netinger et al. [45] investigated the effect of high temperatures up to 1000 °C on concretes made with different types of aggregates. It revealed that some types of aggregate exhibits more significant fire resistance than river aggregate, but above 800 °C, compressive strength of almost all types of concrete reduced to less than 10MPa.

(2) Flexural strength, splitting tensile strength and elastic modulus

Residual flexural strength, residual splitting tensile and residual modulus of elasticity of concrete after the exposure to elevated temperatures was also tested in many past studies, respectively. Similar to the compressive strength reviewed in the previous section, flexural strength, splitting tensile strength and modulus of elasticity of concrete decreases with the increase of temperature, but at a nearly linear rate. Ref. [46] discussed the comparison of tensile strength after exposure of high temperature up to 1200 °C between high strength and normal strength concrete. This demonstrated the reduction rate of its strength is larger than that of compressive strength. In Ref. [47], residual mechanical properties of fiber-reinforced high-performance concrete after exposure to high temperature ranged from 200 to 800° C were tested, which resulted in that tensile strength decreased by about 50 % at 400 °C, by almost all zero at 800 °C. Ref. [48] suggested that the reductions in flexural strength were lower in steel fiber reinforced concrete than in plain concrete. The effectiveness of steel fibers was suggested as the bridging cracks induced upon tensile loading and melting themselves after heating [49].

(3) Stress-strain relationship

Stress-strain relationship of concrete at elevated temperatures has been investigated by many researchers. Ref [50] has been found that with the increase of temperature, stress-strain curves become flatter at 600 and 700 °C, and the peak stress shifts downwards and rightwards. Yoda et al. [51] reported that as temperature increases, the strain to stress gets larger and the gradient smaller. On the other hand, Huo et al. [52] indicated that no obvious effects of temperature and strain rate on the shape of ascending branches of normalized stress versus strain curves were found. Fu et al. [53] carried out the heating experiment under loading conditions. It

demonstrates that loading state affects the strength and elasticity and then strain to stress becomes smaller than non-loading state.

1.2.3 Alteration of microstructures in cementitious materials subjected to water action

(1) Leaching behavior

One of the deterioration of concrete in contact with water is calcium leaching, which makes the cement porous due to dissolution of the hydration product and leads to decrease not only the microscopic but macroscopic stability [54]. The speed of this process is very slow and the scale is in microscale. However, nowadays it can be said that concrete is the potential material for the use of high-level nuclear waste disposal facility and its service life is expected to exceed over 10,000 years. Therefore, the long-term stability of a radioactive waste repository should be needed and thus this phenomena is not negligible to satisfy the necessary safety level. Therefore, in recent days, more research efforts were carried out to simulate the models with high accuracy.

(2) Phenomenon of leaching

Tsuji et al. [55] pointed out the leaching behavior and change of phase. At first, sodium and potassium ion is leached to surface. Then, calcium hydroxide is dissolved into pore solution followed by diffusion of calcium ion and hydroxide ion to surface. Moreover, dissolution of calcium silicate hydrate to pore solution occurs followed by dissolution of calcium ion and hydroxide ion to surface. Finally, dissolution of SiO_2 occurs.

Therefore, alteration mechanism is divided into two process; dissolution and transportation. These processes have an effect on the reduction of pore volume and subsequently properties of concrete such as strength, permeability, pH, and so forth. Based on these process, many researchers constructed the dissolution-alteration modeling (i.e. [56]).

(3) Evaluation methodologies

One important factor is to estimate the depth of dissolution front as precisely as possible. The other factor is to predict the degraded region in the hydrated cement system due to water attack accurately. Thus, it should be needed to develop accurate methodologies. In previous experimental works, many methodologies were applied to observe the phenomena. However, conventional techniques permit the detectable order of measurement for dissolution front ranges only from 1 to 10 mm in precision at most and limits to one dimensional observation. Even if electron probe X-ray micro-anlayzer (EPMA) which allows us to measure the specimen on the order of 0.1mm was used, only the profile of atoms can be identified [57]. Moreover, in other conventional techniques to measure the degrading region, the specimen must be destroyed during experimental program. The mercury intrusion porosimetry measurement is a good

method for pore structure evaluation due to its large range of pore size measurement and easy to operate. However, MIP measurement cannot provide a true pore size distribution of pore structure because it does not measure pore size but pore entry size [58].

1.2.4 Spalling mechanism

Spalling may occur at high temperature, which will greatly reduce mechanical properties of concrete structure and even cause collapse of the structure. The mechanism of spalling of concrete at high temperature could be mainly explained from two mechanisms; thermo-mechanical process and thermo-hygral process [59]. The former process can be explained that the heating of a concrete element involves high temperature gradients. These gradients can be very important in the case of a rapid heating (e.g. for a fire) and induce high compressive stresses close to the heated surface. These stresses can locally overtake the concrete strength and cause the ejection of pieces [60]. The latter is proposed that the heating of a concrete element involves mass transport into the porous medium. Fluids that are present into concrete (free water, water vapor, and dry air) are moving due to pressure and molar concentration gradients. Particularly, fluids are moving through the inner zones of concrete. Since these zones are colder, water vapor starts to condensate and a “moisture clog” is gradually created close to the heated surface. This clog is assumed to be a region of concrete with high water content. Since this clog acts like a real barrier to fluid’s flow, pore pressures are increasing. These pressures can locally overtake the tensile strength of concrete and initiate the spalling [61]. These two mechanisms are mainly focused on the causes of spalling. Recently, spalling occurs due to the multiple influences. Fu et al. [62] concluded that thermal stress induced cracking parallel to heating surface followed by condensation of moisture. Additional heating causes spalling due to the water vapor pressure. To prevent the explosive spalling, adding polypropylene fibers is useful method because it can reduce the internal water vapor pressure due to their melting and generating new pores and cracks [63].

1.3 RESEARCH OBJECTIVES

The key objective of this research is to understand how exposure of fire to cementitious materials has effects on the crack propagation and alteration in microscopic viewpoint. It is already known that the decomposition of cement hydrate is dependent on the temperature during heating. Therefore, chemical analysis like ignition loss, TG-DTA was utilized to quantify cement hydrate as macroscopic analysis. However, these methodologies are destructive and there are few discussions on changes of cement hydrate after exposure of high temperature in

microscopic viewpoint. In addition, there still exists a lack of studies of microscopic changes in sample including aggregates.

To solve these problems, utilization of X-ray is useful to grasp the internal structure in a non-destructive manner. X-ray Computed Tomography (CT) is useful to analyze internal microstructure three-dimensionally and recently utilized by various researches in cement and concrete field. However, it is difficult to detect the distribution of minerals in a cement hydrated system even using a synchrotron radiation X-ray source. It derives from small differences in the linear attenuation coefficient of minerals in a cement hydrated system, which result in acquisition of CT images with lower contrast. Moreover, phase segmentation of concrete from X-ray images is still challenging because general aggregates and cement paste have similar X-ray attenuation coefficient. Therefore, many image analyses are required to obtain the morphology of concrete [64]. X-ray diffraction method was conventionally utilized to identify the cement hydration system before and after heating. This methodology, however, limits the ability to understand the change of microstructure over time and consider properly the internal state of concrete like moisture due to grind process.

Our research group found out the advantage of coupling CT and XRD measurement and started the development and application of non-destructive integrated CT-XRD method [65] (Hereafter the CT-XRD, and details are explained in Chapter 2.). Then, this method clarified the leaching behavior in vicinity of crack of cementitious materials due to water flow [66], and this led to the motivation to apply the alteration behavior due to high temperature followed by water action.

1.4 SCOPE OF THIS RESEARCH

Scopes of this research are put emphasis on following four points.

1) Further development of non-destructive integrated CT-XRD method for extensive applications of research on cement and concrete field
2) Specification of the difference of crack distribution and identification of minerals in aggregate and cement paste subjected to high temperature
3) Investigation of effect of maximum temperature and duration time on alteration mechanism subjected to high temperature
4) Investigation of multiple degradation on carbonated cement paste before and after heating and water immersion

According to 1), although this new methodology applied and clarified the leaching behavior due

to water flow, there are many rooms for its improvements. For example, the segmentation procedures should be established to obtain accurate morphological descriptions, which can provide accurate physical simulations. Furthermore, in terms of XRD measurement, the verification by comparison with conventional techniques has never been carried out yet. Therefore, some samples were measured in CT-XRD, followed by grinding the same samples and carrying out Powder XRD. Then, the obtained results were discussed in this research.

With regards to 2), the presence or absence of aggregate should have effects on crack propagation. However, these behaviors hardly have been observed in micro scale and the effect of aggregate types should be discussed. These results will be surely effective.

In terms of 3), previous research often concerns the effect of maximum temperature on alteration mechanism. However, the effect of duration time was not enough discussed. Moreover, the CT-XRD has never applied to the cementitious materials subjected to high temperature. These findings from microscopic viewpoint make the alteration mechanisms clearer.

As for 4), while concrete structures may suffer from high temperature like a fire event during their long service life, many research did not considered the effect of carbonation. Carbonation is mechanically beneficial by clogging the bigger capillary pores and refining microstructure [65]. This should surely affect the properties of concrete after exposure of high temperature followed by water penetration. Therefore, this point was discussed by the results in this research.

1.5 THESIS STRUCTURE

In order to meet the objectives presented in this chapter, it is clear that this thesis would need to be divided into six chapters including this chapter. This chapter, Chapter 1, explains an overview of the issues and literature reviews of the topics related to this research, which contains the alteration mechanism and reduction of mechanical properties by high temperature, alteration mechanism subjected to water action, and spalling mechanism. Then, the advantage of application of X-ray for this research are introduced. Finally, the research objectives and scope and this outline are introduced. Chapter 2 introduces an overview of non-destructive integrated CT-XRD method, main observation methodology in this research. Firstly, conventional techniques for the analysis of microstructure of cementitious materials were explained. Then, their problems were discussed and why this unique method was started to develop followed by explanation of the outline. Finally, brief literature reviews using this methodology are described. Chapter 3 focuses on the development of non-destructive integrated CT-XRD method for analysis of cementitious materials including image analysis for further application of research

on cement and concrete research. This chapter consists of two parts; one is to introduce image analysis procedure including phase segmentation and quantitative analysis, and the other is to verify the XRD profiles of the CT-XRD by comparison with conventional powder XRD analysis. Chapter 4 discusses the evaluation of microscopic alteration by subjected to water attack using deteriorated mortar. This chapter indicated the effect of water flow on interface between aggregate and cement paste. In Chapter 5, the microscopic alteration of the carbonated cement paste that was heated at various temperatures followed by immersion in pure water was evaluated. This chapter also discussed the effect of heating duration time on decomposition mechanisms and the effect of re-curing and leaching by continuous the CT-XRD measurement. Chapter 6 summarizes the conclusions from experimental results of this research. Finally, this makes recommendations for future research works.

REFERENCES

[1] Fire and Disaster Management Agency. (2017). “White Paper on Fire Service.” [in Japanese]

[2] Japan Concrete Institute. (2017) “Report of technical committee on evaluating performance of concrete under high temperature condition.” [in Japanese]

[3] Arioz, O. (2007) “Effects of elevated temperature on properties of concrete,” *Fire Safety Journal*, 42, 516-522.

[4] Djaknoun, S., Ouedraogo, E., and Benyahia, A. A. (2012) “Characterisation of the behavior of high performance mortar subjected to high temperature,” *Construction and Building Materials*, 28, 176-186.

[5] Hertz, K. D. (2003) “Limits of spalling of fire-exposed concrete,” *Fire Safety Journal*, 38(2), 103-116.

[6] Japan Cement Association. (2001). “Report of committee on properties and microstructure of hardened cement.” [in Japanese]

[7] Ko, J., Noguchi, T., and Ryu, D. (2011). “The spalling mechanism of high-strength concrete under fire.” *Magazine of Concrete Research*, 63(5), 357-370.

[8] Feldman, R. F., and Ramachandran V. S. (1971). “Differentiation of interlayer and adsorbed water in hydrated Portland cement on thermal analysis.” *Cement and Concrete Research*, 26(5), 607-620.

[9] Hager, I. (2013). “Behavior of cement concrete at high temperature.” *Bulletin of the Polish Academy of Sciences*, 61(1), 145-154.

[10] Saad, M., Abo-El-Enein, Hanna, G. B., and Kotkata, M. F. (1996). “Effect of temperature on physical and mechanical properties of concrete containing silica fume.” *Cement and*

Concrete Research, 26(5), 669-675.

[11] Ma, Q., Guo, R., Zhao, Z., Lin, Z., and He, K. (2015). "Mechanical properties of concrete at high temperature – A review." *Construction and Building Materials*, 93, 371-383.

[12] Feldman, R. F., and Sereda, P. J. (1968). "A model for hydrated Portland cement pastes as deduced from sorption-length change and mechanical properties." *Materials and Structures*, 1(6), 509-519

[13] Taylor, H. F. W. (1997). "Cement Chemistry 2nd edition." *Thomas Telford*.

[14] Mendes, A., Sanjayan, J. G., Gates, W. P., and Collins, F. (2012). "The influence of water absorption and porosity on the deterioration of cement paste and concrete exposed to elevated temperatures, as in a fire event." *Cement and Concrete Composite*, 34(9), 1067-1074.

[15] Piasta, J., Sawicz, Z., Rudzinski, L. (1984). "Changes in the structure of hardened cement paste due to high temperature." *Materials and Constructions*, 17(4), 291-296.

[16] Peng, G-F., and Huang, Z-S. (2008) "Change in microstructure of hardened cement paste subjected to elevated temperature." *Construction and Building Materials*, 22(4), 593-599.

[17] Ibrahim, R. K., Hamid, R., and Taha, M. R., (2012). "Fire resistance of high-volume fly ash mortars with nanosilica addition." *Construction and Building Materials*, 36, 779-786.

[18] Lin, W-M., Lin, T. D., and Powers-Couche, L. J. (1996). "Microstructures of fire-damaged concrete." *ACI Materials Journal*, 93(3), 199-205.

[19] Piasta, J. (1984). "Heat deformations of cement paste phases and the microstructure of cement paste." *Materials and Constructions*, 17(6), 415-420.

[20] Vydra, V., Voda´k, F., Kapic˘kova´, O., and Hos˘kova, S˘. (2001). "Effect of temperature on porosity of concrete for nuclear-safety structures." *Cement and Concrete Research*, 31(7), 1023-1026.

[21] Castellote, M., Alonso, C., Andrade, C., Turrillas, X., and Campo, J. (2004). "Composition and microstructural changes of cement pastes upon heating, as studied by neutron diffraction." *Cement and Concrete Research*, 34(9), 1633-1644.

[22] Poon, C., Azhar, S., Anson, M., and Wong, Y. L. (2001) "Comparison of the strength and durability performance of normal and high strength pozzolanic concretes at elevated temperatures." *Cement and Concrete Research*, 31(9), 291-300.

[23] Lin, Y., Hsiao, C., Yang, H., and Lin, Y. F. (2011). "The effect of post-fire-curing on strength-velocity relationship for nondestructive assessment of fire-damaged concrete strength." *Fire Safety Journal*, 46(4), 178-185.

[24] Lin, W-M., Lin, T. D., and Powers-Couche, L. J. (1996) "Effect of fire-damaged concrete." *ACI Materials Journal*, 93(3), 199-205.

[25] Henry, M., Hashimoto, K., Darma, I. S., and Sugiyama, T. (2016). "Cracking and chemical composition of cement paste subjected to heating and water re-curing." *Journal of Advanced*

Concrete Technology, 14(4), 134-143.

[26] Hossain, K. M. A. (2006). "High strength blended cement concrete incorporating volcanic ash: Performance at high temperatures." *Cement and Concrete Composites*, 28(6), 535-545.

[27] Rostasy, F. S., Weiss, R. und Wiedemann, G. (1980). "Changes of pore structure of cement mortar due to temperatures." *Cement and Concrete Research*, 10(2), 157-164.

[28] Poon, C-S., Azhar, S., Anson, M., Wong, Y-L. (2001). "Comparison of the strength and durability performance of normal- and high-strength pozzolanic concretes at elevated temperatures." *Cement and Concrete Research*, 31(9), 1291-1300.

[29] Mendes, A., Sanjayan, J. G., Gates, W. P., and Collins, F. (2012). "The influence of water absorption and porosity on the deterioration of cement paste and concrete exposed to elevated temperatures, as in a fire event." *Cement and Concrete Composites*, 34(9), 1067-1074.

[30] Li, X. J., Li, Z. J., Onofrei, M., Ballivy, G., and Khayat, K. H. (1999). "Microstructural characteristics of HPC under different thermo-mechanical and thermo-hydraulic conditions." *Material and Structures*, 32(10), 727-733.

[31] Handoo, S. K., Agarwal, S., Agarwal, S. K. (2002). "Physicochemical, mineralogical, and morphological characteristics of concrete exposed to elevated temperatures." *Cement and Concrete Research*, 32(7), 1009-1018.

[32] Wang, X. S., Wu, B-S., and Wang, Q-Y. (2005). "Online SEM investigation of microcrack characteristics of concretes at various temperatures." *Cement and Concrete Research*, 35(7), 1385-1390.

[33] Fu, Y-F., Wong, Y-L., Poon, C-S., Tang, C-A., and Lin, P. (2004). "Experimental study of micro/macro crack development and stress-strain relations of cement-based composites materials at elevated temperatures." *Cement and Concrete Research*, 34(5), 789-797.

[34] Chan, S. Y. N., Luo, X., and Sun, W. (2000). "Effect of high temperature and cooling regimes on the compressive strength and pore properties of high performance concrete." *Construction and Building Materials*, 14(5), 261-266.

[35] Robert, F., and Colina, H. (2009). "The influence of aggregates on the mechanical characteristics of concrete exposed to fire." Magazine of Concrete Research, 61(5), 311-321.

[36] Khoury, G. A. (1992). "Compressive strength of concrete at high temperatures: reassessment." *Magazine of Concrete Research*, 44(161), 291-309.

[37] Schneider, U., Diederichs, U., and Ehm, C. (1981). "Effect of temperature on steel and concrete for PCRV's." Nuclear Engineering and Design, 67(2), 245-258.

[38] Chan, Y. N., Peng, G. F., and Anson, M. (2013). "Residual strength and pore structure of high-strength concrete and normal strength concrete after exposure to high temperatures." *Cement and Concrete Composites*, 21(1), 23-27

[39] Ergun, A., Kurklu, G., Baspinar, M. S., and Mansour, M. Y. (2013). "The effect of cement

dosage on mechanical properties of concrete exposed to high temperatures." *Fire Safety Journal*, 55, 160-167.

[40] Husem, M. (2006). "The effects of high temperature on compressive and flexural strengths of ordinary and high-performance concrete." *Fire Safety Journal*, 41(2), 155-163.

[41] Savva, A., Manita, P., and Sideris, K. K. (2005). "Influence of elevated temperatures on the mechanical properties of blended cement concretes prepared with limestone and siliceous aggregates." *Cement and Concrete Composites*, 27(2), 239-248.

[42] Sancak, E., Sari, Y. D., and Simsek, O. (2008). "Effects of elevated temperature on compressive strength and weight loss of the light-weight concrete with silica fume and superplasticizer." Cement and Concrete Composites, 30(8), 715-721.

[43] Demirel, B., and Kelestemur, O. (2010). "Effect of elevated temperature on the mechanical properties of concrete produced with finely ground pumice and silica fume." *Fire Safety Journal*, 45(6-8), 385-391.

[44] Li, Q., Li, Z., and Yuan, G. (2012). "Effects of elevated temperatures on properties of concrete containing ground granulated blast furnace slag as cementitious material." *Construction and Building Materials*, 35, 687-692.

[45] Netinger, I., Kesegic, I., and Guljas, I. (2011). "The effect of high temperatures on the mechanical properties of concrete made with different types of aggregates." *Fire Safety Journal*, 46(77), 425-430.

[46] Chan, S. Y. N., Peng, G-F., and Chan, J. K. W. (1996). "Comparison between high strength concrete and normal strength concrete subjected to high temperature." *Materials and Structures*, 29(10), 616-619.

[47] Peng, G-F., Yang, W-W., Zhao, J., Liu, Y-F., Bian, S-H., and Zhao, L-H. (2006). "Explosive spalling and residual mechanical properties of fiber-toughened high-performance concrete subjected to high temperatures." *Cement and Concrete Research*, 36(4), 723-727.

[48] Giaccio, G. M., and Zerbino, R. L. (2005). "Mechanical behaviour of thermally damaged high-strength steel fibre reinforced concrete." Materials and Structures, 38(3), 335-342.

[49] Suhaendi, S. L., and Horiguchi, T. (2006). "Effect of short fibers on residual permeability and mechanical properties of hybrid fibre reinforced high strength concrete after heat exposition." Cement and Concrete Research, 36(9), 1672-1678

[50] Chang, Y. F., Chen, Y. H., Sheu, M. S., and Yao, G. C. (2006). "Residual stress-strain relationship for concrete after exposure to high temperatures." *Cement and Concrete Research*, 36(10), 1999-2005.

[51] Yoda, Y., Imamoto, K., and Kiyohara, C. (2014). "Pore structure and creep characteristics subjected to elevated temperature." *Proceedings of the Japan Concrete Institute*, 36(1), 772-777. [in Japanese]

[52] Huo, J. S., He, Y. M., and Xiao, L. P., and Chen, B. S. (2013). "Experimental study on dynamic behaviours of concrete after exposure to high temperatures up to 700°C." Materials and Strucutres, 46(1-2), 255-265.

[53] Fu, Y. F., Wong, Y. L., Poon, C. S., and Tang, C. A. (2005). "Stress-strain behavior of high-strength concrete at elevated temperatures." *Magazine of Concrete Research*, 57(9), 535-544.

[54] Carde, C., Francois, R., and Torrenti, J-M. (1996). "Leaching of both calcium hydroxide and C-S-H from cement paste: modeling the mechanical behavior." *Cement and Concrete Research*, 26(8), 1257-1268.

[55] Tsuji, Y., Nakarai, K., Haga, K., and Sakamoto, H. (2016). "Leaching modeling and evolution of pH in cementitious materials of radioactive waste repository facilities." *Concrete Journal*, 54(4), 345-352. [in Japanese]

[56] Sugiyama, T., Ritthichauy, W., and Tsuji, Y. (2003). "Simultaneous transport of chloride and calcium ions in hydrated cement systems." *Journal of Advanced Concrete Technology*, 1(2), 127-138.

[57] Haga, K., Shibata, M., Hironaga, M., Tanaka, S., and Nagasaki, S. (2005). "Change in pore structure and composition of hardened cement paste during the process of dissolution." *Cement and Concrete Research*, 35(5), 943-950.

[58] Diamond, S. (2000). "Mercury porosimetry: An inappropriate method for the measurement of pore size distributions in cement-based materials." *Cement and Concrete Research*, 30(10), 1517-1525.

[59] Mindeguia, J-C., Pimienta, P., Noumowe, A., and Kanema, M. (2010). "Temperature, pore pressure and mass variation of concrete subjected to high temperature – Experimental and numerical discussion on spalling risk." *Cement and Concrete Research*, 40(3), 477-487.

[60] Ozawa, M., Uchida, S., Kamada, T., and Morimoto, H. (2012). "Study of mechanisms of explosive spalling in high-strength concrete at high temperatures using acoustic emission." *Construction and Building Materials*, 37, 357-370.

[61] Kalifa, P., Menneteau, F-D., and Quenard, D. (2000). "Spalling and pore pressure in HPC at high temperatures." *Cement and Concrete Research*, 30(10), 1999-2005.

[62] Fu, Y. F., Wong, Y. L., Poon, C. S., and Tang, C. A. (2007). "Numerical tests of thermal cracking induced by temperature gradient in cement-based composites under thermal loads." *Cement and Concrete Research*, 29(2), 103-116.

[63] Yermak, N., Pilya, P., Beaucour, A-L., Simon, A., and Noumowe, A. (2017). "Influence of steel and/or polypropylenes fibres on the behavior of concrete at high temperature: Spalling, transfer and mechanical properties." Construction and Building Materials, 132, 240-250.

[64] Stamati, O., Roubin, E., Andò, E., and Malecot, Y. (2018) "Phase segmentation of concrete

x-ray tomographic images at meso-scale: Validation with neutron tomography," *Cement and Concrete Composites*, 88, 8-16.

[65] Sugyiama, T., Hitomi, T., and Kajiwara, K. (2014). "Nondestructive integrated CT-XRD method for research on hydrated cement system." *Proceedings of the 4th International Conference on the Durability of Concrete Structures*, 298-303.

[66] Takahashi, H., and Sugiyama, T. (2016). "Investigation of alteration of deteriorated mortar due to water attack using non-destructive integrated CT-XRD method." *Proceedings of the 11th fib International Ph.D Symposium in Civil Engineering*, 445-452.

[67] Pihlajavaraara, S. E. (1968). "Some results of the effect of carbonation on the porosity and pore size distribution of cement paste." *Materials and Constructions*, 1(6), 521-527.

Chapter 2 NON-DESTRUCTIVE INTEGRATED CT-XRD METHOD

2.1 INTRODUCTION

This chapter explains about the details of non-destructive integrated CT-XRD method. At first, conventional techniques which were used to study microstructural of cementitious materials in previous research works are introduced. Then, the history of development of non-destructive integrated CT-XRD method was explained with facility introduction. Finally, examples of application of non-destructive integrated CT-XRD method was introduced.

2.2 MICROSTRUCTURAL ANALYSIS METHODOLOGY

2.2.1 Physical property analysis

(1) Porosimetry

The microstructure of cementitious materials mainly accounts for the durability. This property can be evaluated as various methods. For example, mercury intrusion porosimetry (MIP) is applied to evaluate pore size distributions in cement matrix [1, 2]. However, many references suggested that accurate pore size distributions are not provided by MIP because there exists the lack of direct accessibility of most of the pore volume to the mercury surrounding the specimen. Therefore, some substituting method was proposed. For example, substituting Wood's metal for mercury as the intruding liquid is useful. The large pores and/or the ink-bottle type pores may be selectively filled with this metal because Wood's metal can be intruded above its melting temperature and solidified by lowering temperature [3]. Nitrogen sorption does, at least in adsorption, not suffer from the ink-bottle effect, but the analysis of larger pores (radius > 50 nm) suffers from limitations of resolution. Moreover, it should be needed to pay attention to drying method because it may collapse the fine structure [4].

(2) Nuclear magnetic resonance

Solid-state nuclear magnetic resonance (NMR) spectroscopy represents an important research tool for the characterization and structural analysis of cement pastes and cement-based materials and has been increasingly employed in this field for more than the paste 3 decades. A main advantage of the method is nuclear –spin selectivity, where one nuclear-spin isotope of the NMR periodic table (e.g. ^{1}H, ^{11}B, ^{19}F, ^{27}Al and ^{29}Si) is detected at the time, which often results

in rather simple but informative spectra for complex multiphase systems, such as cementitious materials. In addition, resonances from these spin nuclei are most sensitive to local structural ordering and/or dynamic effects, which permits studies of no only crystalline phases but also amorphous components, such as the calcium-silicate hydrate (C-S-H) phase, produced during the setting and hardening of Portland cement. Thus, NMR complements a number of other analytical techniques which probe the long-range order of crystalline phases (e.g. X-ray diffraction) or bulk chemical features. Recently, ^{29}Si magic-angle spinning (MAS) was utilized to study the amorphous C-S-H phase produced by Portland cement hydration by checking 29Si chemical shifts for silicates reflect the degree of condensation of SiO_4 tetrahedra in studies of zeolites and aluminosilicate minerals [5]. This relationship was also found for calcium silicates [6], and the amorphous C-S-H phase produced by Portland cement hydration [7]. More recently, ^{1}H-NMR relaxometry have been further developed for studies of solid and mobile water in hardened cement systems, providing new knowledge about porosity, pore sizes, pore connectivities and water diffusion [8, 9].

(3) X-ray CT

X-ray CT provides one of the most accurate methods of examining the internal structure of an object in three dimensions without upsetting the properties of a damaged sample. Each image that results from an X-ray CT scan consists of a 3D field of voxels. Each voxel is assigned a different grey-scale brightness which is dependent on its X-ray attenuation level called as linear attenuation coefficient (LAC). A material has unique value of LAC. Therefore, the determination of thresholds has the potential to define specific materials, such as cement paste, aggregates, void and so forth. In addition, the quantitative evaluation can be carried out by combination with image analysis techniques.

In cement and concrete field, Landis et al. [10] is one of the leading groups and has applied to observe the internal cracking patterns of a series of small mortar specimens, which revealed that three-dimensional renderings qualitatively illustrate features of internal cracking such as the effects of different microstructural features. Promentilla et al. characterized the propagation of cracks in mortars that were exposed to freezing-thawing action [11]. Ivan et al. [12] used cesium carbonate as a tracer in-situ diffusion test with the aid of X-ray CT to measure the 3D crack geometry and tracer diffusivity. In recent years, as the performance of apparatus increased, the target of observation expanded to reinforced concrete. The authors applied X-ray CT scanning to reinforced mortar induced crack followed by electronic corrosion and extracted crack volume and corroded rebar [13]. It indicated the potential to solve the crack propagation and corrosion mechanism in non-destructive manner. Yang et al. [14] carried out the in-situ micro X-ray CT tests of concrete cubes under progressive compressive loading conditions to study 3D fracture

evolution. This applied not only the threshold-based segmentation to visualize directly the development of cracks but also Digital Volume Correlation (DVC) technique to map the relative deformations between consecutive images with high precision. Moreover, it suggested that the segmented microstructures can be used as inputs for image-based FE models, and the displacements and strains from the DVC analyses of segmented X-ray CT data may be used to validate predictions of these models. However, some authors use a series of manual operations, which are extremely time-consuming and certainly not reproducible. Therefore, segmentation processes are challenging and still needed to improve [15].

In order to assess spatial heterogeneity of internal pore structure, the following performance should be improved; three-dimensional, non-destructive and spatially-resolved investigation (non-bulk dependent), no constraining specific specimen preparation requirement (e.g. drying), direct measurement without interpolation or hypothesis on pore geometry and a sufficient high spatial resolution to detect all size range of cement pores including gel pores, i.e. a nano-scale resolution. This improvement processed and analyzed to get morphological information of the cement pore network such as pore shapes, sizes and pore connectivity and tortuosity [16]. Over the last years, spatial resolution of the technique improved and reached values lower than 1μm as the capabilities of the optics used to focus the beam have increased. The resolution of the CT images depends on the spot size of the X-ray source, the optics used for the magnification and resolution of the detector.

Synchrotron-based microtomography has been used extensively over the past quarter century to study pore structure in a variety of heterogeneous materials [17]. Galluci et al. [18] reported that porosity and pore connectivity of cement measured by μ-CT strongly depend on the voxel size (spatial resolution). Landis et al. [19] applied the synchrotron X-ray source to measure internal crack growth during each load increment. Promentilla et al. [20] characterized pore connectivity and tortuosity to understand the effect of microstructure on transport processes using synchrotron X-ray with submicron resolution (0.5 μm/voxel) in SPring-8. Sugiyama et al. [21] evaluated the diffusion tortuosity in deteriorated cement pastes as a pore structure-transport parameter and revealed that the deterioration of the cement matrix due primarily to the dissolution of portlandite decreases the diffusion tortuosity to a single digit as the degree of pore connectivity larger at the submicron scale. Provis et al. [22] also applied μ-CT to evaluate the microstructure and pore network characteristics of alkali-activated binders like geopolymer. The findings of this research indicated that porosity reduction was observed in samples with ≥50% slag content significantly, which were affected by a space-filling calcium (alumino) silicate hydrate gel.

2.2.2 Chemical property analysis

(1) Electron microscopy

Electron microscopy is one of the most powerful techniques for studying the microstructure of cementitious materials. With many advances, scanning electron microscopy (SEM) is widespread and even benchtop machines are available at relatively low cost. Transmission electron microscopy has also made a significant contribution to understand microstructure.

SEM is available to the huge range of samples. It can be possible to visualize the morphology of cement hydration system with presence of microcrack [23]. It may also be applied to mortars and concretes and has the unique advantage of being able to isolate the paste part of these composites. It is also possible to study interfacial transition zone (ITZ) [24].

To obtain backscattered electron (BSE) images is also useful in terms of that it can reveal the different phases. A significant advantage of BSE imaging is that the contrasts is reproducible and can be used for quantitative analysis of images. Furthermore, it has a wide range of magnifications from about 20× to 10,000× so that features can be seen in detail and in context. At low magnifications, the arrangement of aggregates, paste and any defects in a concrete may be studied. At the highest magnifications, it is possible to observe the morphology of the hydrate phases – C-S-H, ettringite, etc, and pores down to about 100 nm [25]. However, it still has a limitation in terms of visualization of 2D images.

Transmission electron microscopy (TEM) has also made a significant contribution to understanding these materials, although this is much less widely used due to more limited availability of instrumentation and difficult sample preparation. Details that cannot be captured in SEM can be studied in TEM, such as the morphology of hydrates and chemical analyses without the problems of intermixing. Our understanding of the nature of the nearly amorphous C-S-H phases has been advances by developments in analytical TEM [26]. However, how to operate the device is difficult. The high current density used in TEM techniques may easily destroy the sample by excessive heating. Even low doses of electrons may have a quite significant impact on the delicate structure of C-S-H.

(2) Electron probe micro-analyzer

Application of Electron Probe Micro Analysis (EPMA) method to cementitious materials has been increasing. EPMA enables us to carry out qualitative and quantitative analysis of element in micro region and distribution analysis of specific element concentration. Moreover, it has high spatial resolution (less than 1 μm). Therefore, it was utilized to assess decrease ratio of Ca/Si ratio and the amount of chloride ion penetration from surface of concrete [27, 28]. Owing to the applicability, Area Analysis method using EPMA has established as a JSCE standards [29]. However, even if the use of EPMA permits measurement on the order of 0.1 mm, chemical

compounds cannot be identified – only the profile of atoms.

(3) Thermogravimetric analysis

Thermogravimetric analysis (TGA) is a widely applied technique in the field of cement science. Measurements of bound water and portlandite content by TGA are often used to follow the reaction of Portland cement [30], or to evaluate the reactivity of supplementary cementitious materials (SCMs), such as fly ash and blast furnace slags [31]. TGA is able to identify X-ray amorphous hydrates, such as C-S-H or AH_3, and can be used complementarily to other techniques such as XRD. These identifications are derived from that minerals and hydrates can undergo several thermal reactions: dehydration, dihydroxylation, decarbonation, oxidation, decomposition, phase transition, or melting. Weight changes or release of heat from TGA results show these reactions. Based on the recorded weight changes during the TGA measurement, the amount of mineral or hydrate can be easily calculated in cement hydration systems where only one or two solids are present. However, cement hydration systems have a multitude of minerals and hydrates. Therefore, the reactions often overlap, which makes quantification difficult.

(4) Calorimetry

Calorimetry is the measurement of heat and heat production rate. It is a generic way of studying processes, all processes (physical, chemical, and biological) are generally related to enthalpy changes. One of the oldest and most common applications of calorimetry is to study the hydration of cement [32]. There are many different types of calorimeters that can be used in the cement field, and some of them have many uses. The most common technique is isothermal (heat conduction) calorimetry in which the heat production rate (thermal power) from small samples of paste or mortar is directly measured. Differential scanning calorimetry (DSC) is used to study the heat effects of changing temperature. This is a very common technique in many fields; in the cement field typical applications are, e.g. quantifying gypsum and hemihydrate in anhydrous cement [33], or determining the free (freezable) water via low-temperature DSC, assessing freezing processes [34]. Moreover, DSC can be applied to study the pore size distribution and cumulative pore size using thermoporometry [5]. It can quantify gel pore structure in the size of 3nm or less.

(5) X-ray diffraction

X-ray diffraction (XRD) is one of the most prominent analytical techniques in the characterization of crystalline or fine-grained materials. The feature of XRD is the rapid and if carried out properly, the amounts of each cement hydration phases. XRD can also be used to quantify the degree of hydration of the anhydrous cement and can provide the information on

the formation of hydrated phase individually. Recently, Rietveld method started to apply for quantitative phase analysis [35].

X-ray diffraction is based on the scattering of X-rays. Here X-ray used to investigate and quantify the crystalline nature of materials by measuring the diffraction of X-rays from the planes of atoms within the material. The produced diffraction pattern depends on the atoms present, their locations, and thermal motion. Every crystalline substance produces a unique diffraction pattern, which is fingerprint of the material. In polycrystalline materials, each phase produces its pattern independent of the others. X-ray diffraction analysis is thus ideally suited for the characterization and identification of phases. In 1912, Max von Laue discovered that crystalline substances act as three-dimensional diffraction gratings for X-ray wavelength similar to spacing of planes in a crystal lattice. X-ray diffraction depends on constructive interference of monochromatic X-ray and crystalline sample. The interaction of the incident ray with the sample produces constructive interference and a diffracted ray when conditions satisfy Bragg's Law ($n\lambda=2d\sin\theta$). Bragg's Law depends on the wavelength of electromagnetic radiation to the diffraction angle and the lattice spacing in a crystalline sample. The diffracted X-rays are then detected, processed and counted. By scanning the sample through a range of 2θ angles, all possible diffraction directions of the lattice should be attained due to the random orientation of the material. Conversion of the diffraction peaks to d-spacings allows identification of the mineral because each mineral has a set of unique d-spacings. Typically, this is achieved by comparison of d-spacings with standard reference patterns. The mentioned above technique is conventional XRD or angle dispersive XRD technique. There is another XRD technique, so called Energy-Dispersive XRD (EDXRD), where white X-rays used as an incident X-ray and operated at a fixed scattering angle. The concept of obtaining structural information with the new method was originally introduced by Giessen and Gordon in 1968 [36]. This method is based on the good energy resolution of semiconductor detectors. A collimated (parallel) white X-ray beam is scattered by the specimen through a fixed optimized angle 2θ and the energy distribution of the scattered X-ray is analyzed by a semiconductor detector connected to a multichannel pulse height analyzer. The measured energy distribution of the scattered X-ray shows distinct peaks as like as the angle dispersive diffraction (ADXRD) method, providing the required information for structural studies of materials [37]. The EDXRD method has many advantages compared with the conventional ADXRD method. The fixed scattering angle geometry makes EDXRD especially suitable for in-situ studies in special environments (e.g. under very low or high temperatures and/or pressures). Only one entrance and one exit window are needed. EDXRD is able to collect full simultaneously, it enables studies where structural changes can be determined over time. EDXRD is almost exclusively used b synchrotron X-ray, which allows for measurement within real engineering materials.

Furthermore, EDXRD has some difficulties. Here the peaks are more than one order of magnitude wider than in ADXRD. Another disadvantage of EDXRD is the potential for overlap of fluorescence peaks and diffraction peaks. There is an influence of polarization of the primary X-ray beam on integrated intensities. The spectral intensity distribution of the incident white X-ray available from a conventional target is non-uniform and limited. There is a limited input count rate in EDXRD. Need an energy-dependent absorption corrections. Some of the mentioned above difficulties can be diminished or removed by using the X-ray produced by high energy synchrotrons. The synchrotron X-ray, especially from a storage ring is an ideal X-ray source for EDXRD. The high intensity (about 10^3 times larger than that using a conventional X-ray tube) of synchrotron X-ray, its smooth spectrum and well-defined polarization make it possible to obtain quantitative intensity measurements. This EDXRD technique with synchrotron X-ray from a storage ring is used in this study.

2.3 MOTIVATION TO DEVELOP THE METHOD

Nowadays, durability is important factor to preserve the deterioration. However, while about 70 % of concrete is composed of aggregate, durability of concrete is mainly dependent on cement paste matrix because it is porous area and thus governs transport phenomena. Therefore, it is very important to predict the deterioration properly, but these microstructural phenomena process is very slow and microscale. With conventional experiments, there are many limitations that the detectable order of measurement for the deterioration front ranges from 1 to 10mm in precision at most especially in leaching behavior, and it is given merely in one dimension. Even if the application of more precise technique like EPMA, chemical compounds cannot be identified. Considering the slow kinetic process of cement hydrate alteration, the period of experiment becomes lengthy. When other techniques applied to evaluate the degradation area, it must be destroyed each time during the experiment. X-ray CT is good methodology to segment the internal structure such as pores or air voids. However, using the synchrotron radiation X-ray CT cannot identify the distribution of a mineral in three dimensions because of small difference of X-ray absorption characteristics, which means only lowered contrast in a CT image can be obtained. Therefore, it was anticipated that if X-ray CT combined with XRD in same X-ray source was accomplished, it can solve the problems above discussed. Then the development of the CT-XRD has started.

2.4 NON-DESTRUCTIVE INTEGRATED CT-XRD METHOD

2.4.1 Facility introduction

Non-destructive integrated CT-XRD method has been originally developed at BL28B2 in SPring-8, which is the synchrotron radiation facility in Japan [38-40]. SPring-8 has the most powerful synchrotron radiation which is currently available. Consisting of narrow, powerful beams of electromagnetic radiation, synchrotron radiation is produced when electron beams, accelerated to nearly the speed of light, are forced to travel in a curved path by a magnetic field. The research that was conducted at SPring-8, located in Harima Science Park City, Hyogo Prefecture, Japan, includes nanotechnology, biotechnology, and industrial applications. The name “SPring-8” is derived from “Super Photon ring-8 GeV” (8GeV, or 8giga electron volts, being the energy of electron beam circulating in the storage ring). SPring-8 was opened in 1997 to users from academia, research institutes, governmental agencies and domestic and international. Any user whose application is accepted may use the facility. SPring-8 is managed by RIKEN, with the Japan Synchrotron Radiation Research Institute (JASRI) in charge of operation, maintenance and promotion of use.

BL28B2 is a multi-purpose beam line (BL) using white X-rays. Area of research is covered by white X-ray diffraction and topography, time-resolved energy-dispersive XAFS (DXAFS) for studies of chemical and/or physical reaction process, biomedical imaging and radiation biology studies, and high energy (~200 keV) X-ray microtomography. Figure 2-1 shows the photograph of inside the hutch and Figure 2-2 shows the photograph of appearance of sample sitting on the stage.

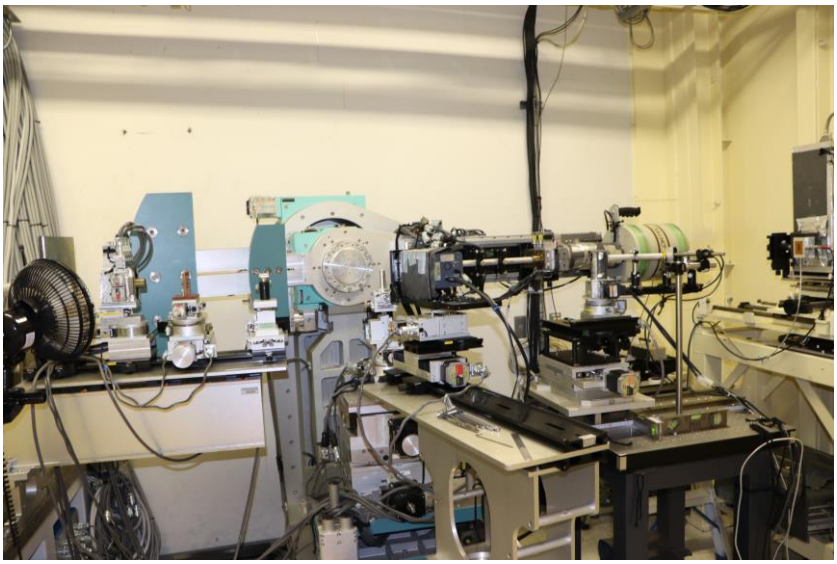


Figure 2-1 The photograph of inside the hutch

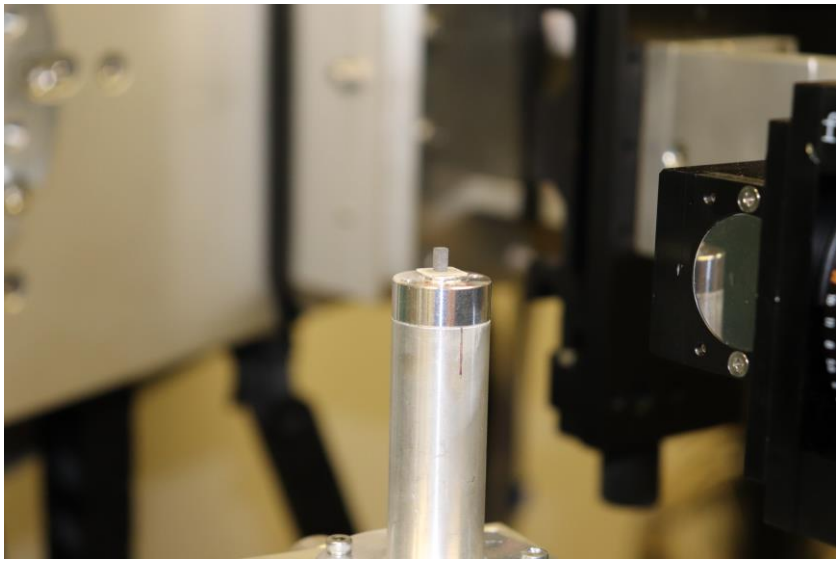


Figure 2-2 The photograph of the appearance of sample sitting on the stage

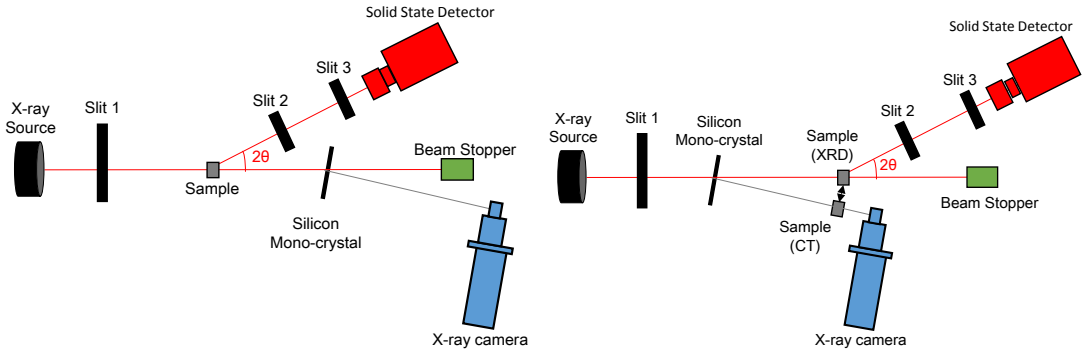


Figure 2-3 Schematic diagram of the system for non-destructive integrated CT-XRD method (The left is previous system and the right is current one.)

Our research group has developed a non-destructive technique to study the microstructure of hardened cementitious materials using its X-ray source [32, 33, 41-43].

2.4.2 Outline of non-destructive integrated CT-XRD method

As described above, the specified BL employs white X-ray diffraction, which is one of the unique features of this method. A white X-ray covers a wide range of wave length zone. Therefore, with using a white X-ray as the incident X-ray there is no need to scan the angle between sample and detector, and energy-dispersive XRD profile can be obtained. Figure 2-3 shows the outline of this method (both the original and updated is shown). Compared with both, the silicon mono-crystal is moved to upstream position to enhance the image contrast more. The

details for CT and XRD measurement are discussed respectively in the next section.

2.4.3 Details of CT measurement

White X-ray is emitted to a silicon mono-crystal located in upstream position of sample and then diffracted to a specific angle while getting itself monochromatic as shown in Figure 2-3. Sample is set in the direction of diffracted X-ray and exposed followed by capture of X-ray camera. The reason why the monochromatic X-ray is extracted from the white X-ray is to enhance image contrast. Therefore, the couple of CT and XRD measurement is feasible using the same X-ray source. In previous system, the silicon mono-crystal is located in the downstream position. That system, however, has problems that noise is generated due to scattering of transmitted X-ray and edge-enhancement effect increases due to long camera-length. Consequently, only CT images with low signal to noise ratio can be obtained. In order to solve this problem, the silicon mono-crystal is moved to the upstream position and sample is subsequently set on the way of diffracted X-ray, and camera is set beyond the sample. Then signal to noise ratio was improved to obtain good quality of images [44]. The stage on which sample sets is revolving during CT measurement and thus transmission images of X-ray with different angles can be obtained. Image reconstruction can be carried out by back projection of the transmission images with using the software in adjoining operational computer. The reconstructed images in three dimensions can be referred as determinations of ROI followed by XRD measurement.

2.4.4 Details of XRD measurement

X-ray diffraction profile can be obtained in the Region of Interest (ROI). Sample is moved on the straight line of X-ray irradiating direction as shown in Fig. 3. In order to extract the signal of the X-ray diffraction only in the ROI, three slits are deployed in the system. A slit in the upstream position (S1) and two slits in the downstream (S2 and S3) are installed so as to focus a specific space and obtain the only signals of X-ray diffraction there, called the gauge volume. The gauge volume can be set on ROI because the coordinate system in the CT measurement corresponds to that in the XRD measurement. A solid-state detector is used and located behind S2 and S3. The angle of the arm that corresponds to the twice of the diffraction angle (2θ) is fixed during the measurement and the relationship between X-ray energy and the intensity of diffracted X-ray can be obtained. To compare the results of the CT-XRD and Powder-XRD, the variable number, “Energy” from the CT-XRD results, was converted to “diffraction angle” using two relationships; one is the relationship of light and energy (see (1)) and the other is Bragg’s equation (see (2)).

$$E = \frac{hc}{\lambda} = \frac{12.3983}{\lambda} \qquad (1)$$

Where E is the energy of incident X-ray, h is the planck constant (≒6.63×10^{-34}), c is the speed of light (≒3.00×10^{8}), and λ is the wavelength of the incident wave.

$$\lambda = 2d\sin\theta \qquad (2)$$

Where d is the spacing between the planes, and theta is the angle between the incident X-ray and the scattering planes.

Table 2-1 summarized the details information about setup conditions of the CT-XRD used in this study

2.4.5 Procedure of measurement

The procedure for the measurement of the CT-XRD is shown as follows. A sample sits on the stage in the BL hutch. First, CT measurement is carried out followed by reconstruction to obtain microtomographic images. Then, the region of interest (ROI) in a given cross section of the sample is determined. Finally, XRD is measured targeting the ROI. Figure 2-4 shows the flowchart of the CT-XRD procedure.

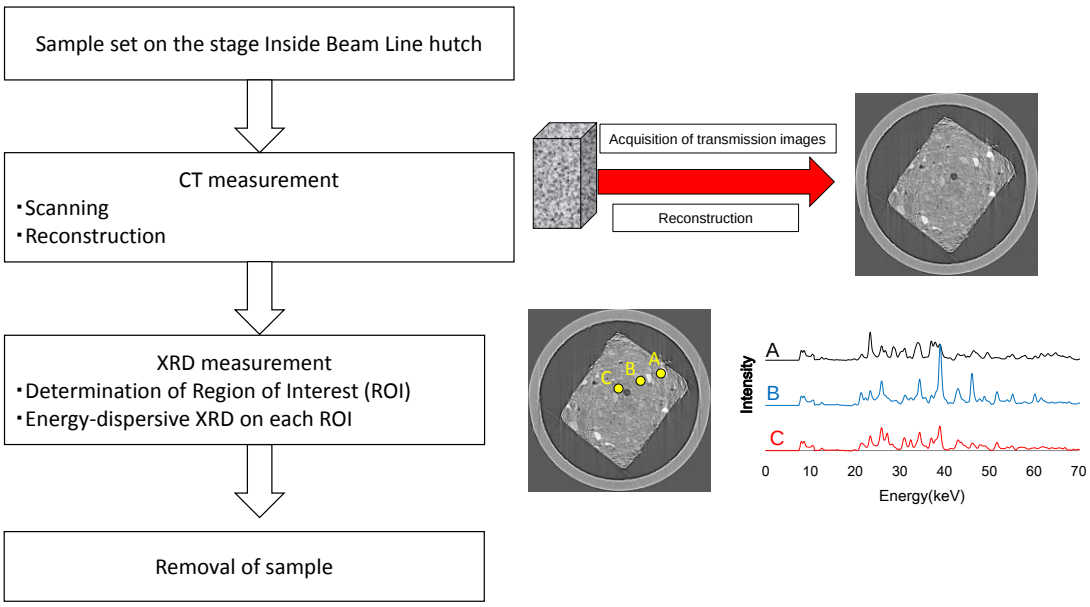


Figure 2-4 Flowchart of non-destructive integrated CT-XRD method

Table 2-1 Details information of the CT-XRD used in this study

	Items		Experiment conducted in this study				
			Chapter 3		Chapter 4	Chapter 5	
			Ex1	Ex 2		Ex 1	Ex 2
CT	Instrument arrangement♯		Current		Previous	Current	
	Extracted X-ray energy (keV)		25				
	Angle step (deg.)		0.12				
	Rotation (deg.)		180				
	Number of projections		1500				
	Exposure time (s)		0.4				
	Image reconstruction algorithm		Back Projection Procedure				
	Total number of cross-sectional image		1440		767	1440	
	Cross-section image size (Number of pixel)		1920×1920		768×768	1920×1920	
	Pixel size*	Cross section (μm)	2.45		7.67	2.45	
		Slice thickness(μm)	2.45		5.14	2.45	
	Distance**	A to B (mm)	600		500	600	
		B to C (mm)	30		350	30	
XRD	Slit size	S1 (Width × Height)	0.05 mm× 0.30 mm		0.05 mm× 0.15 mm	0.05 mm× 0.30 mm	
		S2 (Width × Height)	0.025 mm×3.00 mm				
		S3 (Width × Height)	0.15 mm×10.00 mm				
	Distance	S1 to sample (mm)	800		270	800	
		sample to S2 (mm)	170		150	170	
		S2 to S3 (mm)	440		460	440	
	Diffraction angle (θ)		5°		10°	5°	
	Preset time (s)		300				

*Pixel size is slightly different between each measurement in Experiment because of delicate setup.

** Previous A=Sample, B=Mono-crystal, C=Camera

Current A=Mono-Crystal, B=Sample, C=Camera

♯ See Figure 2-3

2.4.6 Analysis method

(1) Reconstruction of transmission image

Projection images were taken at different views with a definite exposure time per projection with an angle step. The transmitted images are then detected by an X-ray image detector which consists of a thin scintillator, optic system and CCD camera. Tomographic reconstruction is performed using a public domain computer program in use at SPring-8, which employs the convolution back projection algorithm to generate each slice or cross section images. The quality of reconstructed image can be improved by adjusting the rotation center.

(2) 3D imaging

The stack of the slices provides the reconstructed volumetric data of the scanned sample. Therefore, the reconstructed 3D-image data set was composed of contiguous grayscale images. With stacking up all slices, a 3D image in the scanning area can be obtained using free software "ImageJ" [45]. Figure 2-5 shows the example of 3D imaging for ROI.

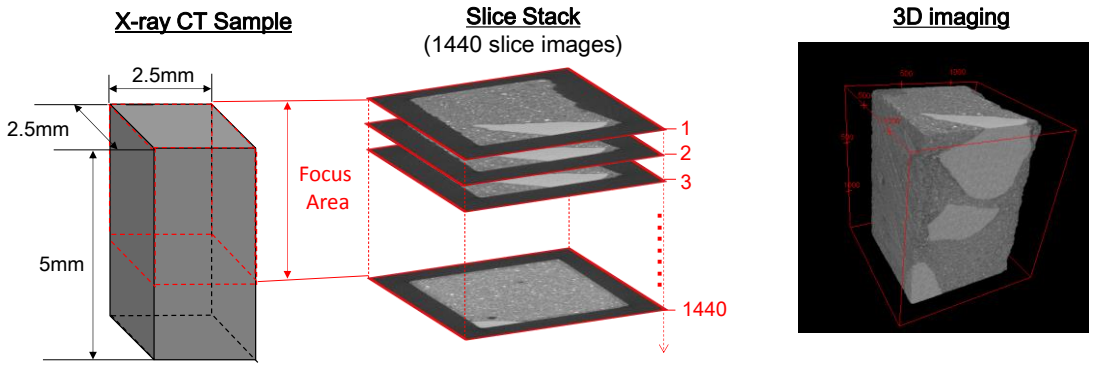


Figure 2-5 Example of 3D imaging

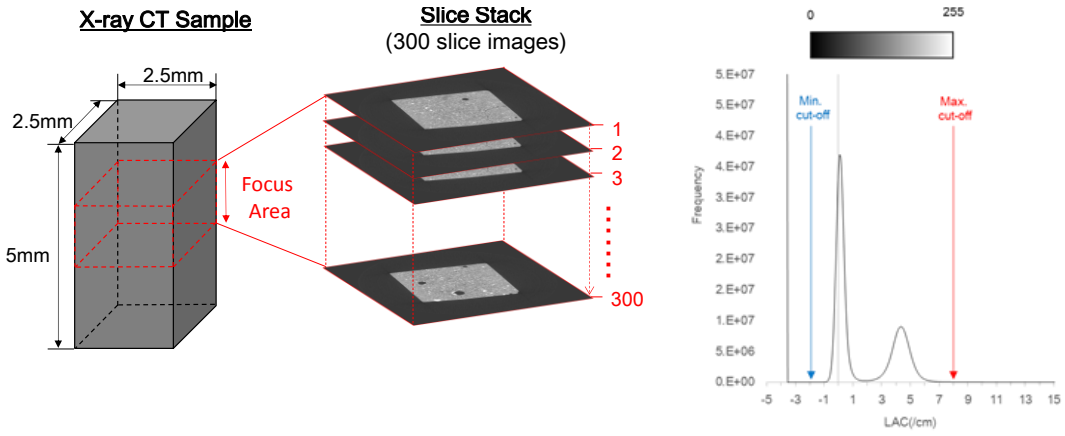


Figure 2-6 Example of CT histogram of the CT images and rescaling to 8bit gray scale images

Table 2-2 Composition, notation, density, and linear attenuation coefficient of different phases on cement system [50]

Phase	Chemica Formula	Notation	Density	Linear Attenuation Coefficient at 25 keV
Ferrite	$(CaO)_4(Al_2O_3)(Fe_2O_3)$	C_4AF	3.708	21.21
Free lime	CaO	C	3.341	16.67
Alite	$(CaO)_3(SiO_2)$	C_3S	3.120	12.59
Belite	$(CaO)_2(SiO_2)$	C_2S	3.326	12.40
Aluminate	$(CaO)_3(Al_2O_3)$	C_3A	3.030	11.27
Anhydrite	$CaSO_4$	$C\underline{S}$	2.968	9.28
Portlandite	$Ca(OH)_2$	CH	2.251	8.79
Calcite	$CaCO_3$	$\underline{C}$	2.710	8.14
Calcium Silicate Hydrate (Jennnite)	$(CaO)_9(SiO_2)_611H_2O$	CSH	2.331	6.83
Calcium Silicate Hydrate (Tobermorite 14 Å)	$(CaO)_5(SiO_2)_68H_2O$	CSH	2.228	5.58
Calcium Silicate Hydrate (Afwillite)	$(CaO)_3(SiO_2)_23H_2O$	CSH	2.645	7.97
Calcium Silicate Hydrate Ⅰ	$(CaO)_{1.7}(SiO_2)4H_2O$	CSH	1.85[a)]	4.83
Calcium Silicate Hydrate Ⅱ	$(CaO)_{1.7}(SiO_2)1.8H_2O$	CSH	2.604[b)]	8.58
Gypsum	$CaSO_42H_2O$	$C\underline{S}H_2$	2.311	5.89
Monosulfate	$(CaO)_3(Al_2O_3)(CaSO_4)12H_2O$	$C_4A\underline{S}H_{12}$	2.015	4.21
Periclase	MgO	M	3.584	3.91
Quartz	SiO_2	S	2.641	3.62
Ettringite	$(CaO)_3(Al_2O_3)(CaSO_4)_332H_2O$	$C_6A\underline{S}H_{32}$	1.778	3.56

Sources: a) Bentz et al. (1994); b) Allen et al. (2007);
no mark) Balonis and Glasser (2009)

(3) Rescaling to 8bit gray scale image

Figure 2-6 shows the example of CT histogram of Linear Attenuation Coefficient (LAC)

rescaled to 8bit gray scale image. Originally, each voxel of reconstructed images is expressed in 32bit LAC based value. This 32bit images are very clear but too heavy file type to carry out image processing. Therefore, image normalization or contrast stretching was applied to the whole stack of the reconstructed slices on the basis of the predetermined LAC values of the phases of concern. This procedure allowed us to even out the brightness among the slices and enhance the contrast in the said images.

This histogram is based on the stacks of ordinary Portland cement paste shown in left side. There are two distinct peaks which are associated with the air and the cement matrix, respectively. From Figure 2-6, it can be said that larger peaks position around the value of 4.8. Table 2-2 provides the list of some of the referred minerals for hardened cement pastes with LAC at the X-ray energy level of 25 keV. LAC of the referred minerals was obtained from the NIST database [46] after imputing the chemical compounds and density of targeted mineral, which was referred to Ref. [47-50]. According to this table, the larger peak is closer to the LAC of C-S-H Ⅰ and other candidate minerals like Portlandite can be negligible. Therefore, it can be said that the area of cement paste in these cross sectional images mainly indicates the distribution of C-S-H.

Minimum parameter was determined as the sharp incline point from almost zero and the maximum was set as the convergence point to almost zero (-2 and 8, respectively, in this case), and then 8-bit grayscale images with values that range from 0 to 255 were produced. The GSV in the images is directly related to the measured LAC according to this equation (3):

$$\mathrm{GSV} = \left(\frac{255}{maximum - minimum}\right)(LAC - minimum) \qquad (3)$$

(4) Threshold based segmentation

After normalization of images, threshold-based segmentation can be implemented [51]. Figure 2-7 shows the example of histogram for all stacks of mortar sample with 5 % volume of

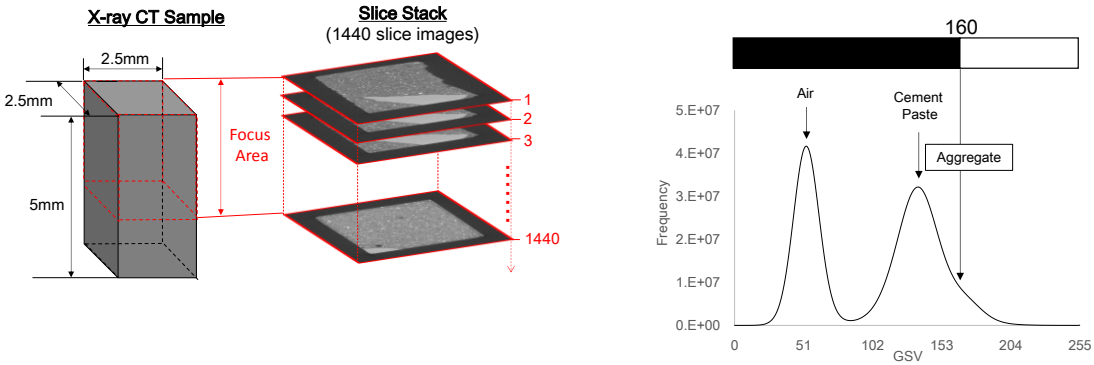


Figure 2-7 Example of ROI and threshold determination

limestone aggregate and Figure 2-8 the result of aggregate segmentation. To extract the constituent itself, SLICE program was used, which is a basic 3D-image analysis program developed in SPring-8 [52]. According to Figure 2-7, three peaks can be found derived from air, cement paste, and aggregate in ascending order. In this case, threshold was determined as 160 and binarization was carried out using Pixel Value Replacer (PVR). Then, multiple cluster labeling was applied to binarized image stacks to extract the larger objects [52]. Then the aggregate distribution inside the sample was visualized as shown in the right side of Figure 2-8.

(5) Identification of minerals

Identification of minerals is important to analyze the presence or absence of cement hydration products, which means the evaluation of alteration. In this research, identification was carried out to compare obtained energy dispersive profile with theoretical profile obtained by inputting the lattice constant of targeted minerals using simulation software developed in BL28B2. Figure 2-9 and 2-10 show the monitors of simulation software distributed by SPring-8 [53]; the former indicates the calculation of theoretical profile, and the latter does the set and subtraction of background. Theoretical profile can be obtained by setting the crystal structure file and various parameters.

Some standard crystal structure database [Inorganic Crystal Structure Database (ICSD),

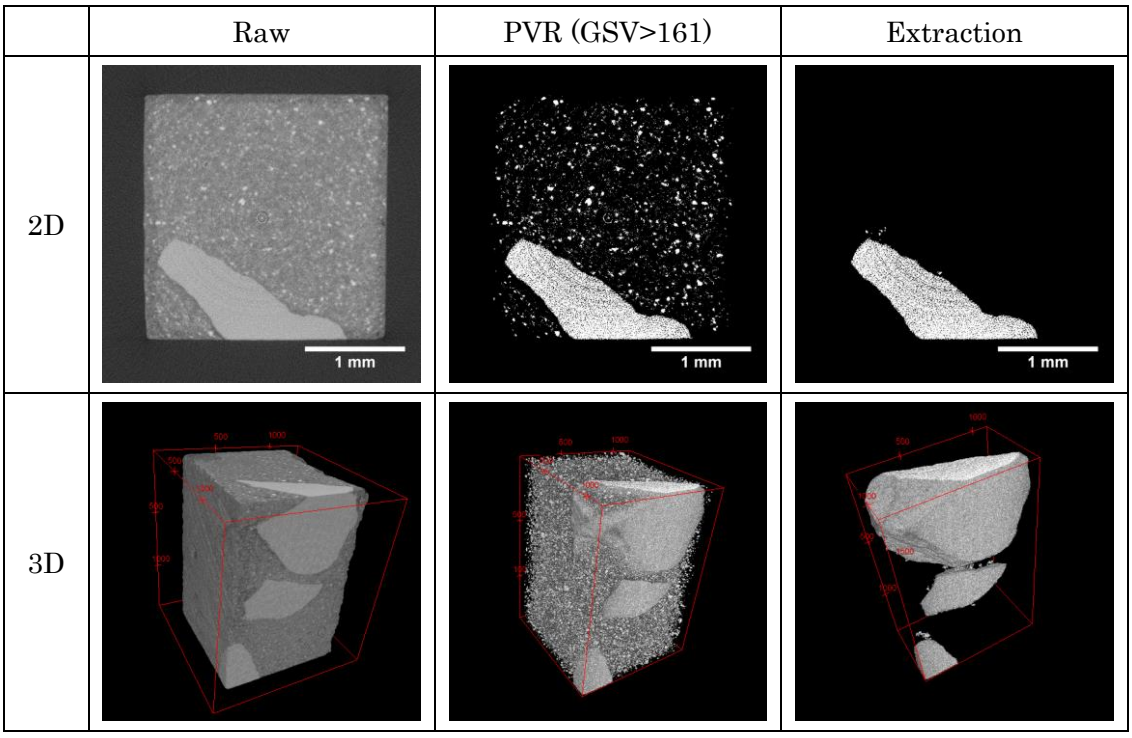


Figure 2-8 Example of phase segmentation

American Mineralogist Crystal Structure Database (AMCSD), Crystallography Open Database (COD), and so forth] can be applicable to get the mineral information. In this study, ICSD was

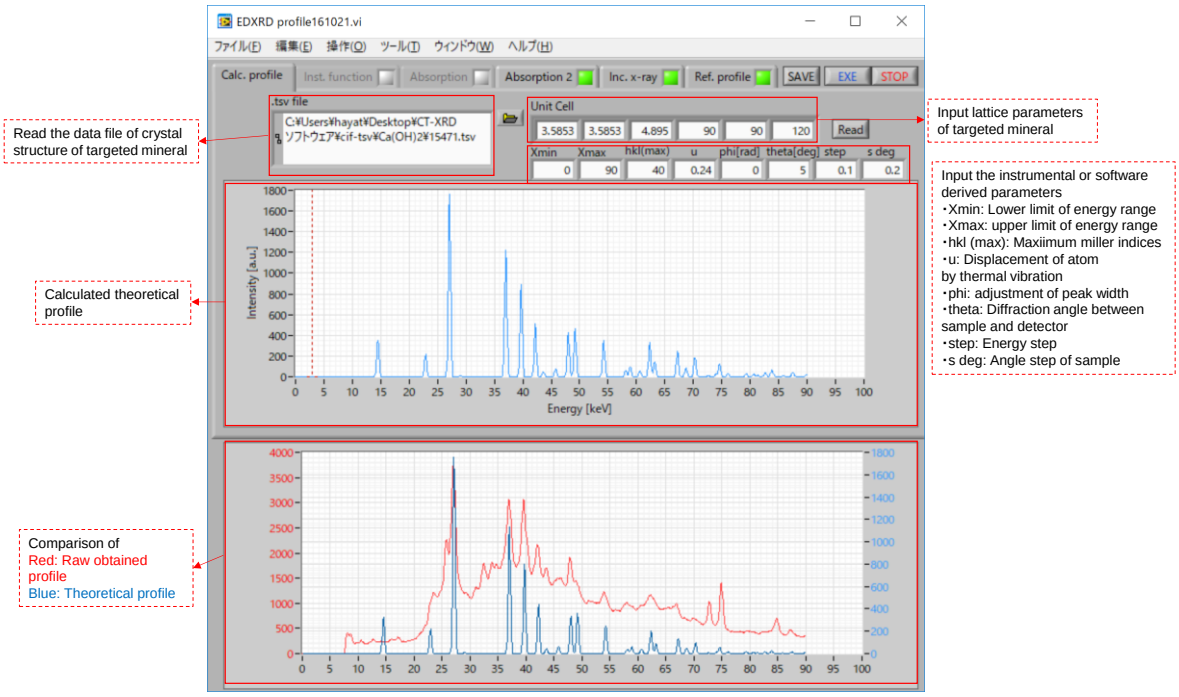


Figure 2-9 Monitor of simulation software; the way to output theoretical profile

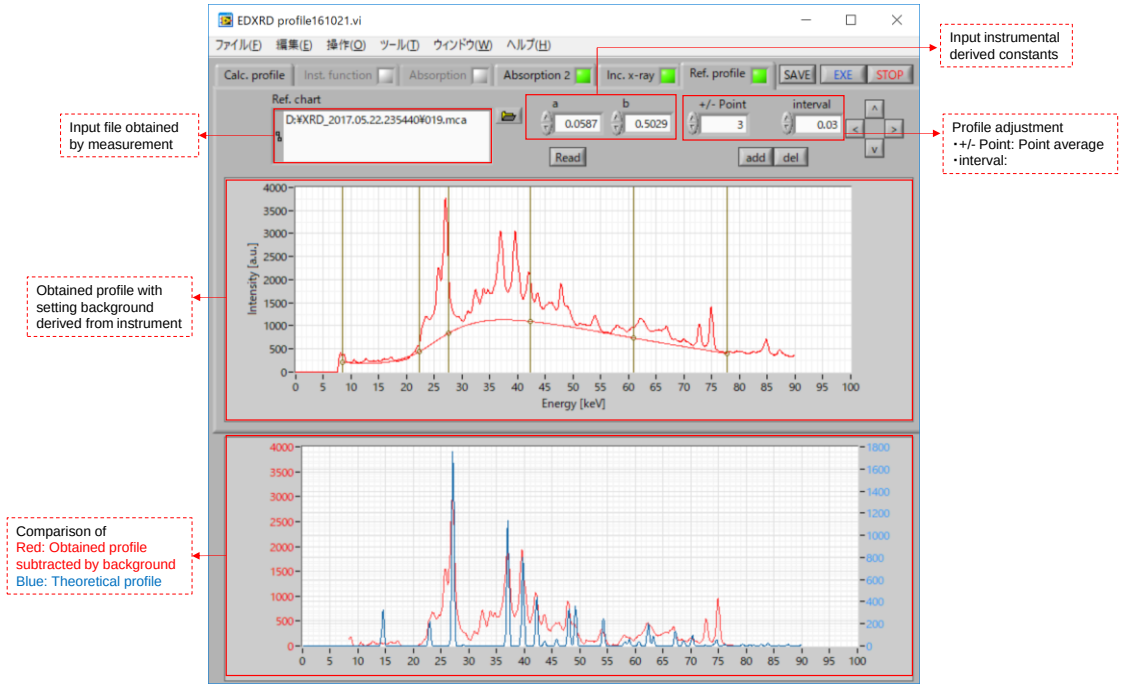


Figure 2-10 Monitor of simulation software; the way to output background subtracted profile

used to do so. According to the parameters, the lattice parameters, which means the length and angles of unit cell of smallest structural unit, should be input. Moreover, instrumental or software derived parameters, which means diffraction angle between sample and detector should also be input. Then, the theoretical profile, which is shown as that peak position and

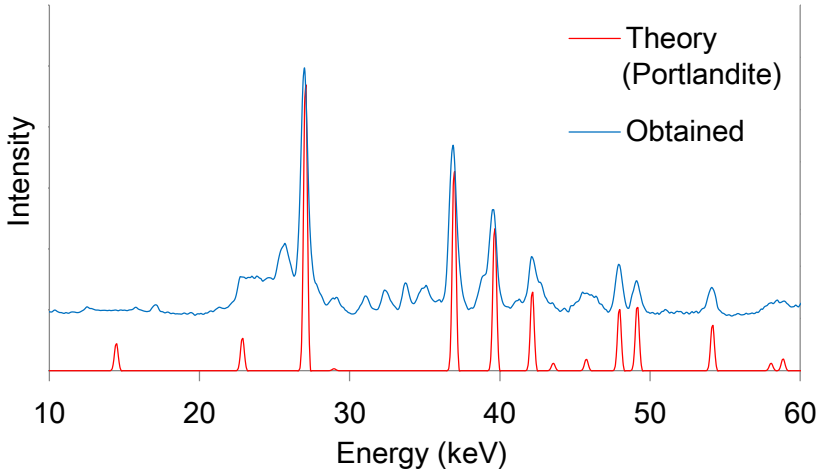


Figure 2-11 Comparison of obtained data of plain cement paste with theoretical data of portlandite

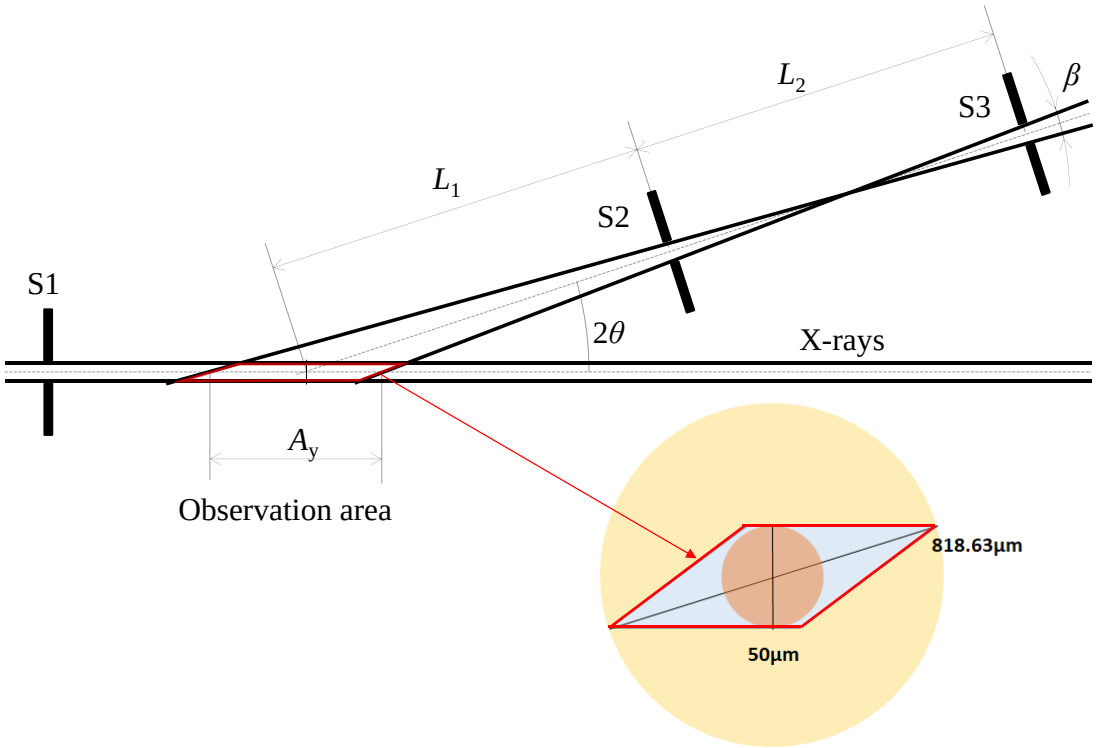


Figure 2-12 Conceptual diagram of the gauge volume

peak intensity were calculated, can be obtained like Figure 2-9.
Moreover, raw obtained profile has instrumental derived background hallow. This can be subtracted by setting the background profile manually. Figure 2-10 shows the result of subtracted obtained profile.
In this thesis, the profiles are shown as background-subtracted type. Figure 2-11 shows the comparison between obtained profile of ordinary Portland cement paste from the CT-XRD and theoretical profile of Portlandie [$Ca(OH)_2$]. It can be seen that many peaks positions of obtained profile are matched with theoretical peaks whereas peaks of obtained profile are broader.

(6) Detection area of XRD
Figure 2-12 shows the detection area of XRD target, so called the gauge volume. As explained in section 2.4.2.2, diffraction signal is measured in the gauge volume. The area indicated as observation area (A_y) can extract the diffraction signals. During the measurement, the sample was rotating because the diffraction signal could be adequately obtained from the increased crystal grain and the diffraction profile can be averaged in the observation region. Therefore, the area which diameter is longer diagonal line of gauge volume is an actual observation area. The intensity of diffraction signals accounts for 90 % within the inscribed circle of gauge volume. With regards to the distance and width of Slit 1, Slit 2 and Slit 3, the diameter of inscribed circle is 50 μm and the diagonal line is 818.63 μm in length.

2.4.7 Application example
Brief literature reviews using the CT-XRD are introduced in this section. Kuri et al. [54] studied the leaching behavior of cracked cement paste. The results suggest that the dissolution zone of the cement paste with a water to cement ratio (W/C) of 0.5 was larger than the case with a W/C of 0.3. In addition, it appeared that the calcite formation reduced the rate of the dissolution from the crack boundary. Kikuchi et al. [55] studied the effect of carbonation test followed by water flow test. It suggested that carbonation affects the blocking of leaching behavior with regards to the results of monitoring the pH values and Ca^{2+} ion concentration.

2.5 SUMMARY

This chapter introduced main tools for this research, namely non-destructive integrated CT-XRD method. First, the significances of conventional microstructural analysis techniques were described. Then, the problems of conventional techniques were extracted and motivation of developing this new methodology was also introduced. For the next, Outline of

non-destructive integrated CT-XRD method was explained including the introduction of SPring-8, which has unique instruments to accomplish the method all over the world followed by the research introduction of application.

REFERENCES

[1] Cook, R., and Hover, K. C. (1999). "Mercury porosimetry of hardened cement pastes." *Cement and Concrete Research*, 29(6), 933-943.

[2] Diamond, S. (2000). "Mercury porosimetry - An inappropriate method for the measurement of pore size distributions in cement-based materials." *Cement and Concrete Research*, 30(10), 1517-1525.

[3] Willis, K. L., Abell, A. B., and Lange, D. A. (1998). "Image-based characterization of cement pore structure using Wood's metal intrusion." *Cement and Concrete Research*, 28(12), 1695-1705.

[4] Korpa, A., and Trettin, R. (2006). "The influence of different drying methods on cement paste microstructures as reflected by gas adsorption; Comparison between freeze-drying (F-drying), D-drying, P-drying, and oven-drying methods." *Cement and Concrete Research*, 36(4), 634-649.

[5] Kuriyama, H., Kurosawa, K., Gotoh, S., and Nawa, T. (2012). "Determination of pore structure of porous materials by thermoporometry." *Cement Science and Concrete Technology*, 66(1), 119-126. (in Japanese)

[6] Mági, M., Lippmaa, E., Samoson, A., Engelhardt, G., and Grimmer, A. R. (1984). "Solid-state high-resolution silicon-29 chemical shifts in silicates." *Journal of Physical Chemistry*, 88(8), 1518-1522.

[7] Lippmaa, E., Mägi, M., Tarmak, M., Wieker, W., and Grimmer, A. R. (1982). "A high resolution ^{29}Si NMR study of the hydration of tricalciumsilicate." *Cement and Concrete Research*, 12(5), 597-602.

[8] Korb, J. –P., Monteilhet, L., McDonald, P. J., and Mitchell, J. (2007). "Microstructure and texture of hydrated cement-based materials: A proton field cycling relaxometry approach." *Cement and Concrete Research*, 37(3), 295-302.

[9] Holly, R., Reardon, E. J., Hansson, C. M., and Peemoeller, H. (2007). "Proton spin-spin relaxation study of the effect of temperature on white cement hydration." *Journal of American Ceramic Society*, 90(2), 570-577.

[10] Landis, E. N., Nagy, E. N., and Keane, D. T. (1997). "Microtomographic measurements of internal damage in portland-cement-based composites." *Journal of Aerospace Engineering*,

10(1), 2-6.

[11] Promentilla, M. A. B., and Sugiyama, T. (2010). "X-ray microtomography of mortars exposed to freezing-thawing action." *Journal of Advanced Concrete Technology*, 8(2), 97-111.

[12] Darma, I. S., Sugiyama, T., and Promentilla, M. A. B. (2013). "Application of X-ray CT to study diffusivity in cracked concrete through the observation of tracer transport." *Journal of Advanced Concrete Technology*, 11, 266-281.

[13] Takahashi, H., Shimura, K., Sugiyama, T., and Tanaka, H. (2016). "Observation of crack area and corroded rebar by electronic test in reinforced mortar using X-ray CT." *Proceedings of the Japan Concrete Institute*, 38(1), 2163-2168. (in Japanese)

[14] Stamati, O., Roubin, E., Andò, E., and Malecot, Y. (2018) "Phase segmentation of concrete x-ray tomographic images at meso-scale: Validation with neutron tomography," *Cement and Concrete Composites*, 88, 8-16.

[15] Yang, Z., Ren, W., Sharma, R., McDonald, S., Mostafavi, M., Vertyagina, Y., and Marrow, T. J. (2017). "In-situ X-ray computed tomography characterization of 3D fracture evolution and image-based numerical homogenisation of concrete." Cement and Concrete Composites, 75, 74-83.

[16] Bentz, D. P., Quenard, D. A., Kunzel, H. M., Baruchel, J., Peyrin, F., Martys, N. S., and Garboczi, E. J. (2000). "Microstructure and transport properties of porous building materials. Ⅱ: Three-dimensional X-ray tomographic studies." *Materials and Structures*, 33(3), 147-153.

[17] Lu, S., Landis, E. N., and Keane, D.T. (2006). "X-ray microtomographic studies of pore structure and permeability in Portland cement concrete." *Materials and Structures*, 39(3), 147-153.

[18] Galluci, E., Scrivener, K., Groso, A., Stampanoni, M., and Margaritondo, G. (2007). "3D experimental investigation of the microstructure of cement pastes using synchrotron X-ray microtomography (μCT)." *Cement and Concrete Research*, 37(3), 360-368

[19] Landis, E. N., Nagy, E. N., and Keane, D. T. (2003) "Microstructure and fracture in three dimensions." *Engineering Fracture Mechanics*, 70(7), 911-925.

[20] Promentilla, M. A. B., Sugiyama, T., Hitomi, T., and Takeda, N. (2008). "Characterizing the 3D pore structure of hardened cement paste with synchrotron microtomography." *Journal of Advanced Concrete Technology*, 6(2), 273-286.

[21] Sugiyama, T., Promentilla, M. A. B., Hitomi, T., and Takeda, N. (2010). "Application of synchrotron microtomography for pore structure characterization of deteriorated cementitious materials due to leaching." Cement and Concrete Research, 40(8), 1265-1270.

[22] Provis, J. L., Myers, R. J., White, C. E., Rose, V., Deventer, J. S. J. van. (2012). "X-ray microtomography shows pore structure and tortuosity in alkali-activated binders." Cement and Concrete Research, 42(6), 855-864.

[23] Wang, X-S, Wu, B-S, and Wang, Q-Y. (2005). "Online SEM investigation of microcrack characteristics of concrete at various temperatures." *Cement and Concrete Research*, 35(7), 1385-1390.

[24] Scrivener, K. L., Crumble, A. K., and Laugesen, P. (2004). "The interfacial zone (ITZ) between cement paste and aggregate in concrete." *Interface Science*, 12(4), 411-421.

[25] Scrivener, K. L. (2004). "Backscattered electron imaging of cementitious materials microstructures: understanding and quantification." *Cement and Concrete Composites*, 26(8), 935-945.

[26] Richardson, I. G. (2000). "The nature of the hydration products in hardened cement pastes." *Cement and Concrete Composites*, 22(2), 97-113.

[27] Haga, K., Shibata, M., Hironaga, M., Tanaka, S., and Nagasaki, S. (2005). "Change in pore structure and composition of hardened cement paste during the process of dissolution." Cement and Concrete Research, 35(5), 943-950.

[28] Tanaka, Y., Kawano, H., and Watanabe, H. (2006). "Chloride ingress into cracking in existing concrete structures." Journal of Japan Society of Civil Engineers (Ser. E), 62(1), 38-51. (in Japanese)

[29] Sub-Committee on New Standards, Committee on Concrete. (2006). "JSCE standards 'area analysis method of elements distribution in concrete by using EPMA." Journal of Japan Society of Civil Engineers (Ser. E), 62(1), 246-259. (in Japanese)

[30] Lothenbach, B., and Winnefeld, F. (2006). "Thermodynamic modeling of the hydration of Portland cement." *Cement and Concrete Research*, 36(2), 209-226.

[31] Scholer, A., Lothenbach, B., Winnefeld, F., and Zajac, M. (2015). "Hydration of quaternary Portland cement blends containing blast-furnace slag, siliceous fly ash, and limestone powder." *Cement and Concrete Composites*, 55, 374-382.

[32] Kocava, V., Gallucci, E., and Scrivener, K. L. (2012). "Methods for determination of degree of reaction of slag in blended cement pastes." *Cement and Concrete Research*, 42(3), 511-525.

[33] Dunn, J., Oliver, G., Nguyen, G., and Sills, I. (1987). "The quantitative determination of hydrated calcium sulfates in cement by DSC." *Thermochimica Acta*, 121, 181-191.

[34] Kaufmann, J. P. (2004). "Experimental identification of ice formation in small concrete pores." *Cement and Concrete Research*, 34(8), 1421-1427.

[35] Scrivener, K. L., Fullmann, T., Gallucci, E., Walenta, G., and Bermejo, E. (2004). "Quantitative study of Portland cement hydration by X-ray diffraction/Rietveld analysis and independent methods." *Cement and Concrete Research*, 34(9), 1541-1547.

[36] Giessen, B. C., and Gordon, G. E. (1968). "X-ray diffraction: New high-speed technique based on X-ray spectrography." *Science*, 159(3818), 973-975.

[37] Laine, E., and Lähteenmäki, I. (1980). "The energy dispersive X-ray diffraction method: annotated bibliography 1968-78." *Journal of Materials Science*, 15(2), 269-277.

[38] Hitomi, T., Kajiwara, K., and Sugiyama, T. (2013). "Micro-observation of chemical compounds in mortar by non-destructive integrated CT-XRD method." *The Proceedings of 67th Annual Convention of Japan Cement Association*, 80-81. (in Japanese)

[39] Kajiwara, K., Hitomi, T., and Sugiyama, T. (2013). "Development of non-destructive integrated CT-XRD method for the evaluation of mineral distribution in cementitious materials." *The Proceedings of 67th Annual Convention of Japan Cement Association*, 82-83. (in Japanese)

[40] Ikeda, S., Sugiyama, T., Hitomi, T., and Kajiwara, K. (2013). "Non-destructive integrated CT-XRD method for the observation of alteration of hardened cement paste with cracks due to water flow." *The Proceedings of 67th Annual Convention of Japan Cement Association*, 84-85. (in Japanese)

[41] Hitomi, T., Mita, Y., Saito, Y., and Takeda, N. (2004). "Observation of fine structure of mortar using X-ray CT images at SPring-8." Proceedings of Japan Concrete Institute, 26(1), 645-650. (in Japanese)

[42] Promentilla, M. A. B., Sugiyama, T., Hitomi, T., and Takeda, N. (2009). "Quantification of tortuosity in hardened cement pastes using synchrotron-based X-ray computed microtomography." Cement and Concrete Research, 39(6), 548-557.

[43] Sugiyama, T., Hitomi, T., and Kajiwara, K. (2014). "Nondestructive integrated CT-XRD method for research on hydrated cement system." *Proceedings of the 4th International Conference on the Durability of Concrete Structures (ICDCS)*, 298-303.

[44] Takahashi, H., Mikami, T., and Sugiyama, T. (2018). "Study on the alteration and crack behavior of mortar exposed to high temperature using non-destructive integrated CT-XRD method." *Proceedings of the Japan Concrete Institute*, 40(1), 1017-1022. (in Japanese)

[45] Rasband, W. (2007). ImageJ; Image processing and analysis in Java, National Insitute of Health (NIH). Available from: < http://rsb.info.nih.gov/ij/>

[46] Chantler, C. T., Olsen, K., Dragoset, R. A., Chang, J., Kishore, A. R., Kotochigova, S. A., and Zucker, D. S. (2005). "X-ray form factor, attenuation, and scattering tables (version 2.1.) [online]." National Insitute of Standards and Technology, Gaithersburg, MD, Available from: <https://physics.nist.gov/PhysRefData/FFast/> [08 Aug. 2018]

[47] Bentz, D. P., Coveney, P. V., Garboczi, E. J., Kleyn, M. F., and Stutzman, P. E. (1994). "Cellular automaton simulations of cement hydration and microstructure development." *Modelling and Simulation in Material Science and Engineering*, 2, 783-808.

[48] Allen, A. J., Thomas, J. J., and Jennings, H. M. (2007). "Composition and density of nanoscale calcium-silicate-hydrate in cement." *Nature Materials*, 6(4), 311-316.

[49] Ballonis, M., and Glasser, F. P. (2009). "The density of cement phases." *Cement and*

Concrete Research, 39(9), 733-739.

[50] Takahshi, H., and Sugiyama, T. (2019). "Application of non-destructive integrated CT-XRD method to investigate alteration of cementitious materials subjected to high temperature and pure water." *Construction and Building Materials*, 203, 579-588.

[51] Nakano, T., Tsuchiyama, A., Uesugi, K., Uesugi, M., and Shinohara, K. (2006). "SLICE – Software for basic 3-D image anlaysis [online]." Japan Synchrotron Radiation Research Institute (JASRI). Available from: <http://www-bl20.spring8.or.jp/slice/>

[52] Hoshen, J. and Kopelman, R. (1976). "Percolation and cluster distribution. Ⅰ. Cluster multiple labeling technique and critical concentration algorithm." Physical Review B, 14(8), 3438-3445.

[53] Kajiwara, K. (2016). Personal communication.

[54] Kuri, J. C., Sugiyama, T., Hitomi, T., and Kajiwara, K. (2015). "Investigation on cracked cement paste subjected to water flow by non-destructive integrated CT-XRD method." Presented in *International Conference on the Regeneration and Conservation of Concrete Structures*, R2-9, Nagasaki, Japan.

[55] Kikuchi, R., Takahashi, H., and Sugiyama, T. (2016). "Study on leaching behavior of the vicinity of crack in cement paste due to water flow using non-destructive integrated CT-XRD method." *Proceedings of the Japan Concrete Institute*, 38(1), 1095-1100. (in Japanese)

CHAPTER 3 IMPROVEMENT OF IMAGE ANALYSIS AND VERIFICATION OF NON-DESTRUCTIVE INTEGRATED CT-XRD METHOD

3.1. INTRODUCTION

This chapter mainly consists of development of non-destructive integrated CT-XRD method. Two experiments were carried out; one is to introduce image analysis from obtained CT images (Experiment 1), and the other is to verify XRD results from CT-XRD by comparison with conventional powder XRD (Experiment 2). At first, a segmentation procedure from X-ray images of mortar samples is introduced to obtain morphological description obtained from Experiment 1. Then, each CT image that is obtained from Experiment 1 is introduced to grasp the distribution of aggregate and crack propagation in mortar sample. From Experiment 2, the profiles of the CT-XRD for each sample were described with powder XRD results. Finally, the results are discussed with verification and advantage of the CT-XRD are explained in summary.

3.2. EXPERIMENTAL OUTLINE

3.2.1 Sample preparation

(1) Experiment 1

Mortar was made in Experiment 1. Ordinary Portland cement was used as binder and tap water with anti-bubble agent was used to reduce entrapped air. Three types of aggregate were mixed in the sample; crushed limestone (C), artificial light weight sand called Mesalite (M), and Toyoura silica sand (S). The density of C is 2.59 g/cm^3. Limestone is precipitation rock, which mainly consists of calcite ($CaCO_3$). The main component of S is SiO_2, with a density of 2.64 g/cm^3 in the absolute dry condition. Raw material of M is extracted from expansive shale rocks followed by grinding, granulation, and calcination. The density in absolute dry condition is 1.60 g/cm^3. Particle size of all aggregates was coordinated into the range between 0.6 mm and 1.0 mm. Before mixing, materials were calculated as a water to cement ratio of 0.5 and the aggregate volume of 0.05. Mixed materials were casted into metal frame in the size of 40×40×160 mm. The samples were de-molded after 24hours of molding, and then cured under water for 14 days. Then, the samples were cut into the prism in the size of 2.5×2.5×5 mm.

(2) Experiment 2

Cement paste with only the Ordinary Portland Cement was used in this experiment. A water to cement ratio is 0.6. The cement paste was mixed and molded into metal frame in the size of 40×40×160 mm. The samples were de-molded after 24 hours of molding, and then cured under water until cutting. After about 12 months of water-curing, the hardened cement pastes were cut into the prism in the size of 2.5×2.5×5 mm for the CT-XRD measurement. Preparation processes for the CT-XRD samples are shown in Figure 3-2. To investigate various alteration mechanism, carbonation test and heating test described in the next section were carried out followed by setting the samples on the jig using epoxy resin. Hereafter, the non-carbonated samples and carbonated samples are described as NP and CP, respectively.

3.2.2 Test procedure

(1) Experiment 1

Heating test was carried out using electronic furnace with a temperature control program in Experiment 1. The rate of heat increase was set at 10 ℃ per minute until the target maximum temperature was reached. The maximum temperature was maintained for 2 hours and the rate of heat decrease was also set at 10 ℃ per minute until room temperature. The target maximum temperature was 400, 600, and 800 ℃. These temperature range was selected because it was expected to occur significant crack propagation due to thermal expansion of aggregate. In order to check the minerals of aggregate and verify the result of XRD on aggregate, heating only aggregate was carried out followed by Powder XRD.

(2) Experiment 2

Before the CT-XRD measurement in Experiment 2, samples were carbonated doing the following procedure; samples were left in a container inside constant temperature furnace under 100 ℃ condition. 99% CO_2 gas was injected into container per 1 day and this process was continued for a period of 7 days.

Heating test was carried out using electronic furnace with a temperature control program in Experiment 1. The rate of heat increase was set at 10 ℃ per minute until the target maximum temperature was reached. The maximum temperature was maintained for 2 hours and the rate of heat decrease was also set at 10 ℃ per minute until room temperature. The target maximum temperature was 200, 400, 600, and 800 ℃.

3.2.3 Setup conditions

(1) Non-destructive integrated CT-XRD method

The CT-XRD measurement was carried out in both Experiment. Setup conditions in this

measurement are followings; the extracted energy of X-ray CT measurement was 25 keV. Angle steps during CT measurement were 0.12° with an exposure time of 0.4 s. Image resolution was 2.45 μm/voxel and 2.44 μm/voxel in Experiment 2. The beam size was 0.05 mm in width and 0.3 mm in height. The angle of diffraction (θ) was fixed at 5° and the preset time was 300 s for XRD measurement. Table 3-1 provides the details of setup condition used in these experimental works.

Table 3-1 Details information of the CT-XRD used in this chapter

	Items		Experiment conducted in this chapter	
			Experiment 1	Experiment 2
CT	Instrument arrangement[#]		Current	
	Extracted X-ray energy (keV)		25	
	Angle step (deg.)		0.12	
	Rotation (deg.)		180	
	Number of projections		1500	
	Exposure time (s)		0.4	
	Image reconstruction algorithm		Back Projection Procedure	
	Total number of cross-sectional image		1440	
	Cross-section image size (Number of pixel)		1920×1920	
	Pixel size	Cross section (μm)	2.45	2.48
		Slice thickness(μm)	2.46	2.44
	Distance[*]	A to B (mm)	600	
		B to C (mm)	30	
XRD	Slit size	S1 (Width × Height)	0.05 mm×0.30 mm	
		S2 (Width × Height)	0.025 mm×3.00 mm	
		S3 (Width × Height)	0.15 mm×10.00 mm	
	Distance	S1 to sample (mm)	800	
		sample to S2 (mm)	170	
		S2 to S3 (mm)	440	
	Diffraction angle (θ)		5°	
	Preset time (s)		300	

* Current A=Mono-Crystal, B=Sample, C=Camera

[#] See Figure 2-3

(2) Powder X-ray diffraction

Powder X-ray diffraction (P-XRD) was used to identify the crystalline phases of the cement paste and verify the data from the CT-XRD in both Experiment. Samples were grinded into powder in a diameter of less than 100 μm and P-XRD measurement was carried out soon after grinding. XRD data were recorded using SmartLab produced by Rigaku. The scanning range was 2θ = 10° to 60° degrees with a 0.01 step scan and a scanning speed of 5.5 degrees per minute. The diffraction profile was acquired and analyzed using powder diffraction analysis software "PDXL" from Rigaku.

3.3 IMPROVEMENT OF IMAGE ANALYSIS

3.3.1. Results of CT measurement

Figure 3-1 ~ 3-8 shows two representative cross section images for each specimen. C-800°C sample was broken and couldn't be measured. This is discussed in next section. Each slice was processed a matrix size into 1320 × 1320 pixels. At a glance, the phases are easily distinguishable; all types of aggregate, cement paste, crack and void. According to M series, it can be seen that air void was also included inside aggregate. It can be considered that this was

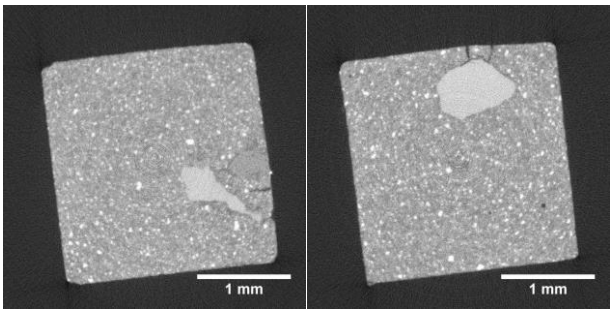


Figure 3-1 Cross Sectional Images: C: Limestone-400°C

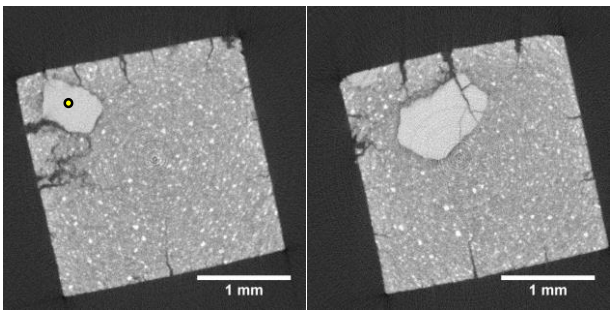


Figure 3-2 Cross Sectional Images: C: Limestone-600°C

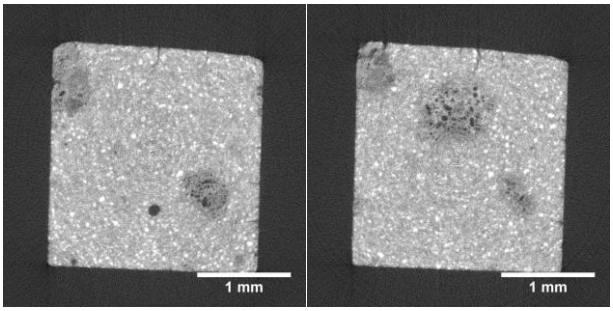


Figure 3-3 Cross Sectional Images: M: Mesalite-400°C

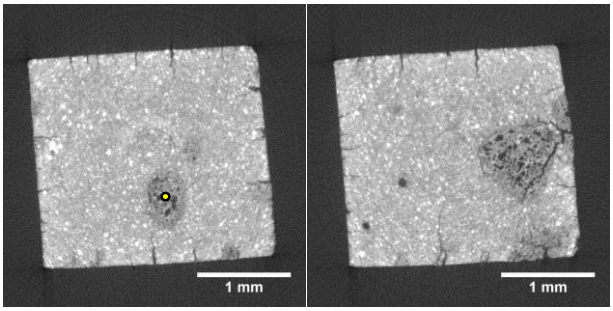


Figure 3-4 Cross Sectional Images: M: Mesalite-600°C

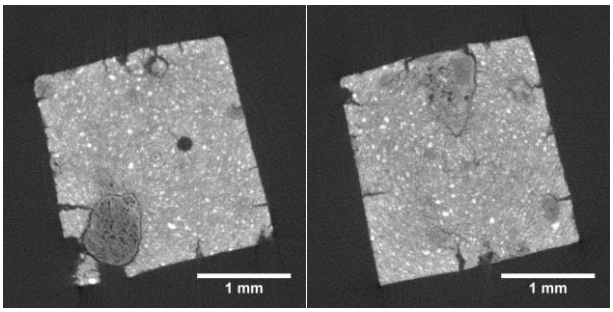


Figure 3-5 Cross Sectional Images: M: Mesalite-800°C

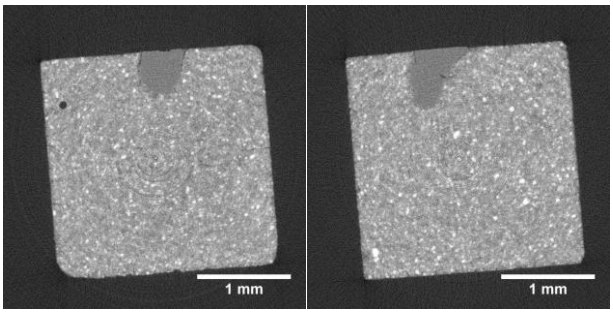


Figure 3-6 Cross Sectional Images: S: Slica sand-400°C

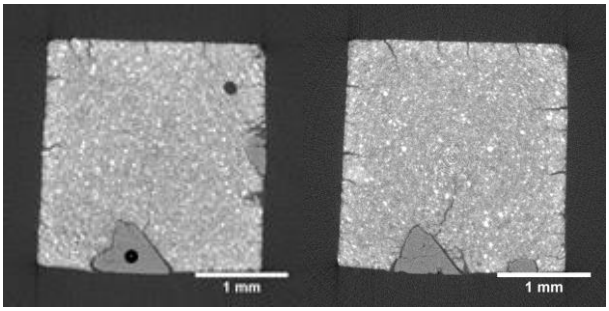


Figure 3-7 Cross Sectional Images: S: Silica sand-600°C

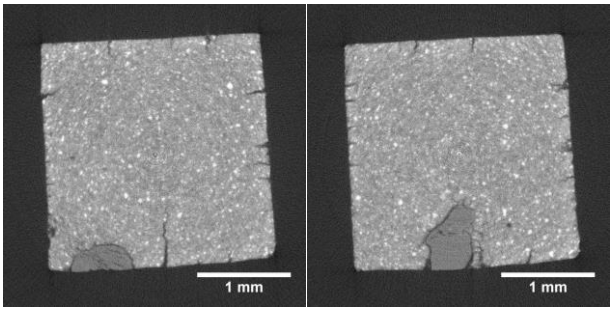


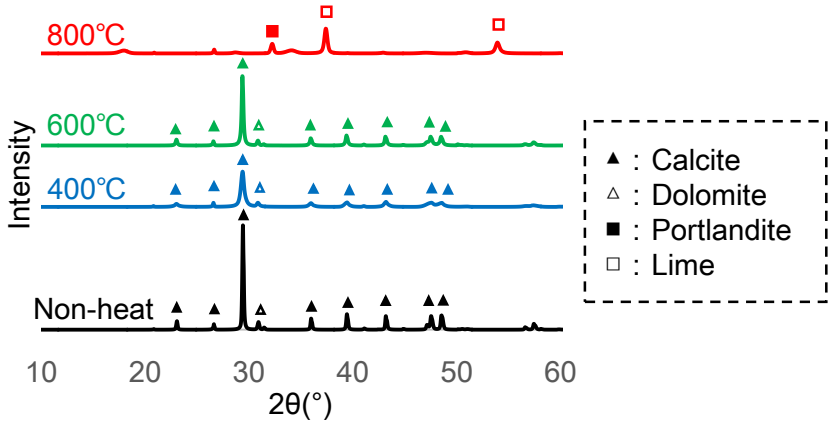
Figure 3-8 Cross Sectional Images: S: Silica sand-800°C

formed during manufacturing process. Concerning 400°C series, cracks can be seen but propagation was stopped at the top of aggregate which is close to outer edge of sample. As for 600°C, it can be found that crack propagation is deeper than 400°C series. Moreover, C-600°C and M-600°C shows that crack propagation penetrates through aggregate. In terms of 800°C, more significant crack propagation than 600 °C series cannot be seen. The markers indicated in 600 °C series are XRD point to do verification. This result is discussed in section 3.4.2.

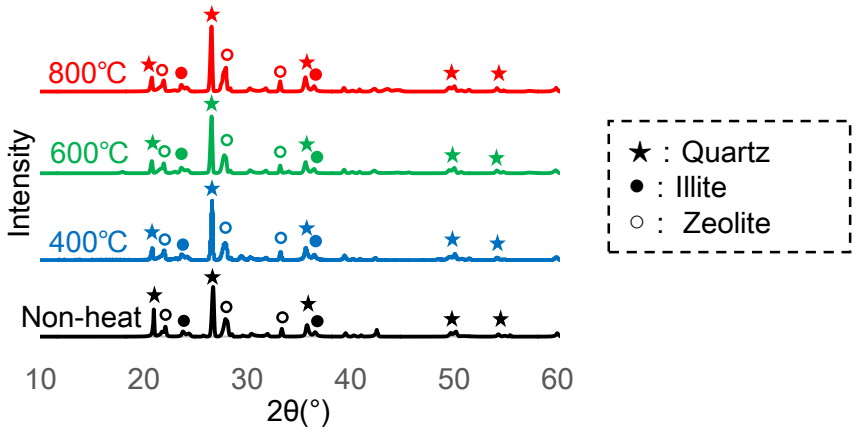
3.3.2. Results of Phase segmentation

(1) Identification of minerals

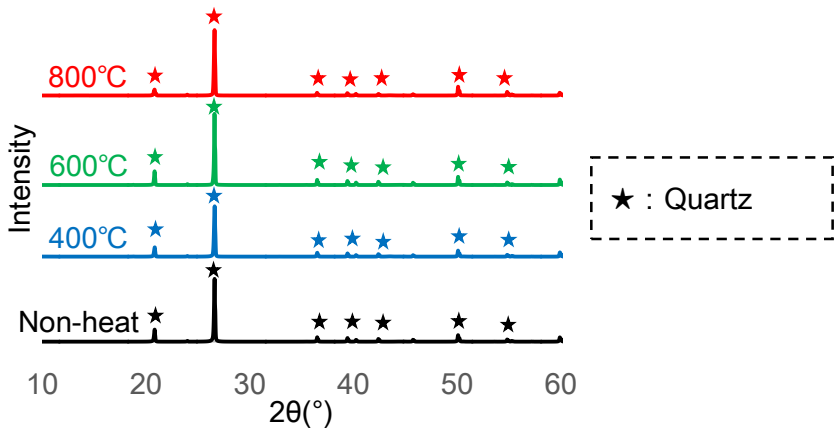
Figure 3-9 shows XRD profiles of powder aggregate by temperature. According to C series, the peaks of Calcite are distinct, and small peaks of Dolomite can be found in the profiles except 800°C. Generally, a small amount of Dolomite is mixed in Limestone [1]. In the profile of C-800°C, the peaks of Lime are found whereas small peaks of Portlandite can be seen. This indicates that the decomposition of Calcite and rehydration with water vapor in surrounding air occurs at 800°C. This decomposition may also lead to destruction of sample. As for M-series, it can be found that significant change is not found and the peaks of Quartz, Illite, and Zeolite are detected from the profiles. This is consistent with a previous research [2]. Maximum peak in the



(a) C: Limestone



(b) M: Mesalite



(c) S: Silica sand

Figure 3-9 Powder XRD profile of each aggregate by temperature

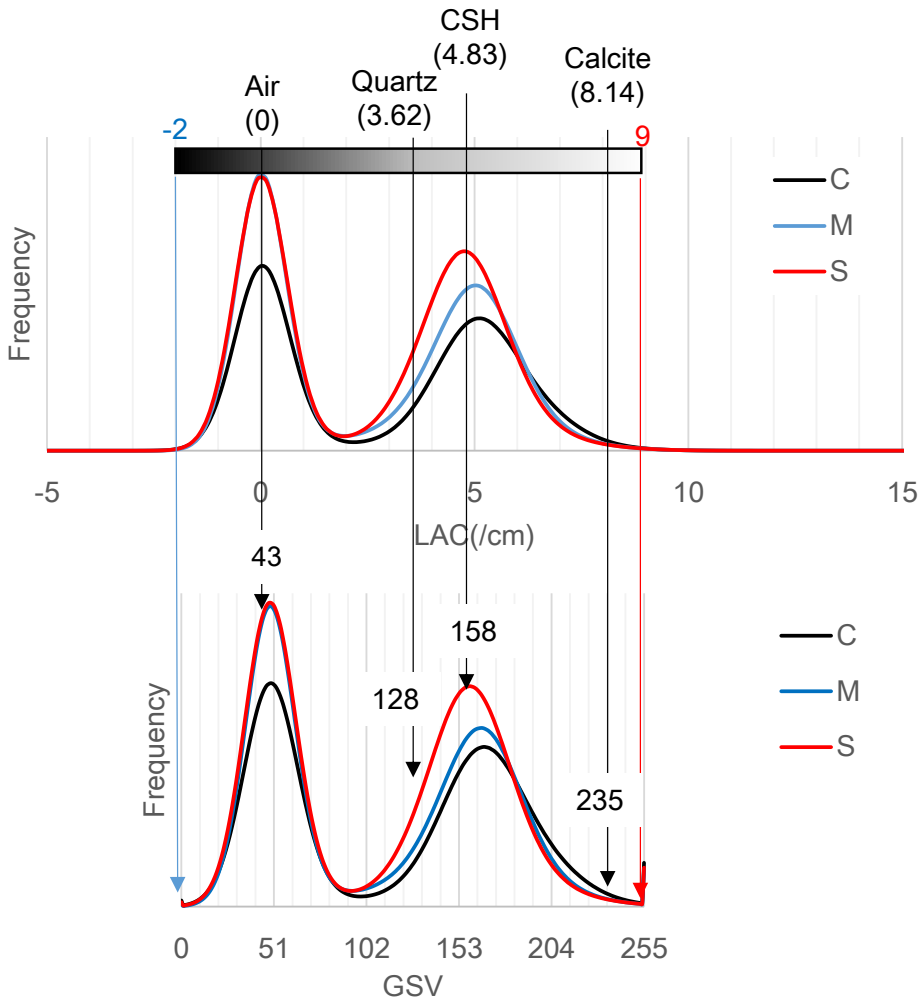


Figure 3-10 CT histogram of the CT images and recalling to 8bit gray scale images

profile positions at 27°, which indicates Quartz. Therefore, main component of M is regarded as Quartz. The profiles of MS-series are consistent with every temperature; only the peaks of Quartz are detected.

(2) Histogram

Figure 3-10 shows the CT histogram of Linear Attenuation Coefficient and rescaling to 8bit gray scale images. LAC of referred minerals was obtained from the NIST database [3] after inputting the chemical compounds and density of targeted constitution. Each LAC was calculated as 8.14 for Calcite, 4.83 for cement paste (regarded as CSH), 3.62 for Quartz, and 0 for Air. It can be said that the peak of air and cement paste is distinctive, but the peak of each aggregate is not distinctive. This is because the aggregate volume is as low as 0.05. In this

analysis, all the CT images were consistently converted to 8bit gray scale images by setting the minimum and maximum to -2 and 9, respectively. These values were determined because frequency was leveled off almost all zero. The minimum and maximum cut-off parameters were determined as the threshold that frequency was leveled off almost all zero, and then 8-bit grayscale images with intensity values that range from 0 to 255 were produced. The GSV corresponding to LAC of targeted constitution is 235 for Calcite, 158 for CSH, 128 for Quartz, and 43 for Air, respectively.

(3) Image processing

(a) Image Filtering

Tentatively, the GSV range of aggregate was set from 20 smaller than the value of targeted aggregate to 20 larger values than it (i.e. 215≤GSV≤255 for Calcite), and binarization was carried out following this range as a trial. Figure 3-11 shows the result of binarization. It can be said that rough morphological descriptions for aggregate are fulfilled. However, many noises are observed in images, especially M and S. In order to improve the signal-to-noise ratio, image enhancement was carried out by referring to [4]. At first, anisotropic diffusion filter was carried out, which can reduce noise in an image while trying to preserve sharp edges and extend to 3D problems. Figure 3-12 shows the histograms before and after filtering. This indicates that the

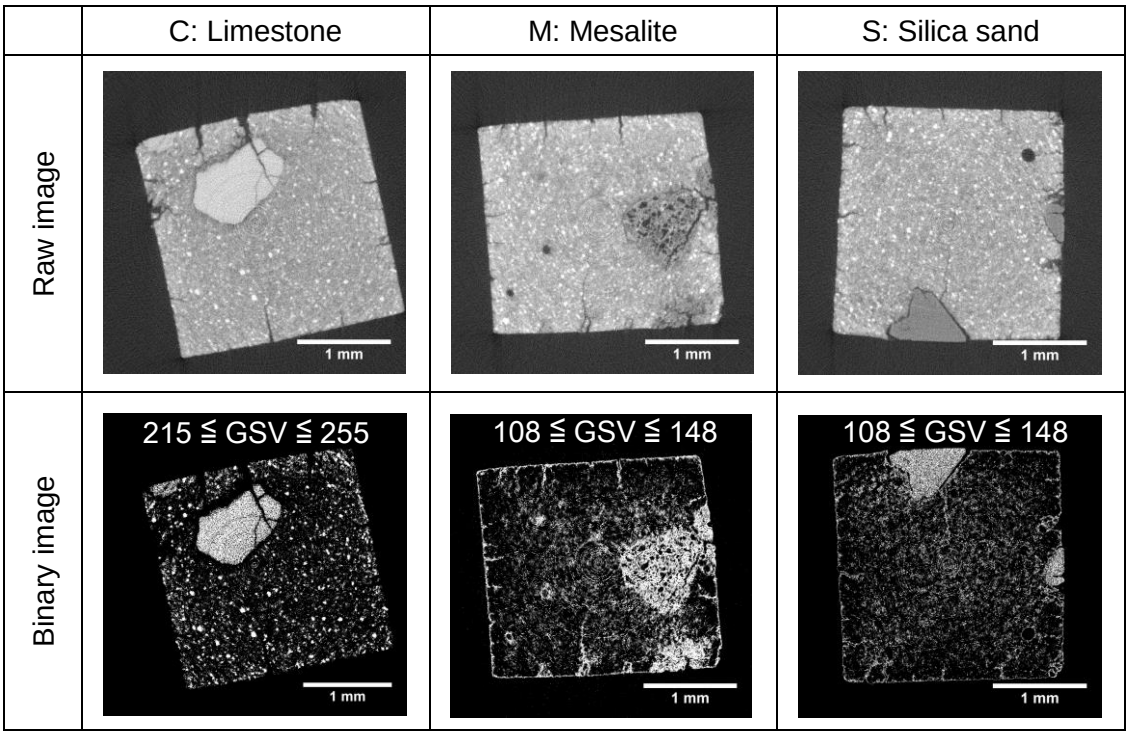


Figure 3-11 Comparison between raw image and binary image

peaks become sharp and therefore aggregate-derived peaks are shown in the histograms. Therefore, thresholds were determined, the intersection between each peak or the intersection of GSV axis. Figure 3-13 shows that the result of binarization from filtered image. This indicates that the noise reduction was appropriately satisfied, but the edges between air, aggregate and cement paste are shown in the image of M and S. Moreover, crack is also extracted from the

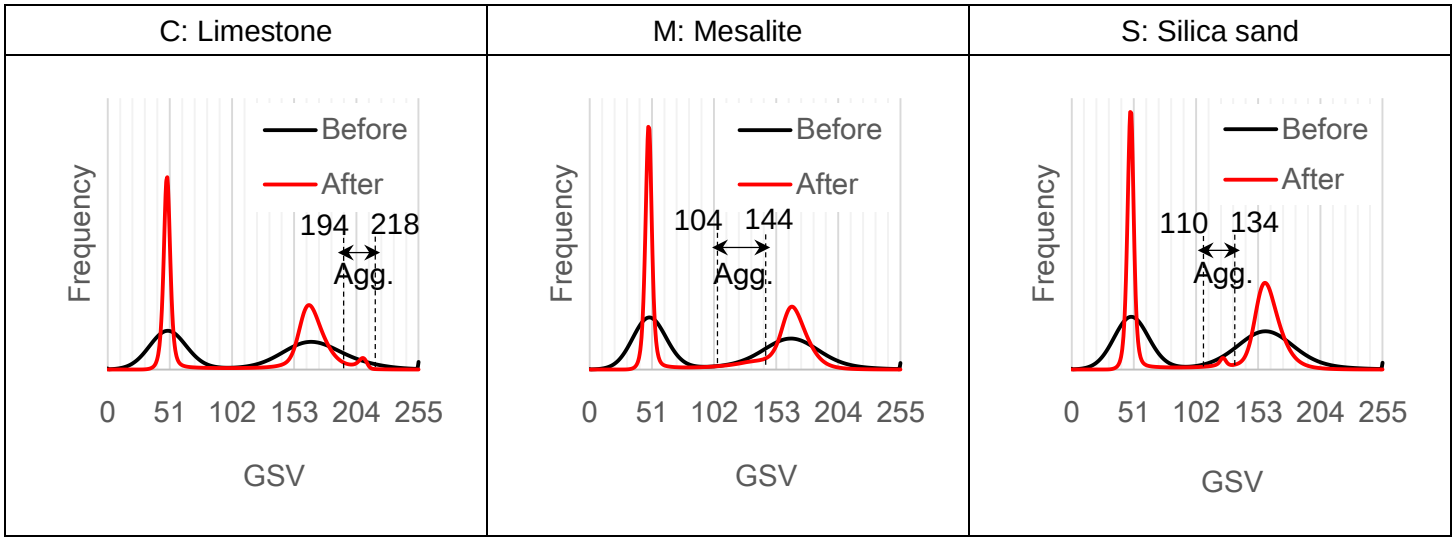


Figure 3-12 Histograms of 600°C series' sample before and after anisotropic diffusion filtering

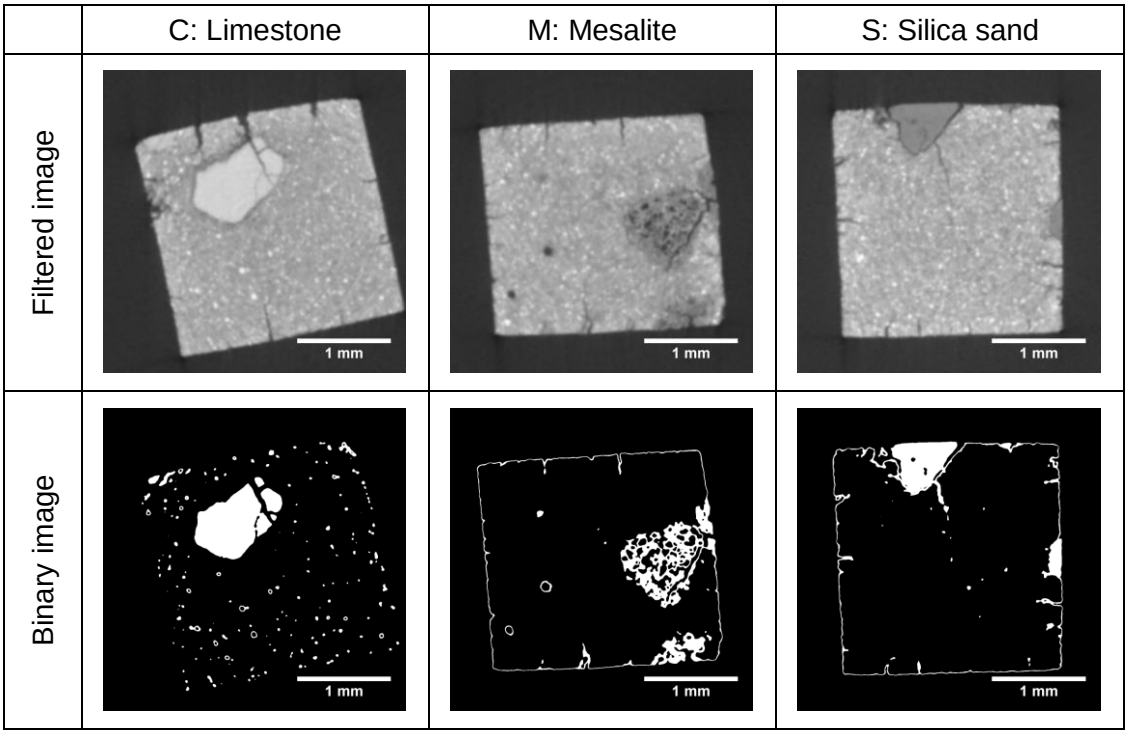


Figure 3-13 Comparison between filtered image and binary image

image of M and S, which means that aggregate and crack cannot be segmented from anisotropic diffusion filtered image. Therefore, based on [4], unsharp mask sharpening filter which enhances edges and partially reverses the smoothing is applied as a second step. Figure 3-14 shows the effect of unsharp mask sharpening filtering including line profile. This indicates that the contrast in phase transition zone becomes higher after unsharp mask sharpening filtering. From this line profile, threshold of air void is determined as 100, and this value or less is treated as air void. Figure 3-15 shows the binary image of void area. It can be said that extraction of

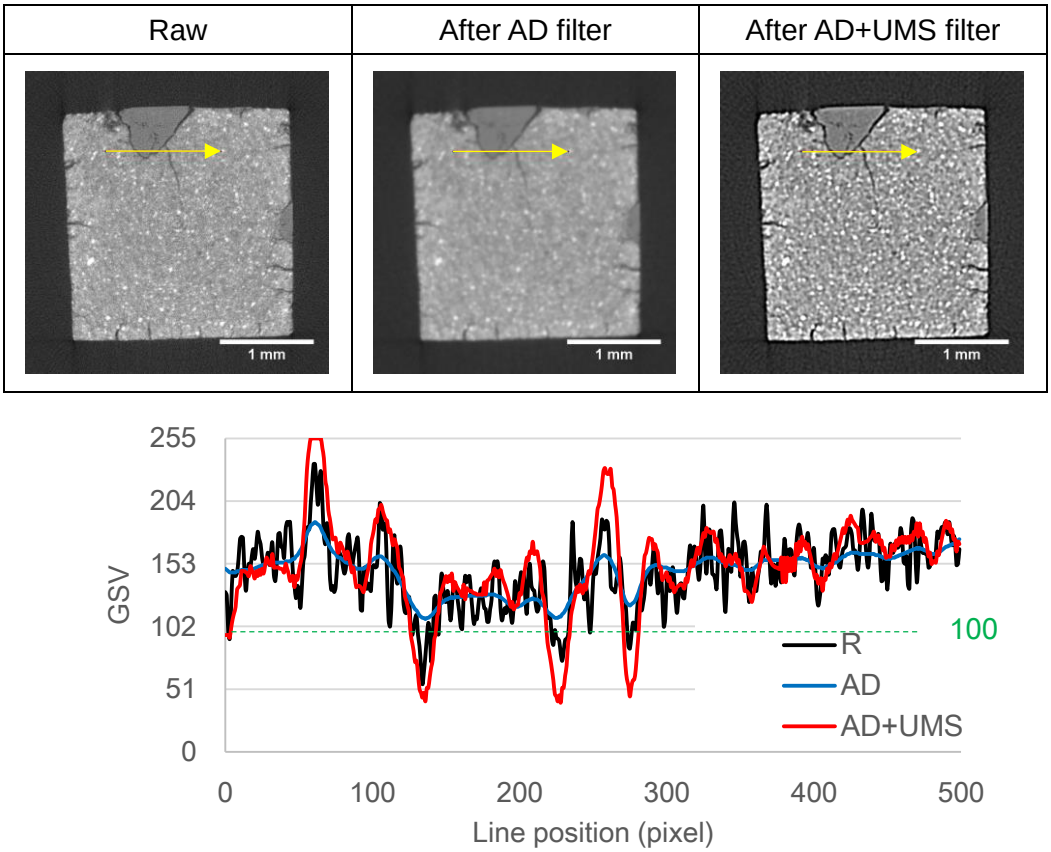


Figure 3-14 Effect of filtering (AD: Anisotropic Diffusion, UMS: Unsharp Mask Sharpening)

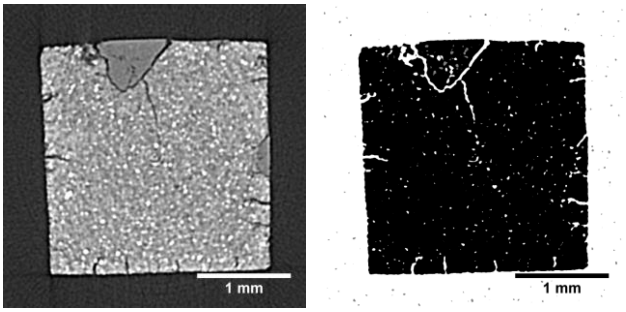


Figure 3-15 Comparison between filtered image and binary image

crack area is adequate. However, if binarization targeting aggregate were carried out as shown in Figure 3-16, morphological description of aggregate is not adequate. Therefore, this filtering can be applied to extract cracking in cement and concrete field

(b) Extraction of crack area

Extraction of crack area to visualize and quantify the amount was applied to binary images. Figure 3-17 shows the illustration of method. First, the total void space could be extracted from the volume of interest (VOI, the region of interest (ROI) across the vertical slice stack), and

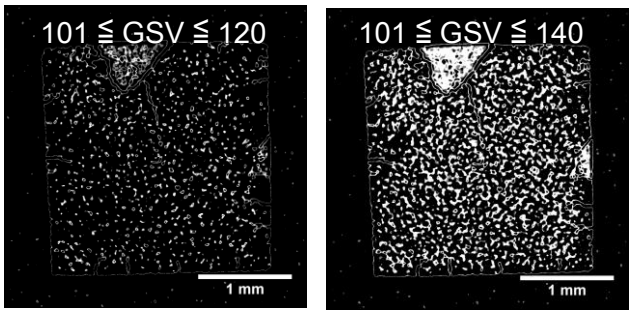


Figure 3-16 Binarization targeting aggregate

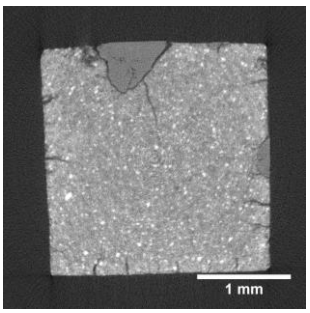
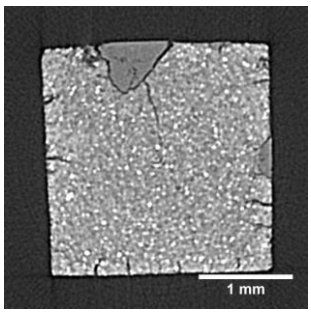
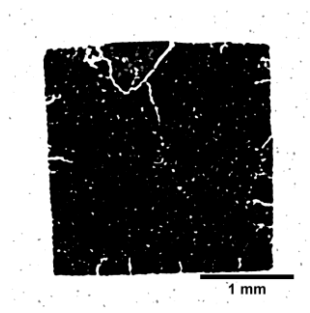
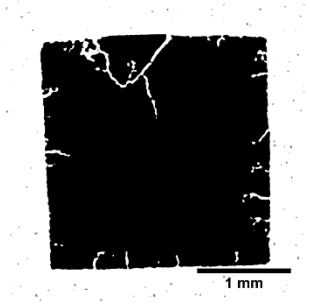
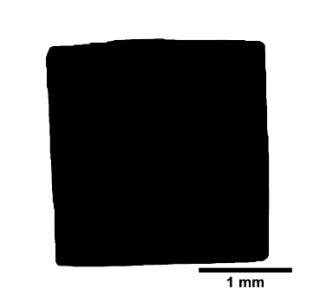
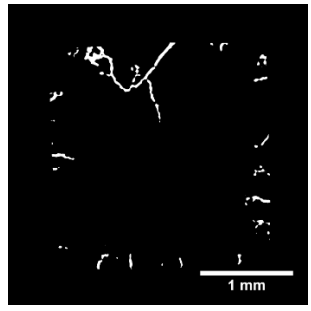
(a) Raw	(b) AD+UMS	(c) binary image showing total void space
		
(d) isolated crack	(e) background image	(f) isolated crack without background
		

Figure 3-17 Method for extracting cracking area

binary white and black that correspond to void space and other area, respectively (Figure 3-17(c)). Next, cluster labeling was carried out to identify crack area in the VOI. In this study, crack area was identified as void spaces connected to only air outside specimen (Figure 3-17(d)). Then, subtraction of background, which can be made by doing morphological closing operation to fill void space (Figure 3-17(e)), was applied to crack area. Finally, only crack area inside specimen was obtained (Figure 3-17(f)).

(c) Extraction of aggregate

As shown in Figure 3-13, rough morphological feature of aggregate can be extracted from binary images. However, when cluster labeling was applied to extract only aggregate area (shown in Figure 3-18), the edge still remained in the image of M and S whereas only aggregate area was extracted in the image of C. This is because the value range of aggregate in C exists at larger than cement paste whereas that in M and S exists between void and cement paste. Therefore, in order to extract only aggregate in M and S, the following procedure were carried out as shown in Figure 3-19. First, subtraction of background was done to eliminate the outer edge of sample. In addition, subtraction of crack area was done to eliminate almost all crack area connected to aggregate. However, some voxels remained in the images. Then, morphological opening operation was applied to eliminate surplus voxels and afterwards

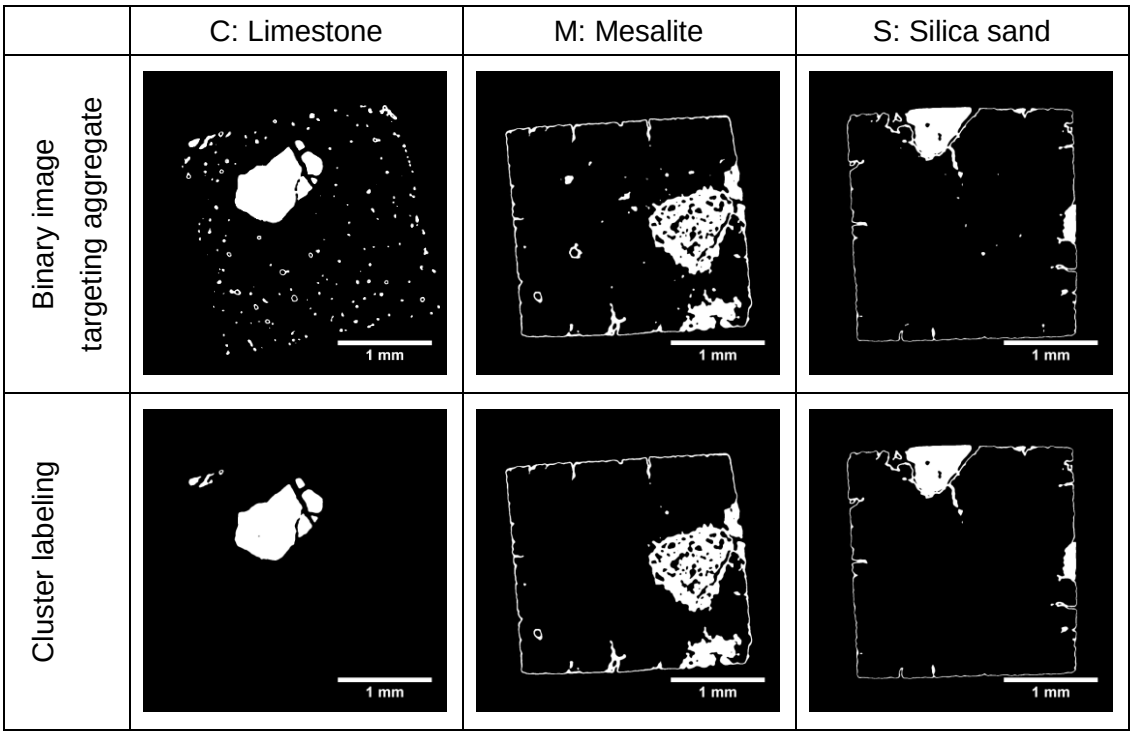


Figure 3-18 Result of cluster labeling

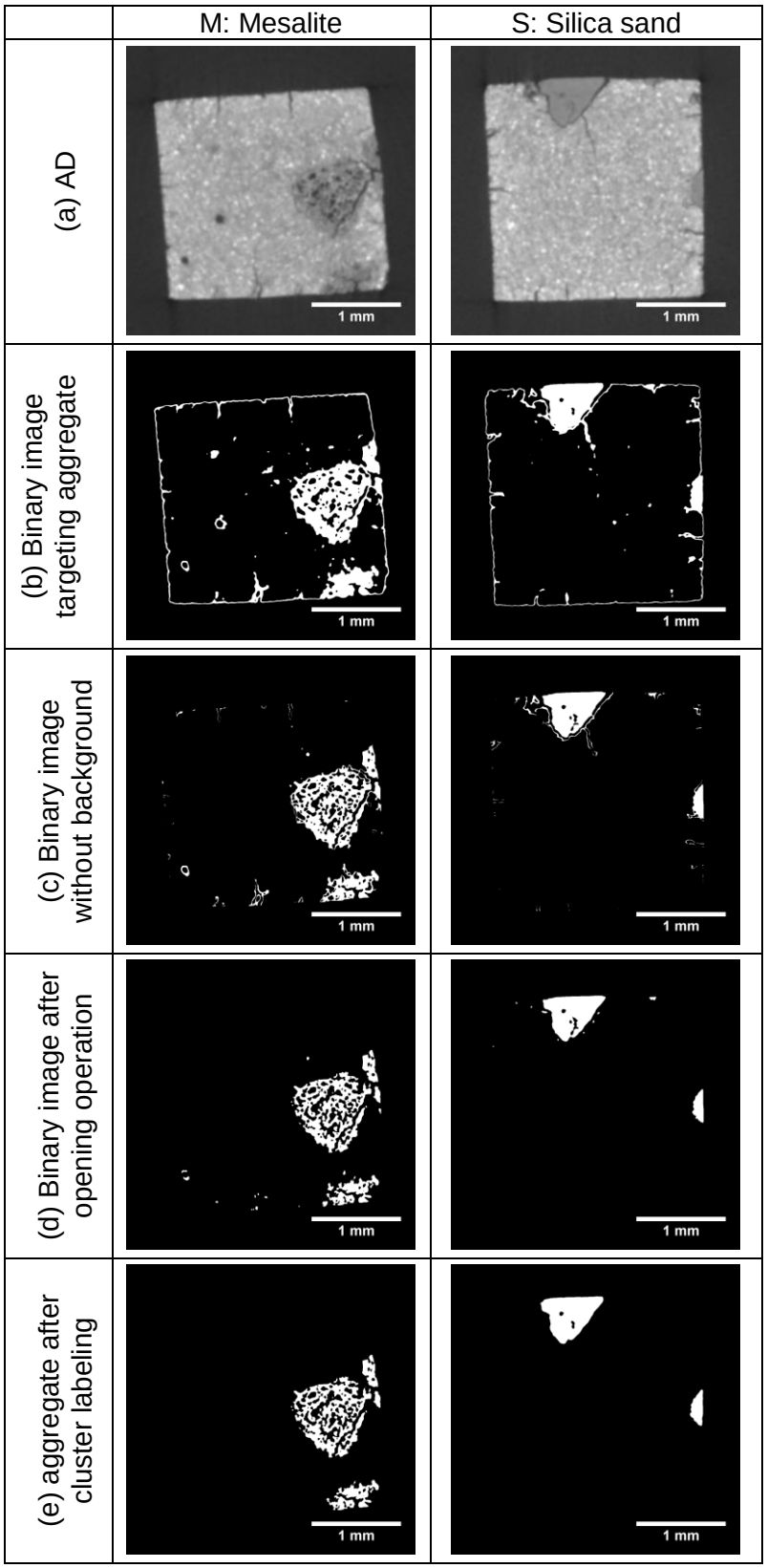


Figure 3-19 Method for extracting aggregate for M and S

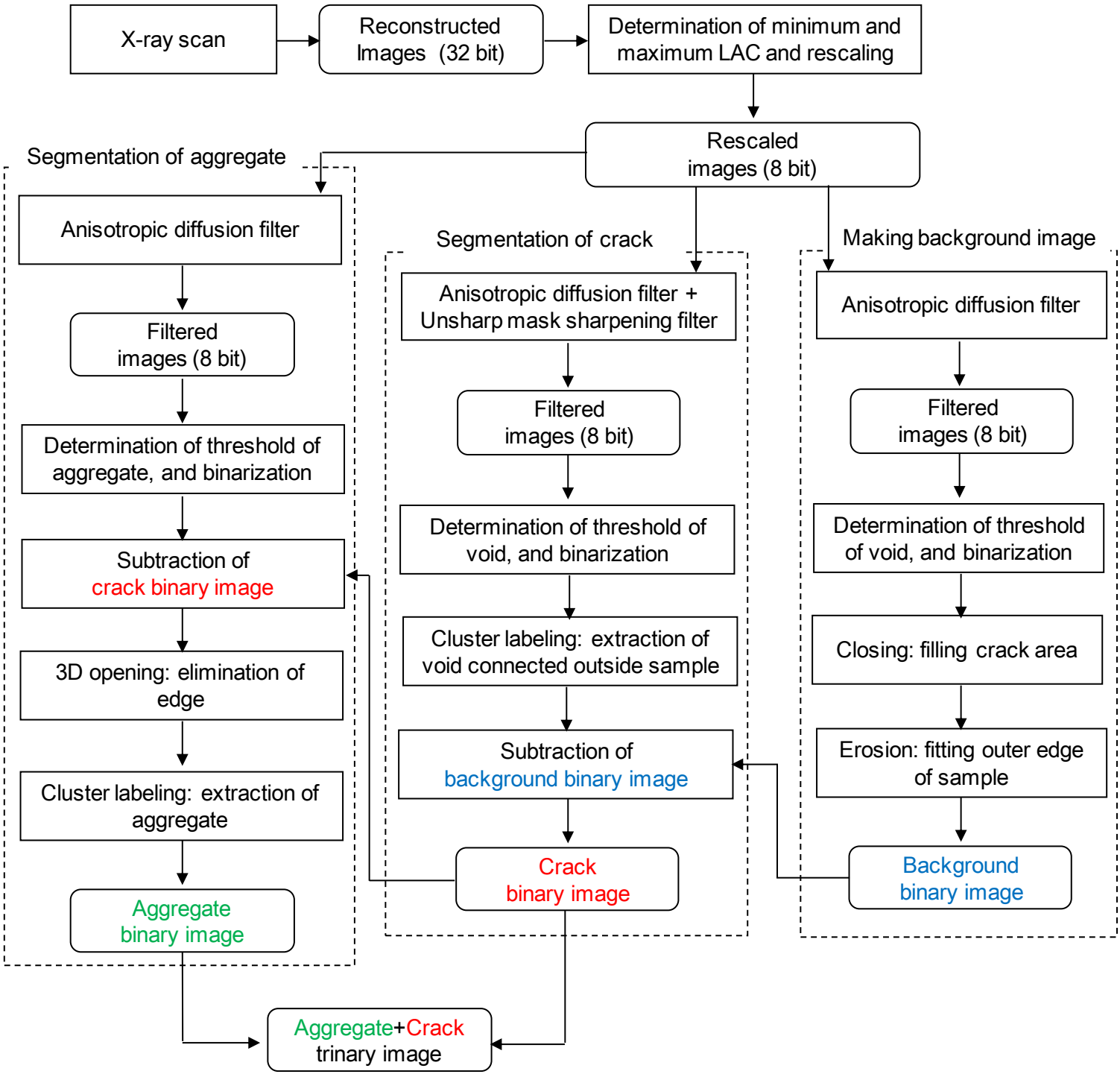


Figure 3-20 Segmentation procedure proposed in this study

aggregate area can be segmented.

Figure 3-20 shows the flowchart of segmentation procedure proposed in this study.

(d) 3D imaging

Figure 3-21 shows the example of 3D imaging of sample, aggregate, and crack area in 600°C-series. In this study, ROI was set as continuous 300 slices including significant aggregate. Using this images, quantitative analysis was carried out explained in next section.

3.3.3. Effect of heating on quantitative analysis of crack behavior

Aggregate ratio (Ra) and crack ratio (Rc) were calculated using the following formulas;

$$Ra=Va/Vs$$

$$Rc=Vc/Vs$$

where Va is the total number of voxels of aggregate, Vc is that of crack, and Vs is that of sample.

In order to calculate the maximum, minimum and mean of crack width in isolated crack, plugins in BoneJ [5] called Thickness [6] was applied. The output of the Thickness plugin is the thickness of a 3D object which is displayed in the form of a thickness distribution and thickness map as shown in Figure 3-22. In this study, the 3D object is the crack structure and the thickness is defined as the crack width.

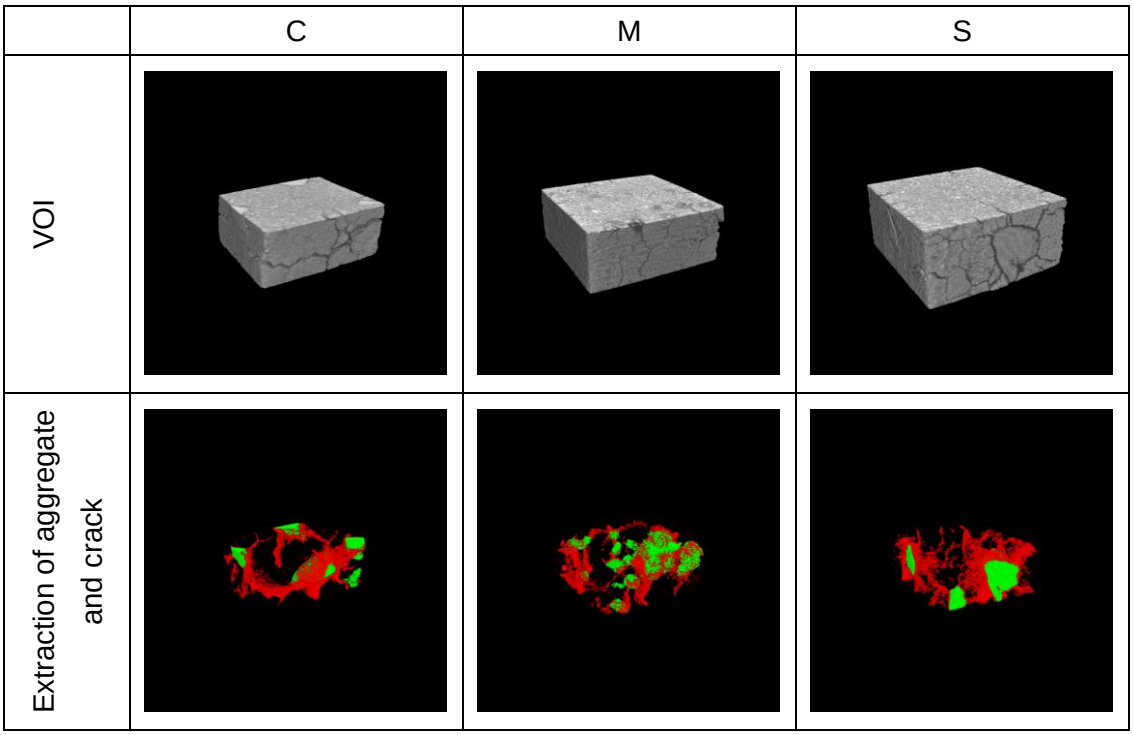


Figure 3-21 3D imaging (green: aggregate, crack: red)

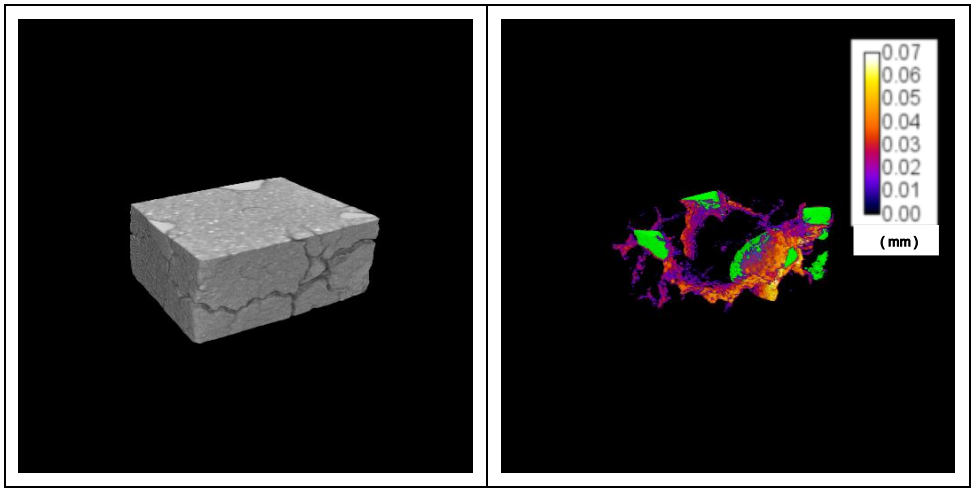


Figure 3-22 Crack width distribution

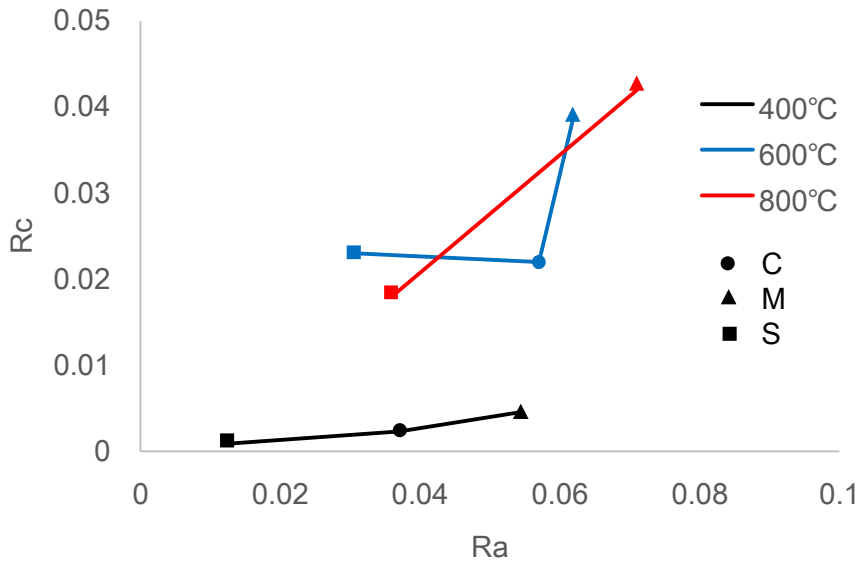


Figure 3-23 Relationship between aggregate ratio (Ra) and crack ratio (Rc)

Figure 3-23 shows the relationship between Ra and Rc. It indicates that crack ratio increased drastically in 600 °C or more. It derived from the expansion of aggregate and decomposition of portlandite. There is a little difference of Rc between C and S whereas thermal expansion coefficient of S is higher than that of C [7]. This might be derived from that aggregate ratio is low and particle size is also small. However, M has the highest Rc among all of aggregate types at any temperatures. It can be considered that the generated crack was connected to void inside aggregate. Figure 3-24 shows the relationship between Maximum temperature and mean crack width. According to 400 °C series, S has the lowest mean crack width whereas Ref. [7] reported that the thermal coefficient of siliceous sand is higher than Limestone sand. It might be derived

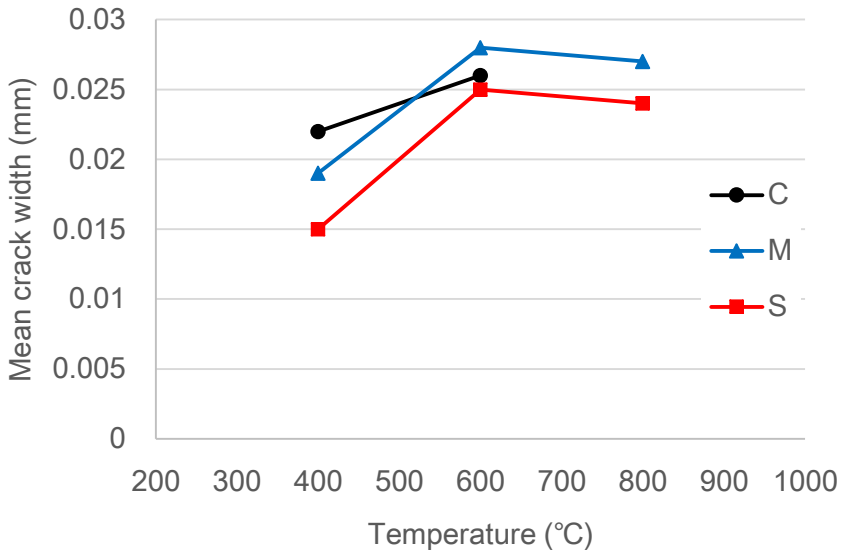


Figure 3-24 Relationship between maximum temperature and mean crack width

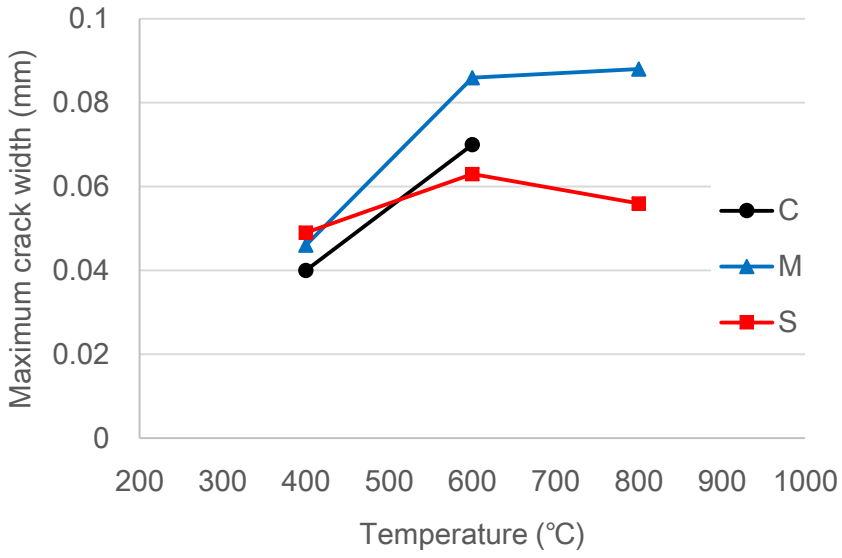


Figure 3-25 Relationship between maximum temperature and maximum crack width

from that Ra of S-400°C is extremely low. In terms of 600 °C series, mean crack width of all aggregate types becomes higher than those of 400 °C. In addition, M has the highest mean crack width among 800 °C series. Moreover, among 800 °C series, M is higher mean crack width than S. It can be considered that the generated cracks were connected to void inside aggregate and subsequently mean crack width becomes larger. Compared between 600 °C and 800 °C, mean crack width becomes lower. Generally, quartz phase change from β to α occurs at 573 °C [8],

which causes brash expansion, and after that, expansion ratio is stable while cement paste keeps on shrink more than 100 ℃ [9]. This might be why crack width becomes smaller between 600 ℃ and 800 ℃. Figure 3-25 shows the relationship between maximum temperature and maximum crack width. The same trend can be seen as the relationship between maximum temperature and mean crack width. But the maximum crack width exceeds more than 0.08 mm on M-600℃ and M-800℃ while other types of aggregate series are 0.06 mm at 600 ℃ and 800 ℃.

It can be concluded that the segmentation procedure of aggregate and crack area was proposed from X-ray images, which can extend to quantitative analysis.

3.4. VERIFICATION OF THE RESULTS OF XRD

3.4.1 XRD target on this study

From Experiment 2, the ROI was set in the center of each sample, which consists of continuous

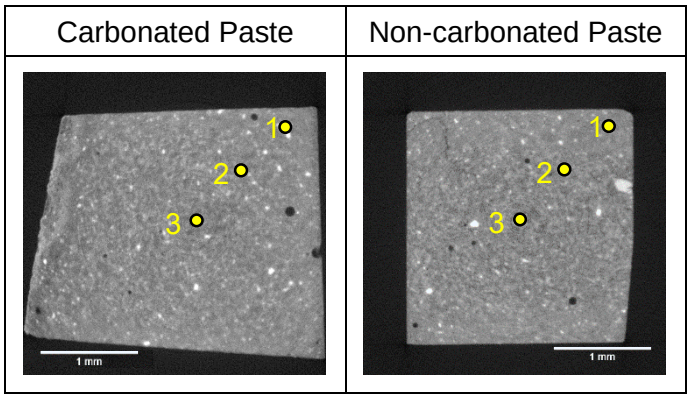


Figure 3-26 Cross Sectional Image: Non-heat

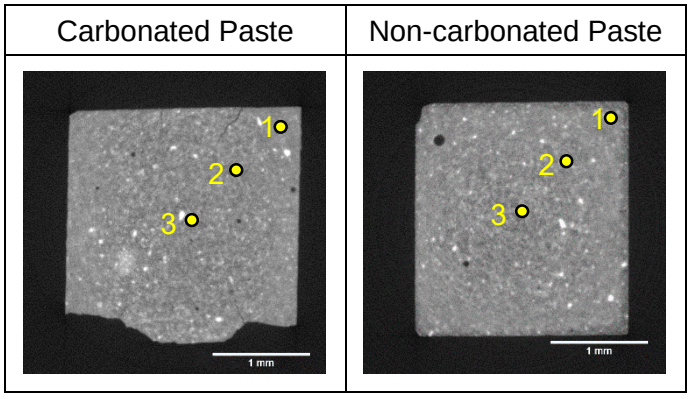


Figure 3-27 Cross Sectional Image: 200℃

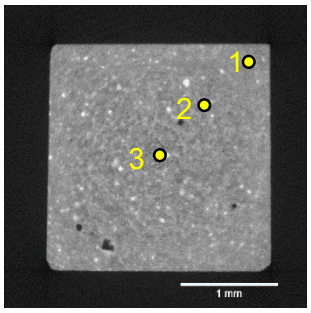
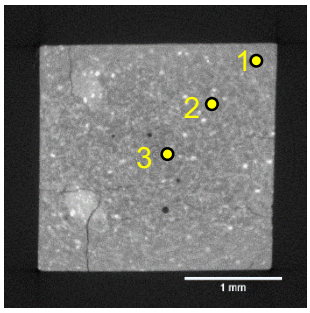
Carbonated Paste	Non-carbonated Paste
	

Figure 3-28 Cross Sectional Image: 400℃

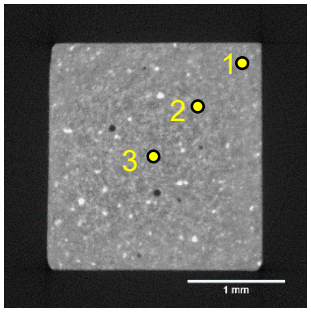
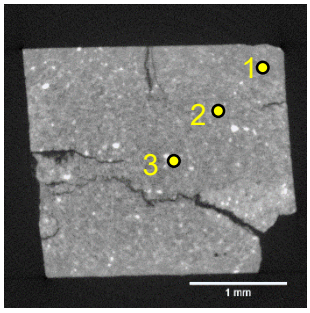
Carbonated Paste	Non-carbonated Paste
	

Figure 3-29 Cross Sectional Image: 600℃

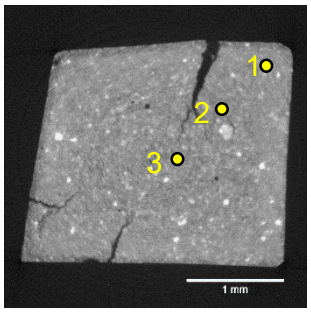
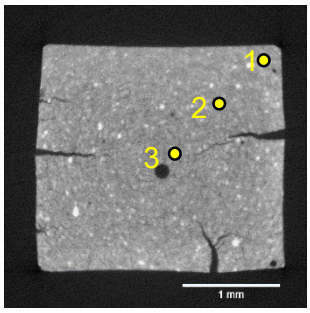
Carbonated Paste	Non-carbonated Paste
	

Figure 3-30 Cross Sectional Image: 800℃

300 slices. Figure 3-26 ~ 3-30 shows micro-tomographic images of each sample. The cross section is located in the middle height of sample. Light gray indicates the cement paste and dark color represents air, voids, and crack. Each slice was processed a matrix size into 1280 × 1280 pixels. According to NP-series, the images show that some cracks were observed in NP-400 °C

and more cracks clearly can be seen in NP-600 °C and NP-800 °C. As for CP-series, only CP-800 °C has significant cracks. Cracks were formed from the outer edge into the center. It can be inferred from that the decomposition of portlandite started to occur higher than 400 °C and triggered the cracking in N-series. In addition, calcite or C-S-H decomposed in CP-series at 800 °C, which may result in cracking. This is discussed in the next section.

3.4.2 Results of XRD measurement

ROIs were determined for XRD measurements as Point 1 to Point 3 from the corner to the center (shown as circle in Figure 3-26 ~ 3-30). Figure 3-31 ~ 3-35 shows series of XRD profiles listed in order of temperature; P-XRD, Point 1, Point 2, and Point 3 are shown from top to bottom. Figure 3-36 shows the profile of XRD point shown in Figure 3-2, 3-4, and 3-7 compared with P-XRD of aggregate heated at same temperature.

(1) Carbonated Paste (CP)-non heat

As for C-NH, it can be found from P-XRD profile that, the peaks of Calcite are distinct whereas some peaks of Portlandite can be seen. Moreover, small peaks of Vaterite also can be found. Groves et al. [10] observed calcium carbonate is formed mainly in outer product regions of C-S-H as microcrystalline Vaterite and Calcite, and residual Portlandite embedded in Vaterite is also observed using TEM. Moreover, Galan et al. [11] proposed the mechanism that Porlandite crystals develop a layer of calcium carbonate whose properties of continuity and thickness depend on the external RH. Kurata et al. [12] implied that the same mechanism occurred in high water cement ratio (60%) by atmospheric exposure test for 10 years. These can support the reasons why the peaks of Vaterite were also detected. A small peak of Belite was also detected, which is derived from the presence of anhydrated cement phases.

With regard to the profile of Point 1, the peaks of Calcite are distinct and a peak of Belite is also confirmed. On the other hand, the peaks of Portlandite cannot be found. On the other hand, profiles of Point 2 and Point 3 exhibit that the peaks of Portlandite are distinct whereas the peaks of Calcite are very weaker than that of Point 1. These profiles reveal that carbonation progressed at the surface layer due to the reaction of atmospheric CO_2 and Portlandite. The presence of Belite is also derived from anhydrated cement particles.

(2) Non-carbonated Paste (NP)-non heat

The P-XRD profile shows that the peaks of Portlandite are significant although some peaks of Calcte and Vaterite can be identified. According to the profile of Point 1, the peaks of Calcite and Vaterite are identified without no peaks of Portlandite. In contrast, the peaks of Portalndite can be detected in both Point 2 and Point 3 while the peaks of Calcite are less significant than

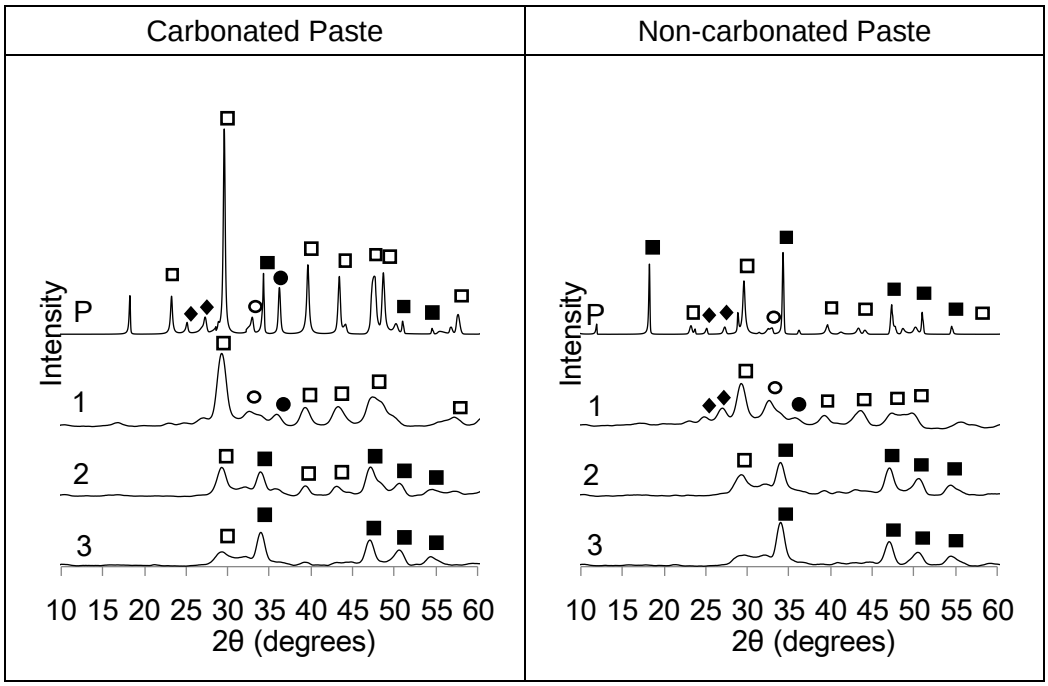


Figure 3-31 XRD profile: Non-heat (alite:▲, belite:○, portlandite:■ , calcite:□ , vaterite:♦ , lime:●)

C-NH. Therefore, it can be concluded that air-induced carbonation occurred at the surface layer in contact with CO_2 to the depth of less than 0.6 mm.

(3) CP-200 °C

The profiles of C-2 has almost all the same characteristics as C-NH. It can be said that the decomposition of carbonated cement hydration products was not observed at 200 °C. The peaks of Calcite were found out in the profile of Point 3, which indicates that carbonation was progressed up to Point 3. Ref. [13] indicated that carbonation depth is proportional to elevated temperature, which supports the results in this research.

(4) NP-200 °C

With regards to the profiles of N-2, no significant difference can be observed compared with N-NH, which indicates that exposure of this temperature did not affect the decomposition of this cement hydration system series.

(5) CP-400 °C

It can be found from the profiles of C-4 that changes are hardly ever observed in comparison with those of C-NH. The exposure of 400 °C did not affect the decomposition of initial carbonated state.

(6) NP-400 °C

The same trends as previous sections can be seen in the profiles of N-4, and the same finding can be explained in this section.

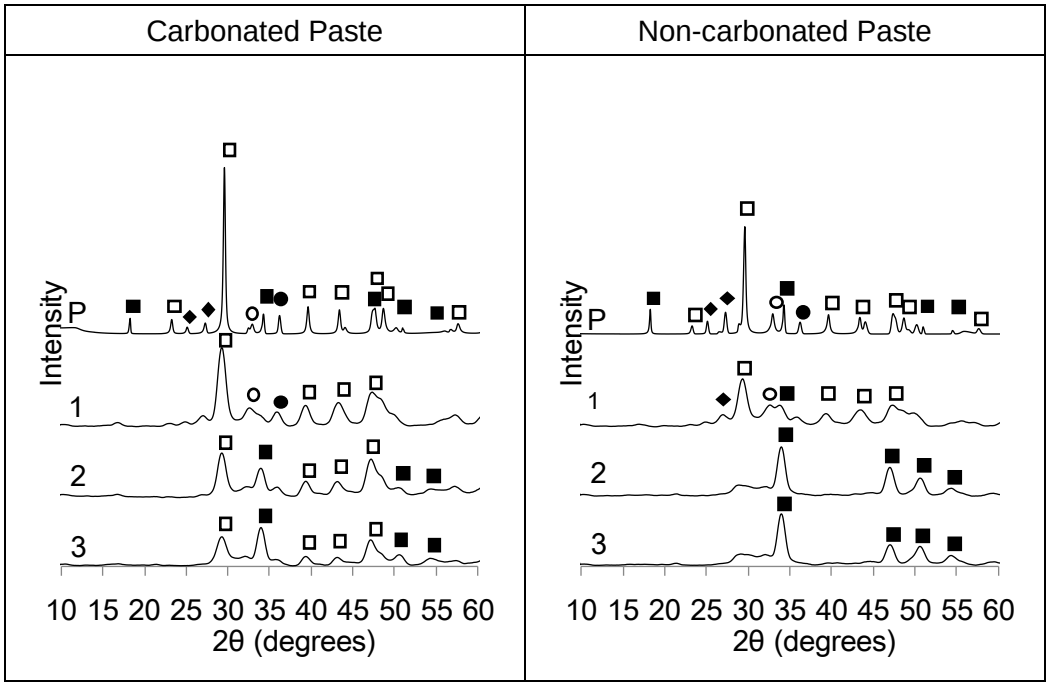


Figure 3-32 XRD profile: 200℃ (alite:▲, belite:○, portlandite:■ , calcite:□ , vaterite:♦ , lime:●)

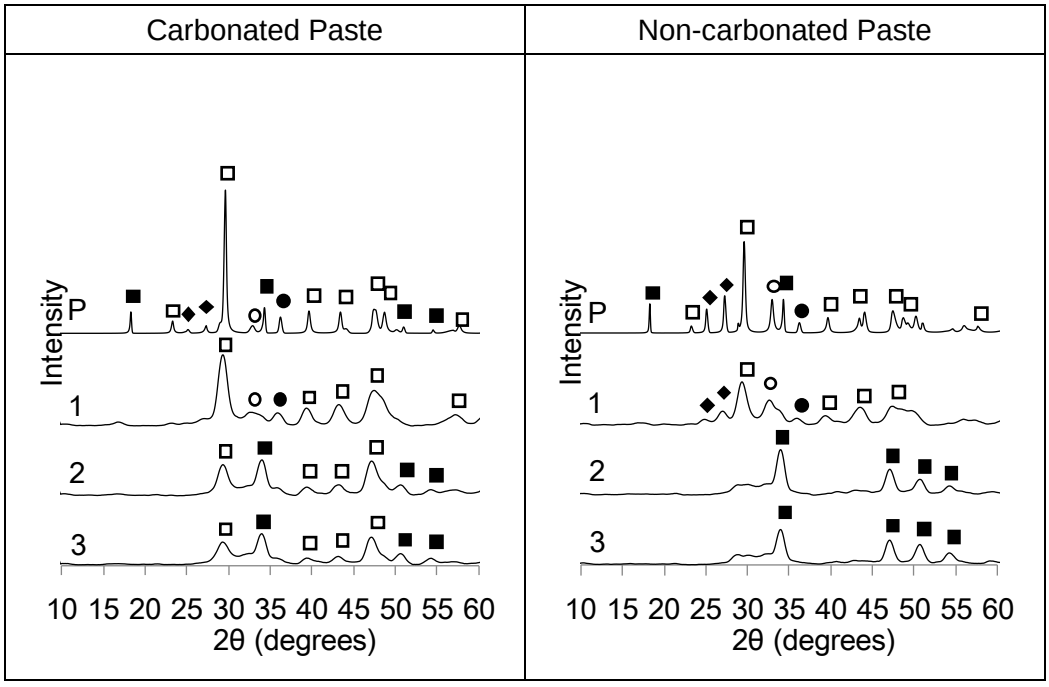


Figure 3-33 XRD profile: 400℃ (alite:▲, belite:○, portlandite:■ , calcite:□ , vaterite:♦ , lime:●)

(7) CP-600 °C

All peaks are consistent with each profile except the existence of peak in P-XRD at 23°. Almost all peaks have good matches with the peaks of Calcite. A peak of C_2S and Lime can be found, respectively. The peaks of Vaterite was not observed while it was observed in the profiles of less

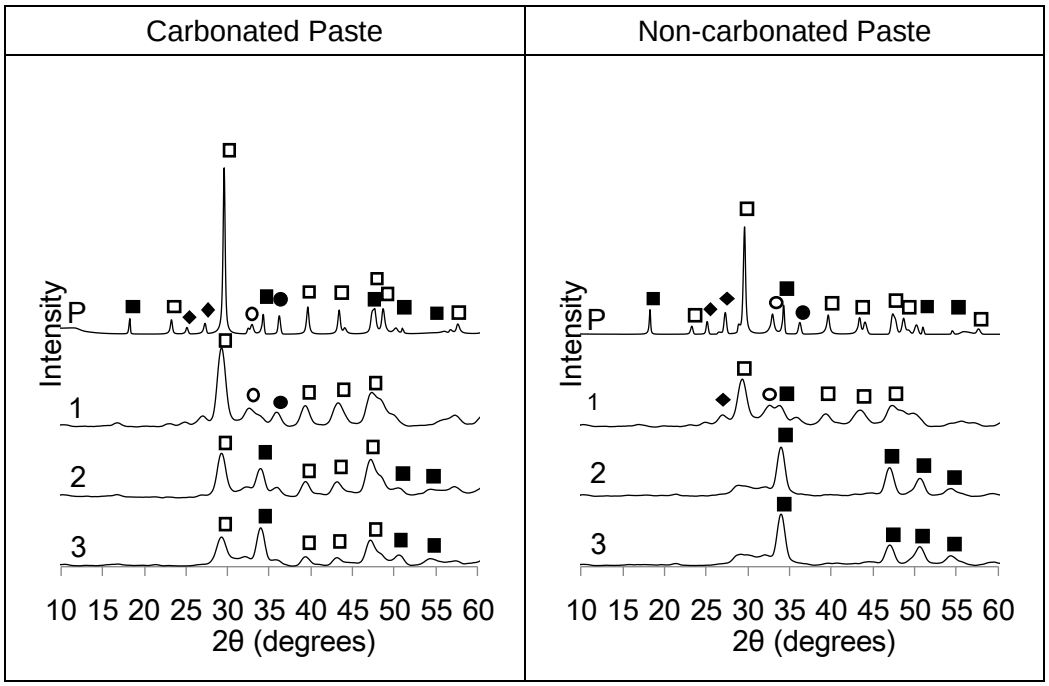


Figure 3-34 XRD profile: 600℃ (alite:▲, belite:○, portlandite:■ , calcite:□ , vaterite:♦ , lime:●)

than 400°C. It is known that Vaterite transforms to Calcite around 500 °C [14], which confirms this result.

(8) NP-600 °C

Unique trend can be found in the profiles of N-6. Although the peaks of calcite and one peak of Lime and C_2S are significant in both P-XRD and Point 1, the peaks of Vaterite which was detected in the samples heated at less than 400 °C. This fact is consistent with the result of C-6. Moreover, the peaks of Portlandite disappeared in P-XRD while the peaks of Portlandite in the broader and weaker state can be seen in Point 2 and Point 3. Castellote et al. [15] revealed that Portlandite with less crystalline was reformed due to the reaction of Lime with water vapor when cooling procedure. Therefore, it can be considered that this reaction occurred inside the sample due to the presence of moisture like free water. In addition, Scrivener et al. [16] pointed out that the friction during intense grinding processes in preparing the powder sample may cause loss of crystal water and changes in the phase assemblage. Thus, some crystalline d structure was easily destroyed during grinding procedure.

(9) CP-800 °C

The peaks of C_3S and C_2S can be found in all profiles consistently. It can be considered that these products were derived from the decomposition of C-S-H, being consistent with previous researches [17, 18]. The profiles in the CT-XRD have the peak of Lime while P-XRD has the peaks of Calcite. This fact indicates that the reaction of Lime with CO_2 in air progressed rapidly because the hydration was not stopped beforehand.

(10) NP-800 °C

The same trends as C-8 was observed in the profiles of N-8, which is derived from the decomposition of C-S-H. Moreover, small tiny peaks of Portlandite were observed in P-XRD. It might be derived from the contact with water vapor in air.

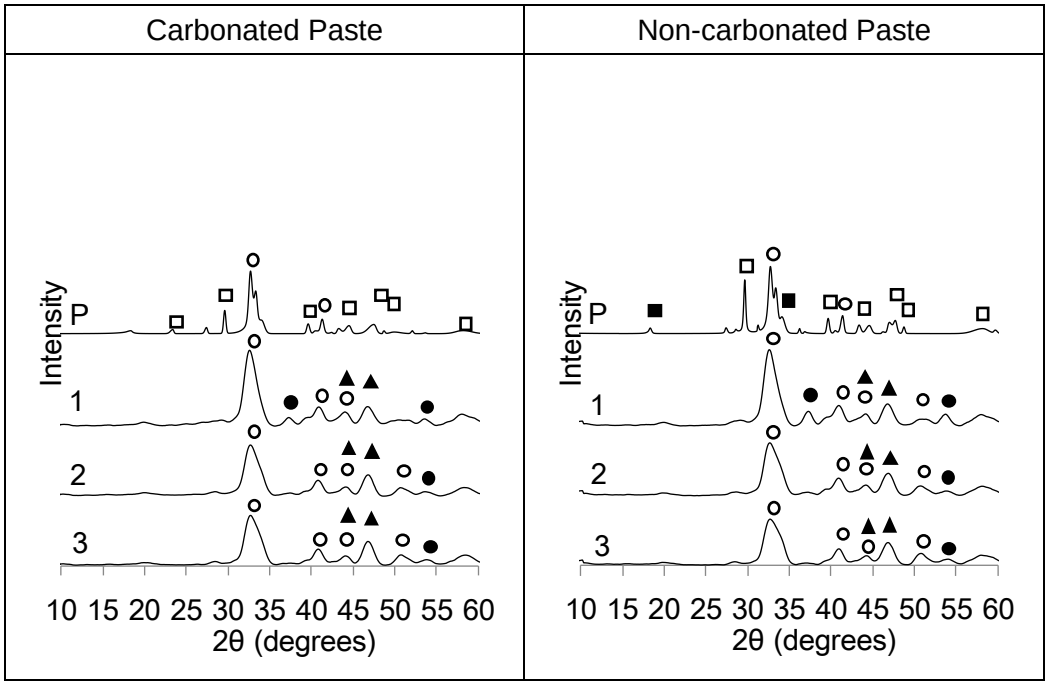


Figure 3-35 XRD profile: 800℃ (alite:▲, belite:○, portlandite:■ , calcite:□ , vaterite:♦ , lime:●)

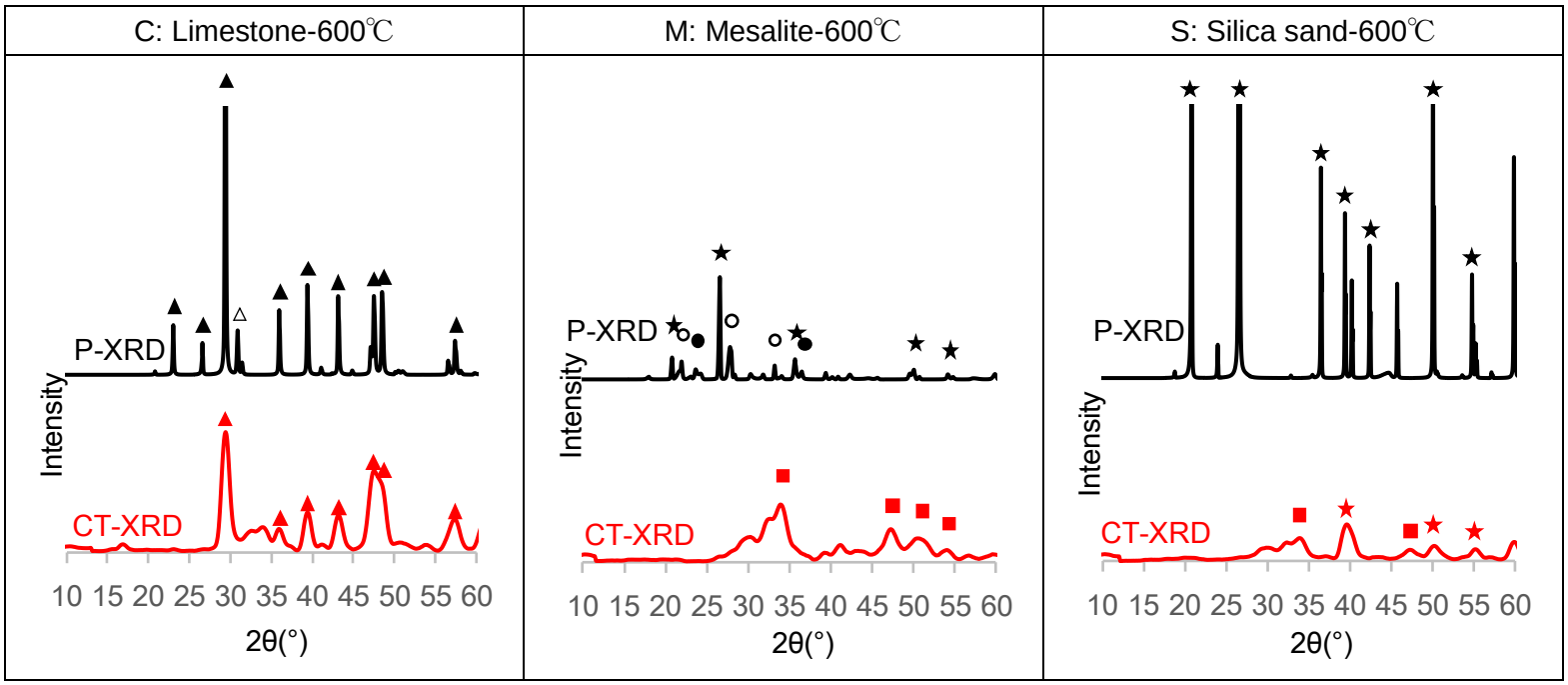


Figure 3-36 XRD profile: each aggregate type (calcite:▲, dolomite:△ quartz:★, zeolite:○, illite:●, portlandite:■)

(11) Limestone-600 °C

The peaks of Calcite can be found in both profiles. However, small peak of Dolomite shown in the profile of P-XRD cannot be found in that of CT-XRD.

(12) Mesalite-600 °C

As explained in Figure 3-9, the profile of P-XRD shows that some peaks of Quartz, Illite, and Zeolite are detected. In the profile of CT-XRD, however, these peaks cannot be detected. Moreover, the peaks of Portlandite are distinct. This may be considered that fresh cement paste dissolved into the void of aggregate during mixing followed by hardening. The reason why the aggregate-derived peak cannot be found is discussed in 3.4.3.

(13) Silica sand-600 °C

While some peaks of Portlandite are detected in the profile of CT-XRD, the peaks of Portlandite are consistent in both profiles. The reason why the peaks of Portlandite are detected in the CT-XRD's is that some areas of cement paste are included in Gauge Volume.

3.4.3 Discussion

Crystal phases identified by both P-XRD and the CT-XRD for each point are listed in Table 3-2. With regard to Portlandite, no peaks can be seen in Point1. Thus, carbonation occurred at the surface layer in contact with CO_2. Its decomposition observed at higher than 600°C. The peaks can be detected in Point 2 and Point 3 of NP-6 whereas no peaks are shown in P-XRD.

According to Calcite, the peaks can be detected in P-XRD or Point 1 for NP-series except NP-8, which derives from much contact with air-induced CO_2. CP-non heat was carbonated up to Point 2. CP-2, CP-4, and CP-6 were carbonated up to Point 3. Ref. [12] indicated that carbonation depth is proportional to elevated temperature, which supports the results in this research. Alite and Belite was detected mostly in NP-8 and CP-8, derived from the decomposition of C-S-H.

Comparison with P-XRD and the CT-XRD in CP-non heat indicates that there is a limitation for the CT-XRD to observe peaks in the range of less than 25° or less. This may derive from absorption of X-ray in low energy range. Moreover, the peaks of the CT-XRD is broader than those of P-XRD, thus closer peaks cannot be shown separately, represented as the range of 45°and 50°. However, the peak positions can be correctly shown in the profiles of the CT-XRD. Therefore, the CT-XRD can evaluate the effect of alteration (carbonation in this case) in non-destructive manner.

Figure 3-37 shows that the comparison of P-XRD of each aggregate type. This indicates that the maximum peak positions at around 29.5° for C, and 26.5° for M and S, and the absolute intensity of M is much lower than that of C and S. This means the crystalline of M is very low and thus, the peaks of quartz cannot be detected in CT-XRD. Instead of that, the peaks of

Table 3-2 The crystal phase for each sample identified by both P-XRD and the CT-XRD

Non-carbonated Paste					Carbonated Paste					Sample	
800	600	400	200	NH	800	600	400	200	NH		
×	×	○	○	○	×	×	○	○	○	P	Portlandite
×	×	×	×	×	×	×	×	×	×	1	
×	○	○	○	○	×	×	○	○	○	2	
×	○	○	○	○	×	×	○	○	○	3	
○	○	○	○	○	○	○	○	○	○	P	Calcite
×	○	○	○	○	×	○	○	○	○	1	
×	×	×	×	×	×	○	○	○	○	2	
×	×	×	×	×	×	○	○	○	×	3	
×	×	○	○	○	×	×	○	○	○	P	Vaterite
×	×	○	△	○	×	×	×	○	×	1	
×	×	×	×	×	×	×	×	×	×	2	
×	×	×	×	×	×	×	×	×	×	3	
○	×	×	×	×	○	×	×	×	×	P	Alite
○	×	×	×	×	○	×	×	×	×	1	
○	×	×	×	×	○	×	×	×	×	2	
○	×	×	×	×	○	×	×	×	×	3	
○	△	△	△	△	○	△	△	△	△	P	Belite
○	△	△	△	△	○	△	△	△	△	1	
○	×	×	×	×	○	△	×	×	×	2	
○	×	×	×	×	○	△	×	×	×	3	
○	△	△	△	△	○	△	△	△	△	P	Lime
○	△	△	△	△	○	△	△	△	△	1	
△	×	×	×	×	△	△	×	×	×	2	
△	×	×	×	×	△	△	×	×	×	3	

Portlandite can be detected in the area of aggregate.

Throughout the XRD results in these experiments, it can be concluded that the CT-XRD has a strong feature that can identify the crystals of internal structure properly, as symbolized in NP-6 or M series.

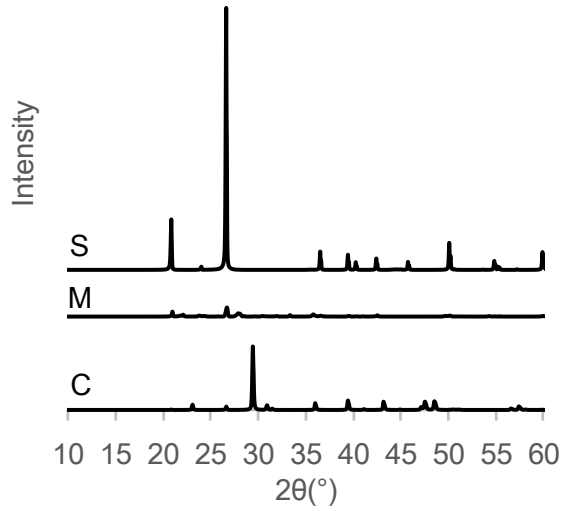


Figure 3-37 Comparison of P-XRD between each aggregate type

3.5 SUMMARY

In this chapter, focuses are mainly put on the phase segmentation of aggregate and crack propagation from X-ray images and verification of non-destructive integrated CT-XRD method by comparing with conventional powder X-ray diffraction technique. Firstly, phase segmentation was carried out and it can be said that this is properly complemented for each aggregate type. Moreover, this can be applicable to quantitative analysis especially for crack width. From the verification of CT-XRD, it clarified that regardless of limitation to detect the intensity peaks in the range of less than 25° and adjacent peaks separately, non-destructive integrated CT-XRD method can evaluate the peak positions and thus evaluate alteration of internal structure in non-destructive manner. Moreover, the profiles of cement paste heated at 600 °C indicated that the presence of Portlandite which might be in less crystalline form was observed. However, its formation was hardly observed in the profile of Powder XRD. Hence the Portlandite with less crystalline nature might be destroyed in the process of the grinding to prepare the powder. Moreover, it can be found out that identification of aggregate can be implemented from the CT-XRD properly to compare with XRD profiles of aggregate in powder state. Limestone crushed sand was identified as Calcite [CaCO3] and standard sand was as Quartz [SiO_2]. It also indicated that cement paste dissolved into the void of aggregate in the hardened mortar of mesalite,

REFERENCES

[1] Yamato, H., Hirono, S., Nakajima, T., and Torii, T. (1983). "Mineralogical feature and alkali-silica reactivity of limestone aggregate produced in Japan." *The Proceedings of Japan Concrete Institute*, 35(1), 967-972. (in Japanese)

[2] Noguchi, F., Ueda, Y., Kimura, H., and Yanagase, T. (1983). "Studies on the bloating mechanism of shales and prevention of fusion welding." *Journal of Ceramic Association Japan*, 91(1049), 27-34. (in Japanese)

[3] C.T. Chantler, K. Olsen, R.A. Dragoset, J. Chang, A.R. Kishore, S.A. Kotochigova, D.S. Zucker, X-ray Form Factor, Attenuation, and Scattering Tables (version 2.1.) [online], National Institute of Standards and Technology, Gaithersburg, MD, 2005. https://physics.nist.gov/PhysRefData/FFast/.

[4] Sheppard, A. P., Sok, R. M., and Averdunk, H. (2004). "Techniques for image enhancement and segmentation of tomographic images of porous materials." *Phisica A*, 339(1-2), 145-151.

[5] Doube, M., Klosowski, M. M., Argenda-Carreras, I., Cordelieres, F. P., Dougherty, R. P., Jackson, J. S., Schimid, B., Hutchinson, J. R., and Hsefelbine, S. J. (2010). "BoneJ: Free and extensible bone image analysis in ImageJ." *Bone*, 47, 1076-1079.

[6] Hilderbrand, T., and Ruegsegger, P. (1997). "A new method for the model-independent assessment of thickness in three-dimensional images." *Journal of Microscopy*, 185, 67-75.

[7] Tokuda, H. (1984). "Thermal properties of concrete." *Concrete Journal*, 22(3), 29-37. (in Japanese)

[8] Khoury, G. A. (1992). "Compressive strength of concrete at high temperatures: reassessment." *Magazine of Concrete Research*, 44(161), 291-309.

[9] Architectural Institute of Japan (2017). "Guide book for fire-resistive performance of structural materials." Maruzen publishing. (in Japanese)

[10] Groves, G. W., Rodway, D. I., and Richardson, I. G. (1990). "The carbonation of hardened cement pastes." *Advances in Cement Research*, 3(11), 117-125.

[11] Galan, I., Glasser, F. P., Baza, D., and Andrade, C. (2015). "Assessment of the protective effect of carbonation on portlandite crystals." *Cement and Concrete Research*, 74, 68-77.

[12] Kurata, K., Miyamoto, S., Minagawa, H., and Hisada, M. (2016). "Relationship between water-cement ratio and change of amount of portlandite due to carbonation in concrete exposed at various region of Japan during 10 years." *Cement Science and Concrete Technology*, 70(1), 435-442. (in Japanese)

[13] Li, Z., and Li, Q. (2011). "Experimental investigation on property recovery of concrete exposed to high temperature." Journal of Structural and Construction Engineering, 76(666), 1375-1382. (in Japanese)

[14] Rao, M. S. (1973). "Kinetics and mechanism of the transformation of Vaterite to Calcite." Bulletin of the Chemical Society of Japan, 46(5), 1414-1417.

[15] Castellote, M., Alonso, C., Andrade, C., Turrillas, X., and Campo, J. (2004). "Composition and microstructural changes of cement pastes upon heating, as studied by neutron diffraction." *Cement and Concrete Research*, 34(9), 1633-1644.

[16] Scrivener, K., Snellings, R., and Lothenbach, B. (2016). "A practical guide to microstructural analysis of cementitious materials." Boca Raton, CRC Press.

CHAPTER 4 EVALUATION OF MICROSCOPIC ALTERATION BY WATER ATTACK

4.1 INTRODUCTION

In this chapter, experimental work of water flow test using crack induced mortar was carried out to investigate the alteration in on the interface between the cement matrix and aggregate. At first, experimental outline was introduced which consists of sample preparation, test procedure, and setup conditions of the CT-XRD. Next, the results were explained and discussed from both CT and XRD measurement. Then, findings from this study was summarized in the last section.

4.2 EXPERIMENTAL OUTLINE

Experimental flowchart of this study is shown in Figure 4-1. After making the sample and initial measurement of the CT-XRD, carbonation test was carried out for 24 days. Then, 2nd measurement of the CT-XRD was carried out to investigate the effect of carbonation. Next, water flow test for 4 days was done followed by the 3rd CT-XRD measurement. Finally, carbonation test for 6 days and 3.5 months water flow test to the sample were carried out and then left in air for about 1 month. 4th measurement of the CT-XRD was done and obtained results were analyzed in this study.

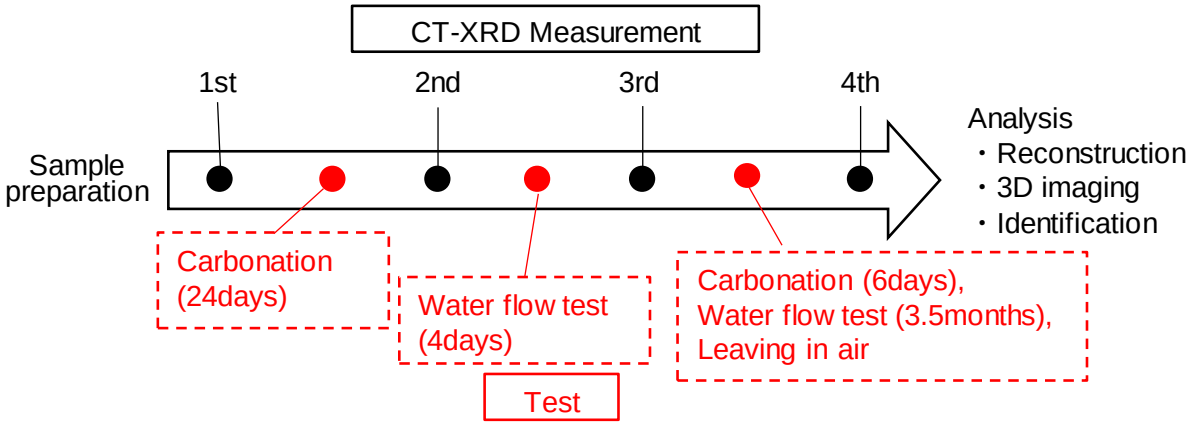


Figure 4-1 Flowchart of this experiment

4.2.1 Sample preparation

Mortar sample was used for this research. Ordinary Portland cement was used with a water to cement ratio of 0.5. A steel mold with 40 mm × 40 mm × 160 mm in size was used. After removal of the mold within 24 h and curing, it was cut so as to obtain a columnar sample about 5 mm in diameter and 5 mm in the length. Aluminum tape was used to cover the cylinder and to attach plastic tubes at both ends. Next, a crack to the vertical direction was induced by split test. After that, the tests shown in the next section were carried out on the sample.

4.2.2 Test procedure

(1) Carbonation test

As shown in Figure 4-2, carbonation test was carried out. Carbon dioxide gas was inhalled through a syringe and injected to the sample. The injecting rate was a constant 180 mL/day and the period of test was 24 days between 1st and 2nd measurements of the CT-XRD and 6 days between 3rd and 4th measurements of the CT-XRD.

(2) Water flow test

As shown in Figure 4-3, water flow test was carried out. A tubing pump with a microtube of 2 mm in the inner diameter was used. Purified water was used, flowing into the sample at the 30 mL/h rate. Between 2nd and 3rd measurement, the discharged water was collected to measure the calcium ion concentration. It is confirmed that the concentration of calcium ions increased in a few days and then leveled off. Between the 3rd and 4th measurement, the water was circulated using a tank of 30 L in volume through the tubing pump.

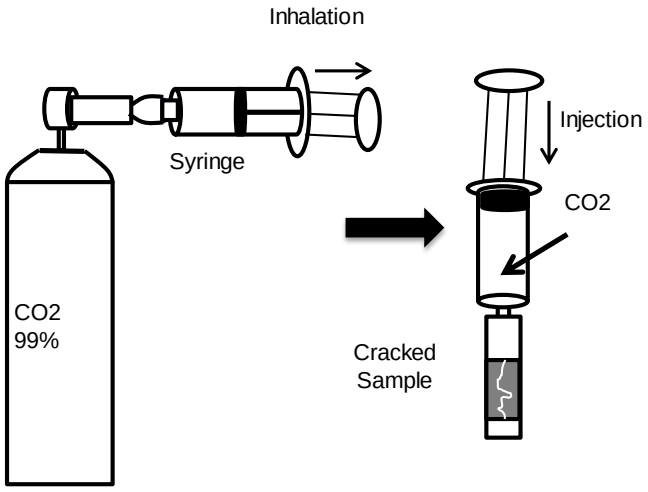


Figure 4-2 Schematic diagram of carbonation test

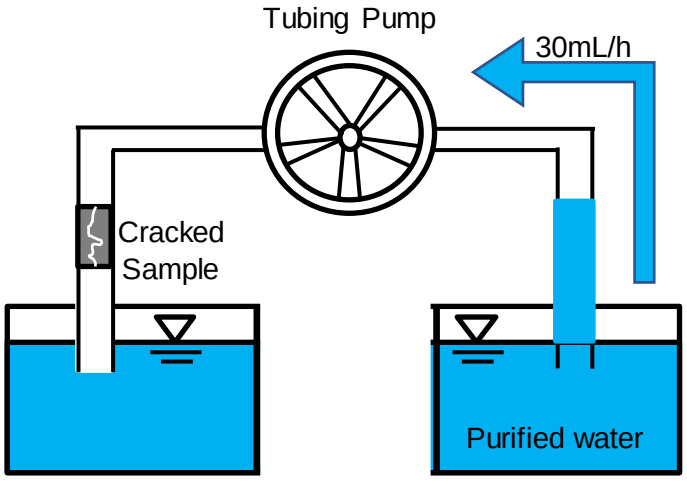


Figure 4-3 Schematic diagram of water flow test

4.2.3 Setup conditions

Table 4-1 shows the setup conditions in this experiment. Although exposure time or pixel sizes for each measurement are slightly different, almost all conditions are the same. The extracted X-ray energy for CT measurement is 25 keV and scanning angle steps is 0.12°, consistently. Image resolution is 7.14 μm/pixel and 5.08 μm/slice. The conditions for XRD measurement are the same for every measurement. As explained in next section, 4th XRD measurement was not carried out because the target point so far was disappeared judge from the cross section image.

4.3 RESULTS OF CT MEASUREMENT

4.3.1 Cross section image

Figure 4-4 shows the sectional images in the middle height of mortar sample for each measurement. The CT images show that there exists one unique aggregate shown in white in the upper right part. Point 1 for XRD measurement was set on this aggregate. To compare with it, Point 2 was selected on an aggregate near crack area. Other points were selected near crack area to investigate the alteration of cement paste before and after process; Point 3 and Point 4 are on the cement paste in the order to be closer. Compared with before and after carbonation test, it can be seen that crack width didn't become larger. On the contrary, water flow test for only 4 days influenced on crack width. Moreover, the area of cement paste around aggregate disappeared after 3.5 months' water flow test. Therefore, XRD measurements on Point 3 and 4 couldn't be carried out at 4th measurement.

Table 4-1 Details information of the CT-XRD used in this chapter

	Items		Experiment conducted in this chapter			
			1st	2nd	3rd	4th
CT	Instrument arrangement#		Previous			
	Extracted X-ray energy (keV)		25			
	Angle step (deg.)		0.12			
	Rotation (deg.)		180			
	Number of projections		1500			
	Exposure time (s)		0.4			
	Image reconstruction algorithm		Back Projection Procedure			
	Total number of cross-sectional image		768			
	Cross-section image size (Number of pixel)		767×767	766×766	768×768	
	Pixel size	Cross section (μm)	7.14			
		Slice thickness(μm)	5.08			
	Distance*	A to B (mm)	500			500
		B to C (mm)	400			350
XRD	Slit size	S1 (Width × Height)	0.05 mm×0.15 mm			
		S2 (Width × Height)	0.025 mm×3.00 mm			
		S3 (Width × Height)	0.15 mm×10.00 mm			
	Distance	S1 to sample (mm)	270			300
		sample to S2 (mm)	150			180
		S2 to S3 (mm)	460			430
	Diffraction angle (θ)		5°			
	Preset time (s)		300			

* Previous A=Sample, B=Mono-crystal, C=Camera

\# See Figure 2-3

4.3.2 Evaluation of damage

To evaluate the damage of actions, the area of crack was extracted in given all cross sections and 3D images of the extracted crack were made. To extract only the crack and calculate the volumatic space, SLICE was used. Extracting the specific area depends on grayscale intensity (GSV) and cracks, voids and other empty spaces exhibit similar GSVs. Then empty spaces between aluminum tape and sample, which connected with crack, were extracted. However, only the crack was extracted as the

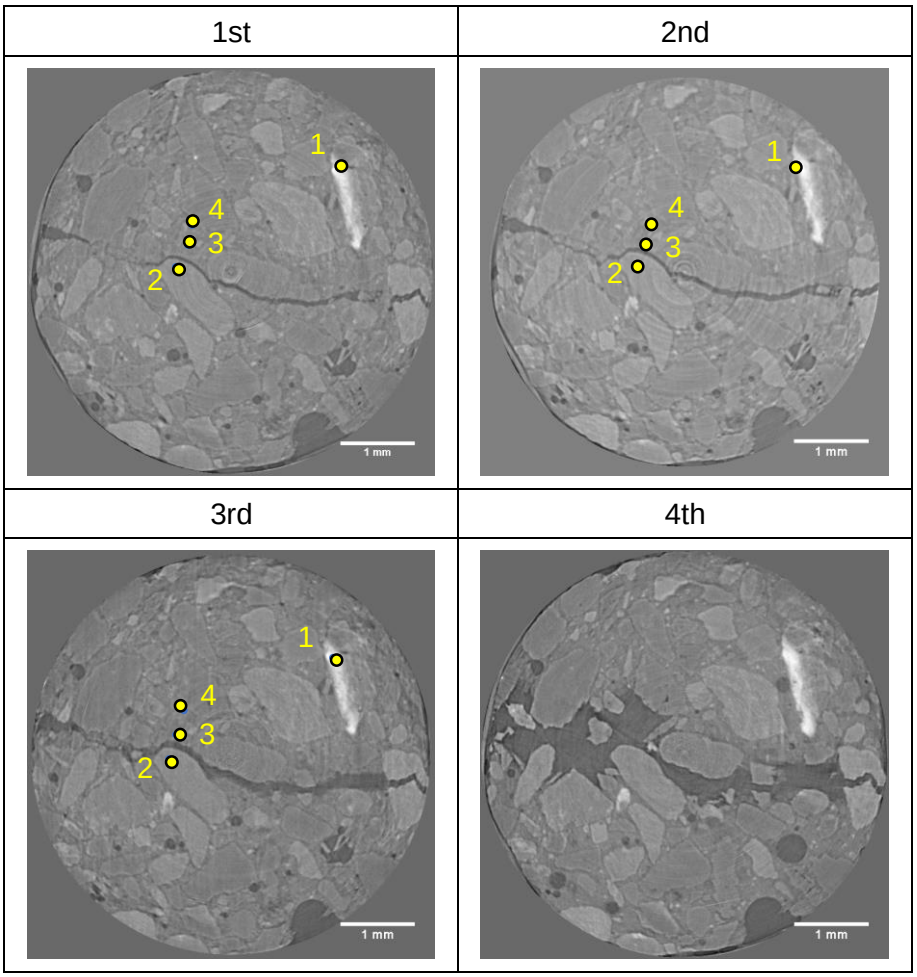


Figure 4-4 Cross section image for each measurement

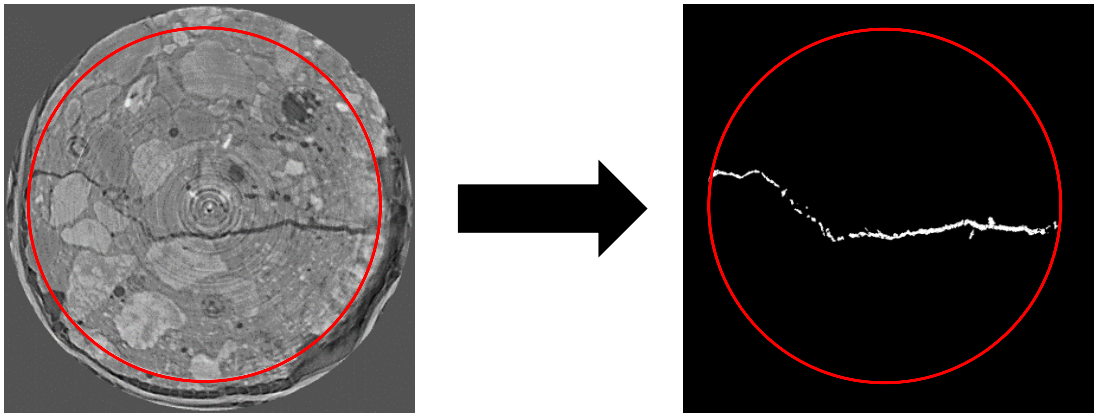


Figure 4-5 Example of extracting crack in a given sectional image at initial condition

CT image by specifying the region of interest (ROI) as shown in Figure 4-5. ROI was selected as 680 pixels in diameter in this case. The 3D images for each measurement from the extracted crack

Table 4-2 Volume of extracted crack

Measurement times	Volume
1st	1.07 mm^3
2nd	1.46 mm^3
3rd	2.22 mm^3
4th	9.09 mm^3

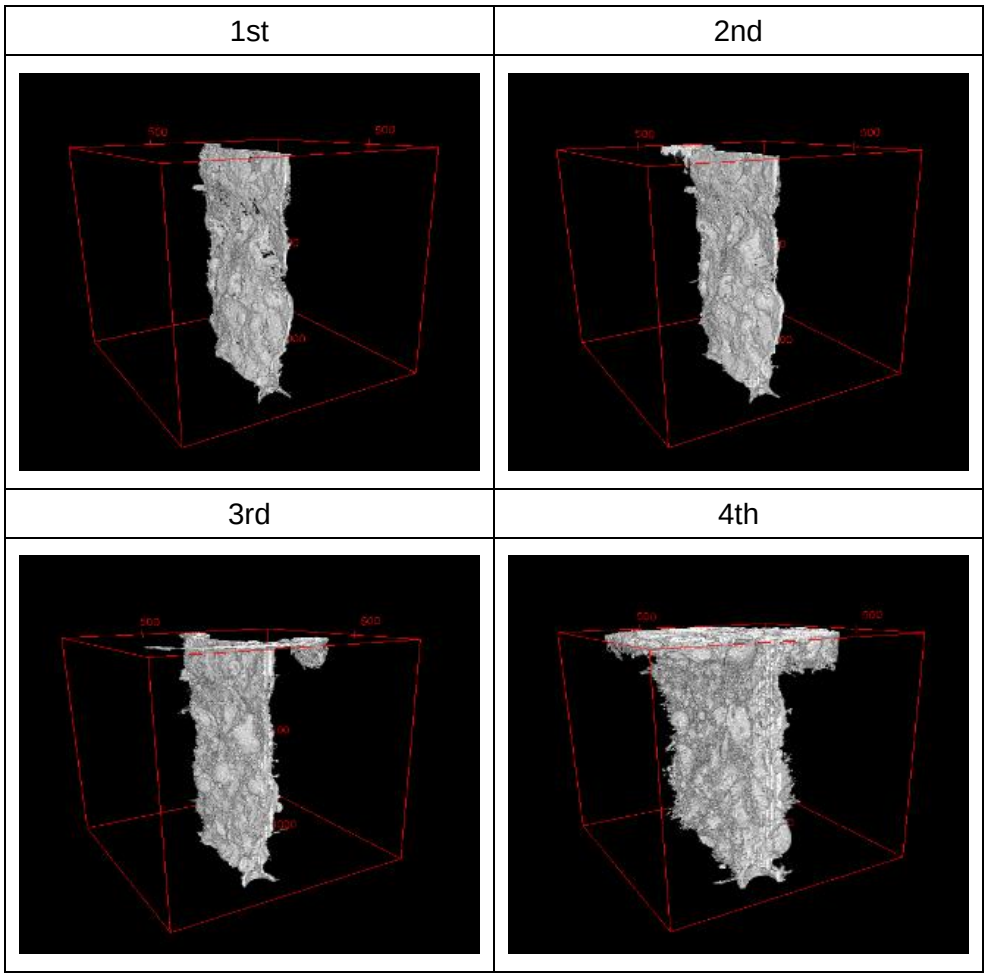


Figure 4-6 3D images of extracted crack for each measurement

are shown in Figure 4-6. It is clearly shown that crack area of 4th measurement was enlarged compared with that of 1st measurement. This was due to contacting with water at the top surface followed by deterioration of the cement paste. Table 4-2 shows a result of the volume of crack. From the result, the volumatic space after 3.5 months' water flow test became 8.5 times larger than the initial state.

4.4 RESULTS OF XRD MEASUREMENT

Figure 4-7 ~ 4-10 show diffraction profiles for each measurement at Point 1 ~ Point 4, respectively. For identification, the diffraction angles of various crystals are also provided.

4.4.1 Point 1

The peaks of diffraction profiles for each measurement are almost all the same as Hematite. One of components of the sand in Shizunai-river used in this research is chert, and warm-colored chert originated from iron oxide [1]. This implies that the existence of Hematite is confirmed.

4.4.2 Point 2

As for Point 2, the diffraction spectrums have some matches with ICSD's Quartz and Chlorite. Chert mainly consists of Quartz, and Green-colored chert originated from green clay minerals including Chlorite. This implies that the existence of Chlorite is confirmed. In addition, the positions of peaks are different in the range from 70° to 75° between the measurements. This result was caused by the displacement of ROI.

4.4.3 Point 3

The peaks of Portlandite can be seen in the diffraction spectrum for 1st and 2nd measurement. However, the peaks are hardly manifested for 3rd measurement, which means that calcium

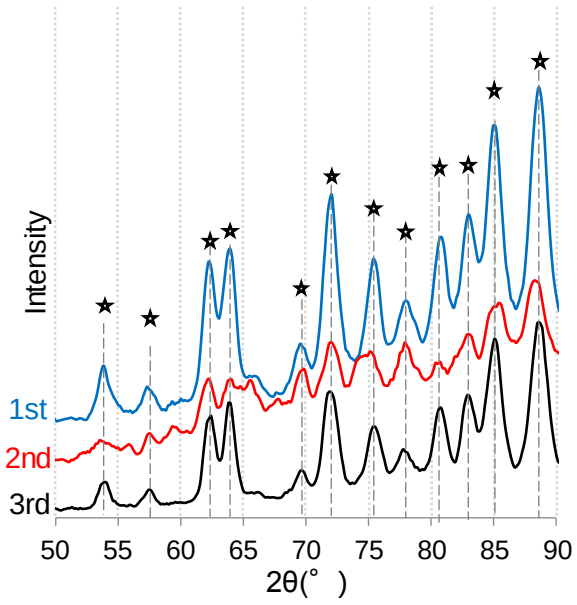


Figure 4-7 XRD profile: Point 1 (☆: Hematite)

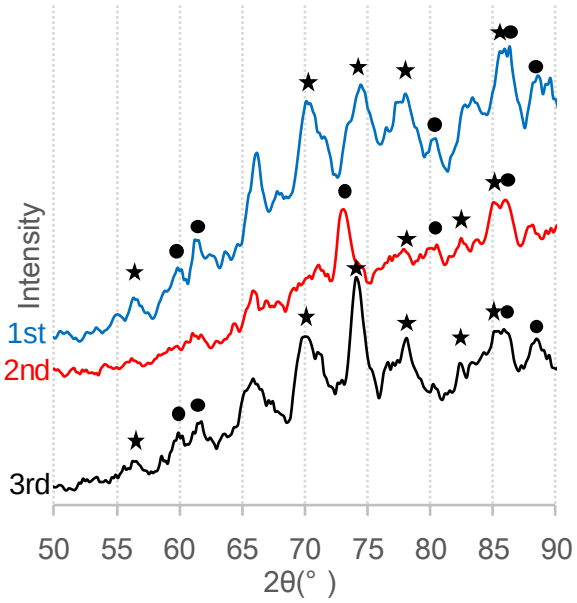


Figure 4-8 XRD profile: Point 2 (★: Quartz, ● Chlorite)

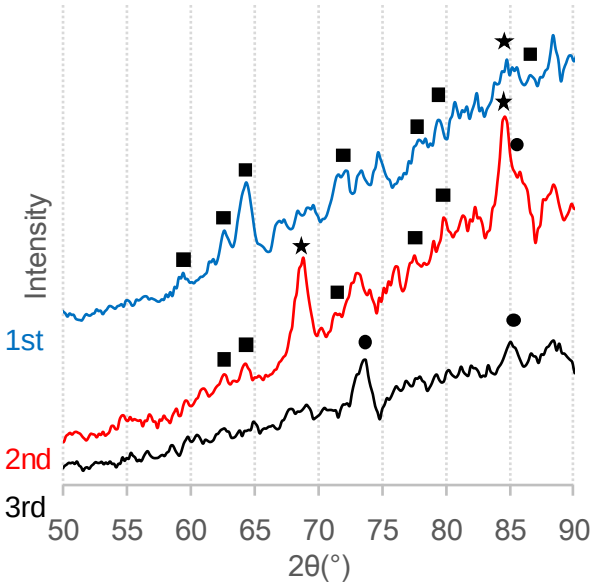


Figure 4-9 XRD profile: Point 3 (★: Quartz, ● Chlorite, ■: Portlandite)

hydroxide in the cement paste dissolved into flowing water only after 4 days water flow test. The peaks derived from Quartz and Chlorite can be seen, which indicates that the minute aggregate around cement paste was unexpectedly included in the XRD measurement at Point 3. It also can be seen that the peak of Calcite is not distinctive in the profile of 2nd measurement. This demonstrates that the Calcite was not formed because CO_2 gas was pressurized to go through the crack space and hence was not accumulated in this carbonation test. In addition, it

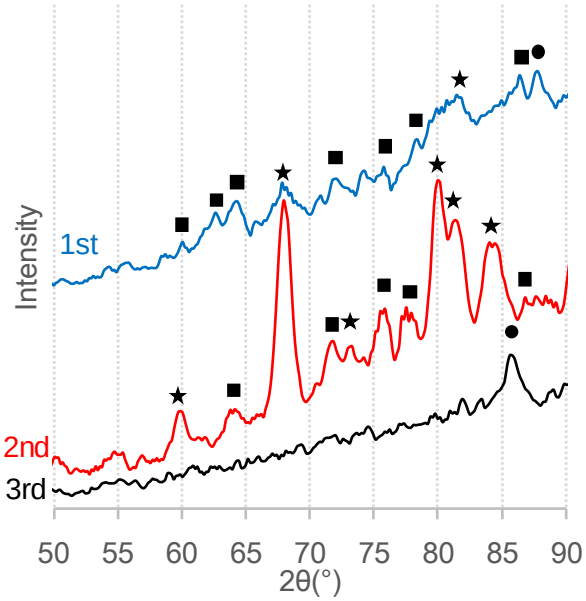


Figure 4-10 XRD profile: Point 4 (★: Quartz, ● Chlorite, ■: Portlandite)

can be considered that the moisture condition for carbonation was not sufficient [2].

4.4.4 Point 4

The same trend as Point 3 can be seen in the diffraction spectrum; the dissolution of calcium hydroxide occurred confirmed by the disappearance of peaks of Portlandite and some peaks of aggregate can be seen. Thereby, the leaching can be observed in the cement paste even further from the crack edge.

4.5 SUMMARY

In this study, alteration of deteriorated mortar due to the action of CO_2 gas exposure and water flow was investigated by using the non-destructive integrated CT-XRD method. It can be concluded that calcium hydroxide in the cement paste around aggregate near crack was dissolved after 4 days' water flow test. Moreover, the loss of the corresponding region of the leached cement paste was found after 3.5 months' water flow.

REFERENCES

[1] Sudo, S., Arita, M., and Fujihashi, Y. (2008). "Sand and Beach of Hokkaido (1): Sands from

Hidaka Mountains – from Hidaka Area to Tokachi Area." *Chishitsu News*, 651, 8-21. (in Japanese)
[2] Šavija, B., and Luković, M. (2016). "Carbonation of cement paste: Understanding, challenges, and opportunities." *Construction and Building Materials*, 117, 285-301.

CHAPTER 5 EVALUATION OF MICROSCOPIC ALTERATION SUBJECTED TO HIGH TEMPERATURE AND WATER

5.1 INTRODUCTION

In this chapter, the results and discussions are described based on three experimental works; first is to investigate the effect of heat duration time on alteration. From this experiment, crack behavior and alteration of cement hydrate system due to heat duration time are discussed. Second is to investigate the effect of immersion in pure water on fire-damaged cementitious material at various temperatures by using non-destructive integrated CT-XRD method. This study provides the knowledge of microscopic alteration behavior exposed to high temperature followed by subjected to water immersion. The obtained results contribute to new findings of alteration behavior under high temperature conditions from the microscopic view point. This study is analyzed and discussed from both image analysis to segment the degradation area and XRD analysis to study the alteration mechanism. Finally, investigation of the effect of environment after exposure of high temperature on the crack behavior and alteration from microscopic viewpoint was carried out. In this experimental work, prepared samples are measured three times; initial, after heating, and after putting in air or water. This study put a focus on the effect of difference of environment after heating, and then analyzed the quantitative analysis of crack ratio and alteration of cement hydration products. This is surely valuable data to reveal the mechanism of re-curing. In this experiment, re-curing was defined as curing after heating.

5.2 EXPERIMENTAL OUTLINE

An overview of the experimental program is shown in Figure 5-1 to meet the objectives. Experiment 1 is to clarify the effect of heating duration time on alteration mechanism. Experiment 2 is to investigate the effect of immersion in deionized water on fire-damaged cementitious material at various temperatures. Experiment 3 is to investigate the effect of environment of standing sample on the properties of cementitious materials after heating (in air or in water).

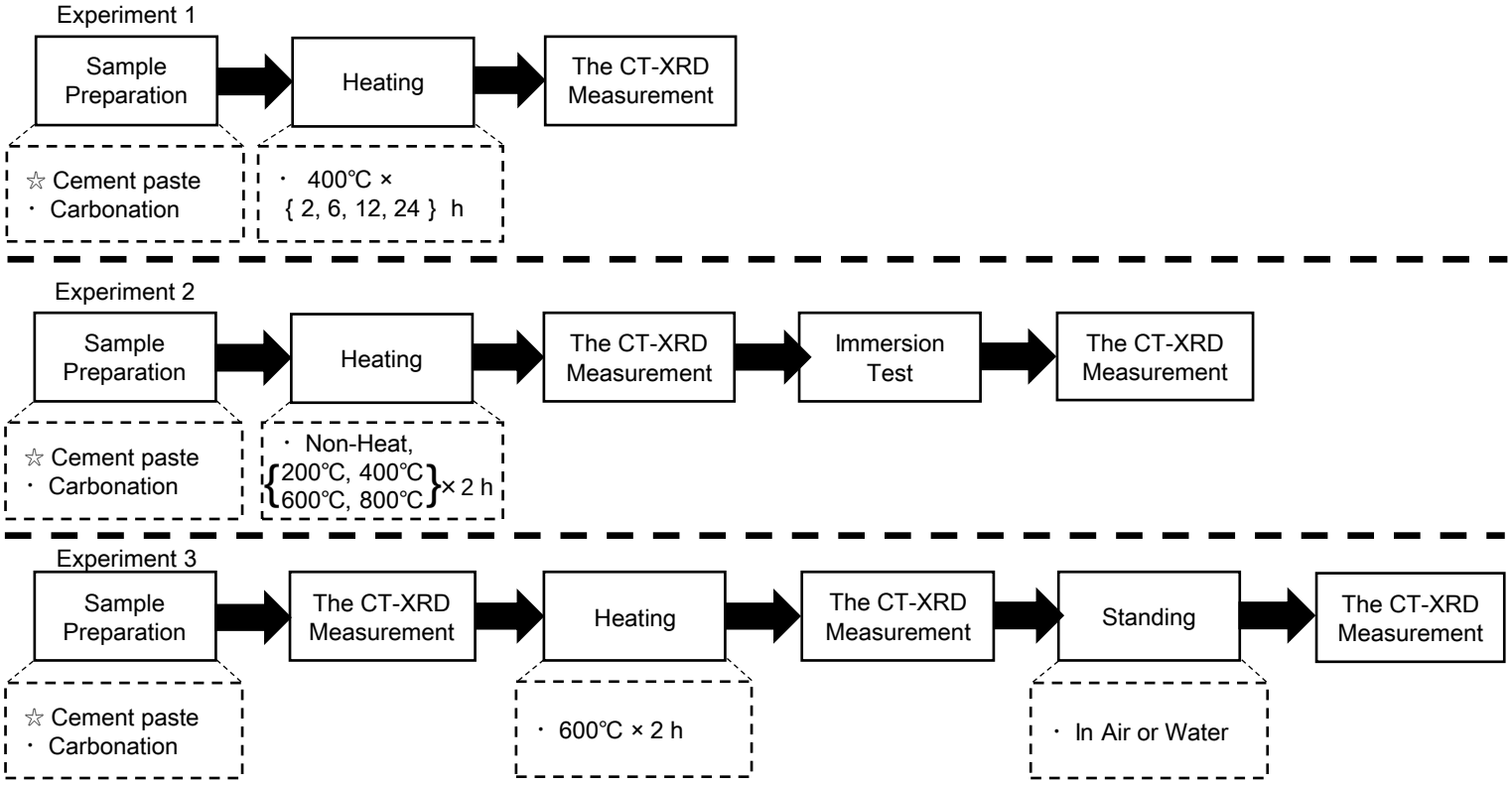


Figure 5-1 Overview of experimental program

5.2.1 Sample preparation

(1) Experiment 1

Cement paste with only the Ordinary Portland Cement was used in this experiment. A water to cement ratio is 0.6. The cement paste was mixed and molded into metal frame in the size of 40×40×160 mm. The samples were de-molded after 24 hours of molding, and then cured under water until cutting. After 28 days water curing and about 1 months leave in air, the hardened cement paste was cut into the prism in the size of 2.5×2.5×5 mm for the CT-XRD measurement followed by setting the samples on the jig using epoxy resin, denoted by sample A. After more 7 months leave in air, three more samples were prepared in the same way as above mentioned, denoted by sample B~D.

(2) Experiment 2

Cement paste with only the Ordinary Portland Cement was used in this experiment. A water to cement ratio is 0.6. The cement paste was mixed and molded into metal frame in the size of 40×40×160 mm. The samples were de-molded after 24 hours of molding, and then cured under water until cutting. After about 12 months of water-curing, the hardened cement pastes were cut into the prism in the size of 2.5×2.5×5 mm for the CT-XRD measurement. Carbonation test and

heating test described in 5.2.2 were carried out followed by setting the samples on the jig using epoxy resin.

(3) Experiment 3

Mortar was made in this Experiment 1. Ordinary Portland cement was used as binder and tap water with anti-bubble agent was used to reduce entrapped air. Limestone crushed sand was used as aggregate (Details are explained in 3.2.1.1). Before mixing, materials were calculated as a water to cement ratio of 0.5 and the aggregate volume of 0.05. Mixed materials were casted into metal frame in the size of 40×40×160 mm. The samples were de-molded after 24hours of molding, and then cured under water for 28 days. Then, the samples were cut into the prism in the size of 2.5×2.5×5 mm, and two samples were prepared; one is for air re-curing and the other is for water re-curing, denoted by A and W, respectively.

5.2.2 Test procedure

(1) Experiment 1

Heating test was carried out using electronic furnace with a temperature control program. The rate of heat increase was set at 10 °C per minute until the target maximum temperature was reached. The rate of heat decrease was also set at 10 °C per minute until room temperature. The target maximum temperature was 400 °C, with the duration time of 12 hours for sample A, and 2 hours, 6 hours, 24hours for sample B~D. Table 5-1 shows the introduction of samples in this experiment. As for sample B~D, the change of the weight and length was measured before and after heating. The weight was measured using electronic balance which is measureable in the increment of 0.1 mg. The length was measured using micrometer in the increment of 1 μm at the center height of each side.

(2) Experiment 2

Before the CT-XRD measurement in this Experiment, samples were carbonated doing the following procedure; samples were left in a container inside constant temperature furnace under

Table 5-1 Samples' introduction in this experiment

Sample	Curing	Heating duration time
A	28 days in water, 1 month in air	12 hours
B	28 days in water 8 month in air	2 hours
C		6 hours
D		24 hours

100 °C condition. 99% CO_2 gas was injected into container per 1 day and this process was continued for a period of 7 days.

After carbonation test, heating test was carried out using electronic furnace with a temperature control program. The rate of heat increase was set at 10 °C per minute until the target maximum temperature was reached. The maximum temperature was maintained for 2 hours and the rate of heat decrease was also set at 10 °C per minute until room temperature. The target maximum temperature was 200, 400, 600, and 800 °C, and Non-Heated (NH) sample was also prepared.

After the heating test and initial CT-XRD measurement, samples were immersed into deionized water. Immersion test was continued for a period of 28 days, with change of water every 7 days.

(3) Experiment 3

At first, initial measurement was carried out for both samples. Afterwards, heating test was carried out using electronic furnace with a temperature control program. The rate of heat increase was set at 10 °C per minute until the target maximum temperature was reached. The maximum temperature was set as 600 °C and maintained for 2 hours. Then, samples were removed from the furnace and soon after measured by the CT-XRD. After that, re-curing was carried out at ambient temperature for 1day. Finally, 3rd measurement was done.

5.2.3 Setup conditions

(1) Experiment 1

Setup conditions in this measurement are followings; the extracted energy of X-ray CT measurement was 25 keV. Angle steps during CT measurement were 0.12° with an exposure time of 0.4 s. Image resolution was 2.41 μm/voxel for sample A and 2.44 μm/voxel for sample B~D. The beam size was 0.05 mm in width and 0.3 mm in height. The angle of diffraction (θ) was fixed at 5° and the preset time was 300 s for XRD measurement. Table 5-2 shows the details of setup conditions for the CT-XRD measurement in this chapter.

(2) Experiment 2

Setup conditions in this measurement are followings; the extracted energy of X-ray CT measurement was 25 keV. Angle steps during CT measurement were 0.12° with an exposure time of 0.4 s. Image resolution was 2.44 μm/voxel. The beam size was 0.05 mm in width and 0.3 mm in height. The angle of diffraction (θ) was fixed at 5° and the preset time was 300 s for XRD measurement.

(3) Experiment 3

Setup conditions in this experiment was same as Experiment 1 except of image resolution.

Image resolution was 2.45μm/voxel, slightly different from Experiment 1.

The details of setup conditions ware shown in Table 5-2.

Table 5-2 Details information of the CT-XRD used in this chapter

	Items		Experiment conducted in this chapter			
			Ex 1		Ex 2	Ex 3
			1st	2nd	1st & 2nd	1st~3rd
CT	Instrument arrangement#		Previous	Current		
	Extracted X-ray energy (keV)		45	25		
	Angle step (deg.)		0.12			
	Rotation (deg.)		180			
	Number of projections		1500			
	Exposure time (s)		1.2	0.4		
	Image reconstruction algorithm		Back Projection Procedure			
	Total number of cross-sectional image		1440			
	Cross-section image size (Number of pixel)		1360 ×1360	1920×1920		
	Pixel size	Cross section (μm)	2.42	2.44		2.45
		Slice thickness(μm)	2.42	2.44		2.45
	Distance*	A to B (mm)	500	600		
		B to C (mm)	330	20	30	
XRD	Slit size	S1 (Width × Height)	0.05 mm×0.30 mm			
		S2 (Width × Height)	0.025 mm×3.00 mm			
		S3 (Width × Height)	0.15 mm×10.00 mm			
	Distance	S1 to sample (mm)	300	800		
		sample to S2 (mm)	150	170		
		S2 to S3 (mm)	460	440		
	Diffraction angle (θ)		5°			
	Preset time (s)		300			

* Previous A=Sample, B=Mono-crystal, C=Camera
Current A=Mono-Crystal, B=Sample, C=Camera

See Figure 2-3

5.3 EFFECT OF HEATING DURATION TIME

5.3.1 Cross section image

Figure 5-2 shows cross sectional images of each sample after heating test. The cross section is located in the middle height of sample and shown in 8-bit gray scale image. It can be seen that image quality between sample A and other's is different. This is derived from the difference of extracted X-ray CT energy. In the image of sample C and D, ring shaped something can be found out around sample, which aluminum jig is shown inside the image. With regards to crack propagation, little crack can be seen in sample B and small crack was found out in the outer edge of sample C. However, cracks become significant in sample A, after heating 12 hours. Moreover, the amount of cracks increased in sample D. This might be derived from the decomposition of cement hydrate. This is discussed in next sections.

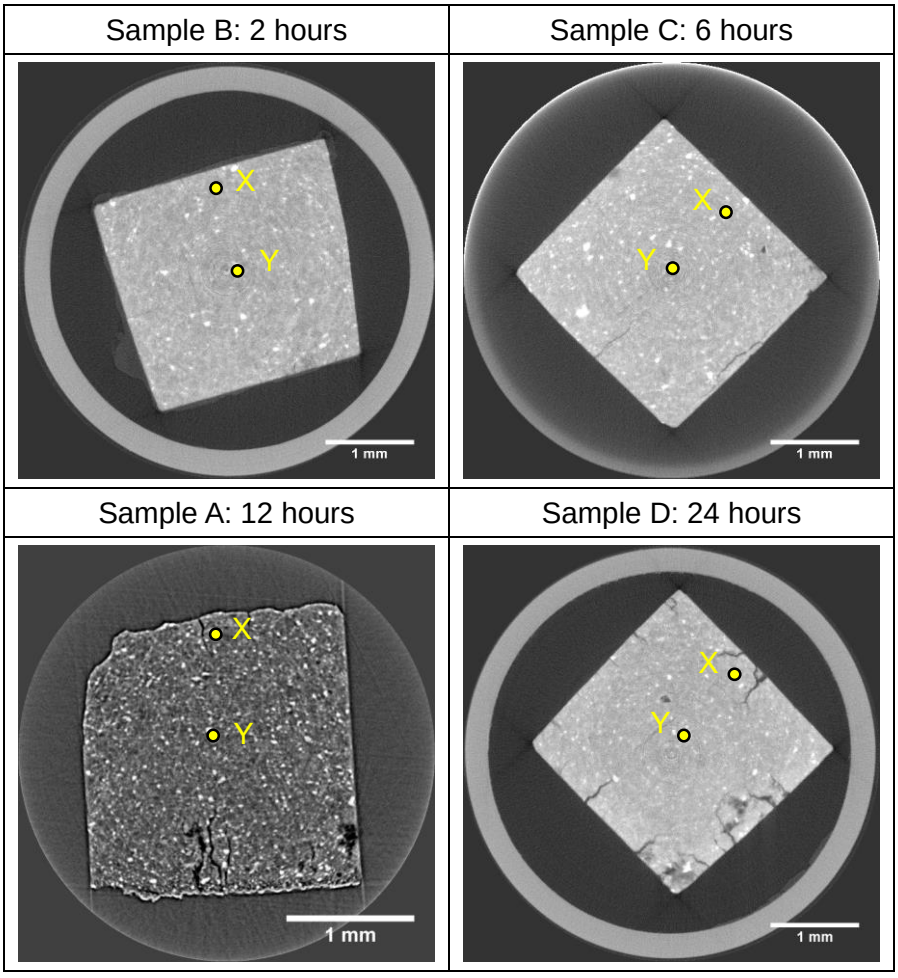


Figure 5-2 Cross sectional image in this experiment

5.3.2 Mass loss and shrinkage

Figure 5-3 and Figure 5-4 show the weight loss ratio and shrinkage by heating test, respectively. In this study, mass loss is calculated by the change of weight before and after heating and shrinkage is done by the change of average length of each 3 side. From Figure 5-3, mass loss was equally about 15% in the 2 hours and 6 hours heating sample, and increased by 20 % in 24 hours heating sample. Figure 5-4 clearly shows shrinkage had the same trend as mass loss ratio, which means the results of the 2 hours and 6 hours heating sample are almost all equal and 24 hours heating had a significant effect on increase of shrinkage. As discussed in the next section, decomposition of Portlandite evaporates the chemical bound water and then mass loss and shrinkage increased. This mechanism might affect the crack propagation at the edge of sample.

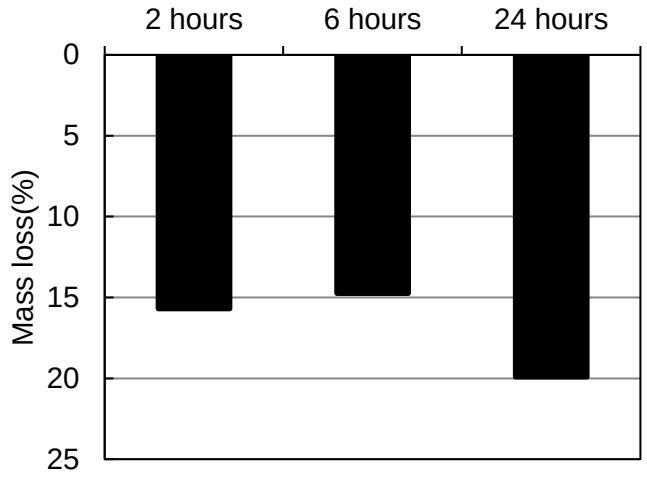


Figure 5-3 Results of mass loss

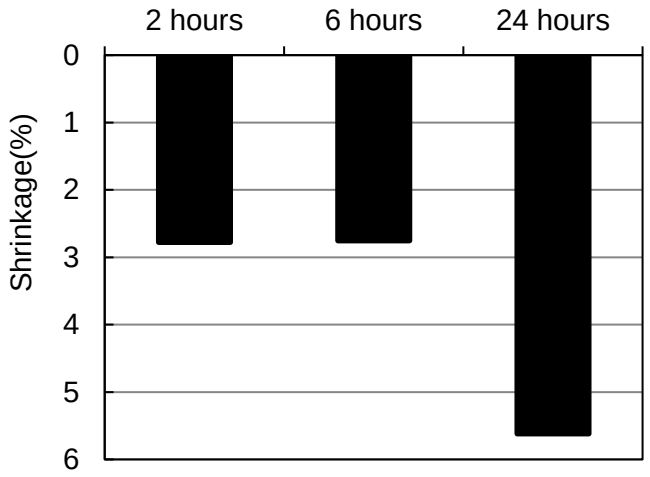


Figure 5-4 Results of shrinkage

5.3.3 Results of XRD measurement

Regions of interests were determined for XRD measurements as point X and Y on the edge and center, respectively (shown in Fig. 5-2 as circle). Figure 5-5 shows the XRD profiles of each sample for the Point X and Point Y. At first, it indicates that the width of peaks in sample B~D is broader than that in sample A. It might be affected by the difference of instrumental

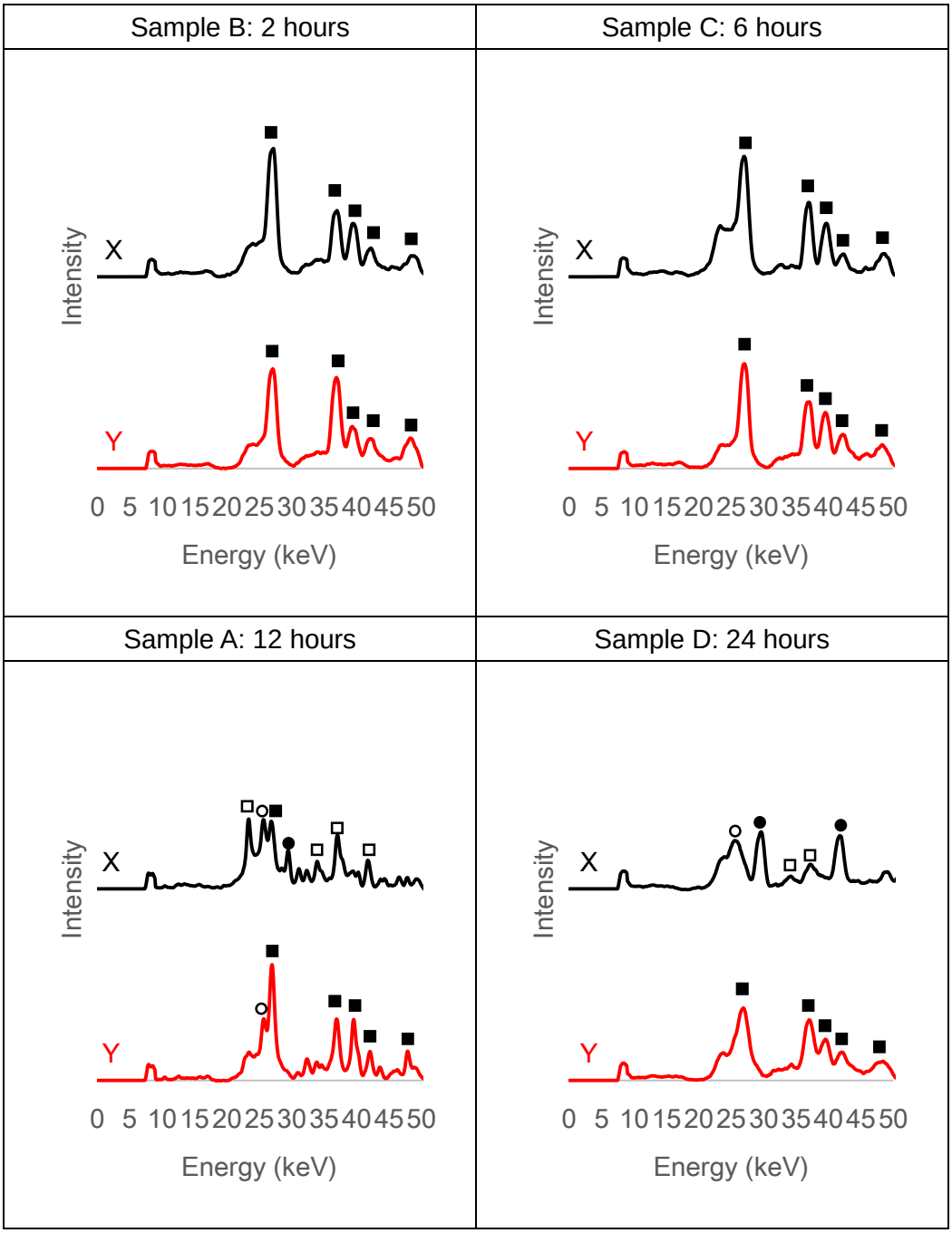


Figure 5-5 XRD profiles in this experiment (belite: ○, portlandite: ■, calcite: □, lime: ●)

arrangement. According to sample B and C, the peaks of portlandite can be seen at both point X and point Y. However, the profiles of sample A and sample D at point X has few portlandite peaks whereas the peaks of calcite and lime can be found. Ref [1] suggested that the decomposition of portlandite occurs if cement paste was heated for a long time at 300~400°C. Therefore, its decomposition occurred in these sample at the surface. The peaks of portlandite was found out in the profile of sample A and sample D at Point Y. But as discussed in section 3.4.2(8), portlandite with less crystalline was reformed due to the reaction of lime with water vapor inside the sample when cooling procedure.

As a summary from this experiment, it can be suggested that the decomposition of portlandite occurs in case of that duration time exceeds 12 hours at 400°C.

5.4 EFFECT OF TEMPERATURE BEFORE AND AFTER IMMERSION

5.4.1 Cross section image

Figure 5-4 ~ 5-8 shows cross sectional images of each sample before and after immersion test. The cross section is located in the middle height of sample. Each slice was processed a matrix size into 1500×1500 pixels. With regard to the images before immersion, cracks can be seen only in the C-8, which is same as the results of Chapter 3. It can confirm that the cracks generated due to decomposition of Calcite at higher than 600°C. However, the images after immersion indicate that the edge became porous in C-NH, C-2, and C-4. Moreover, the edge of C-6 sample becomes more porous than these three samples and that of C-8 sample becomes darker. It derived from calcium leaching due to immersion and maximum temperature before immersion affected the degree of leaching.

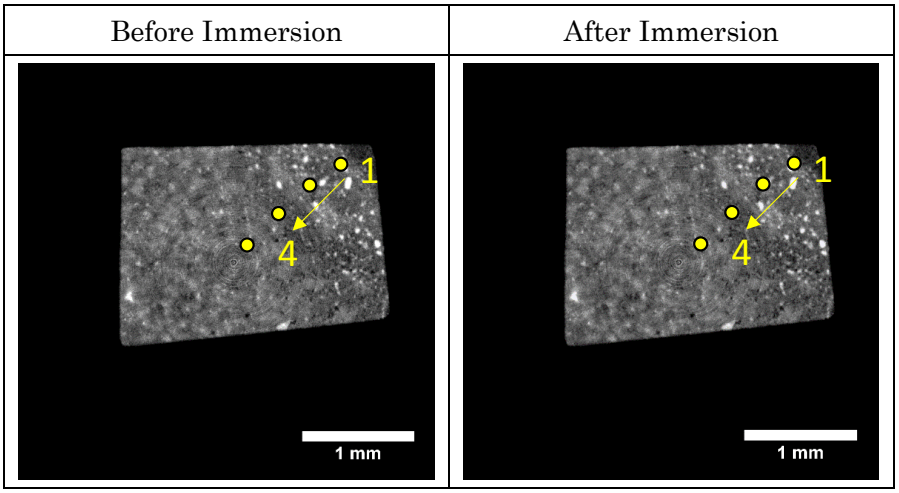


Figure 5-6 Cross sectional images at center heights of NH.

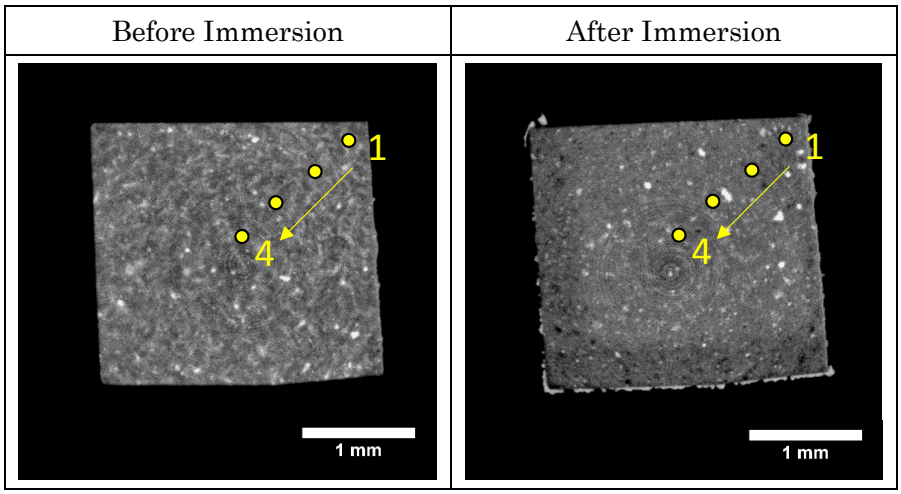


Figure 5-7 Cross sectional images at center heights of 200℃.

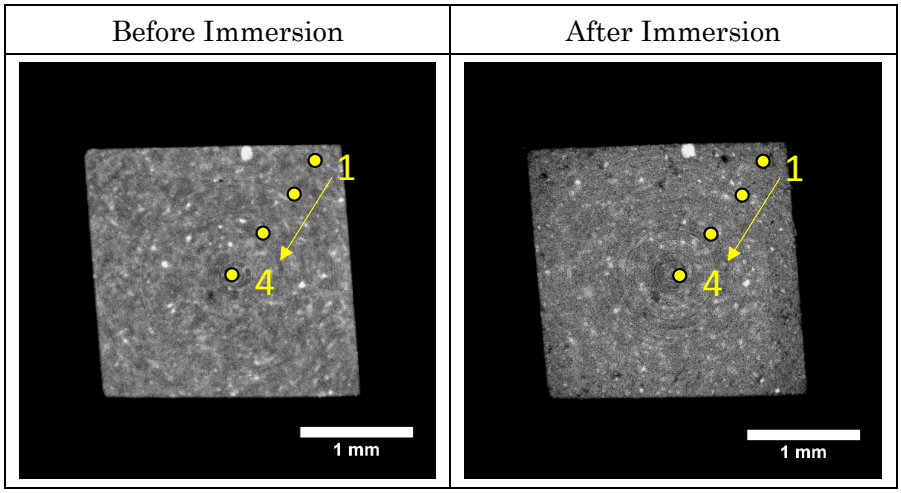


Figure 5-8 Cross sectional images at center heights of 400℃.

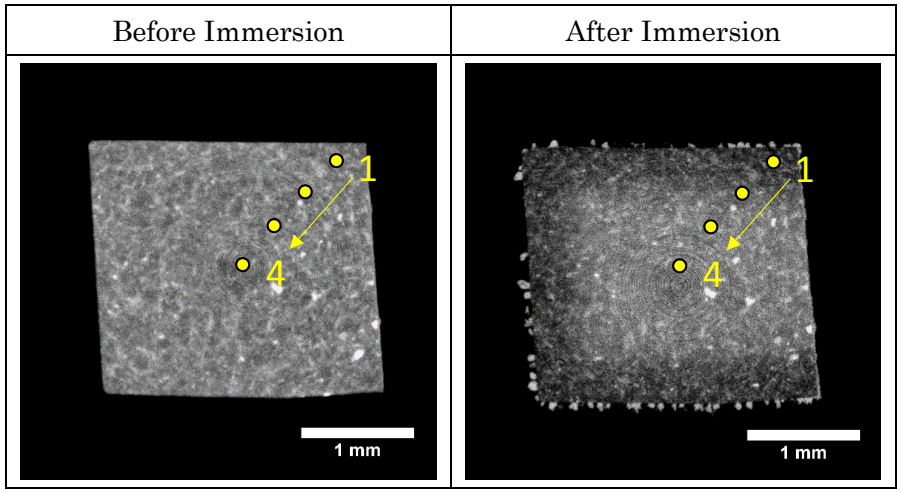


Figure 5-9 Cross sectional images at center heights of 600℃.

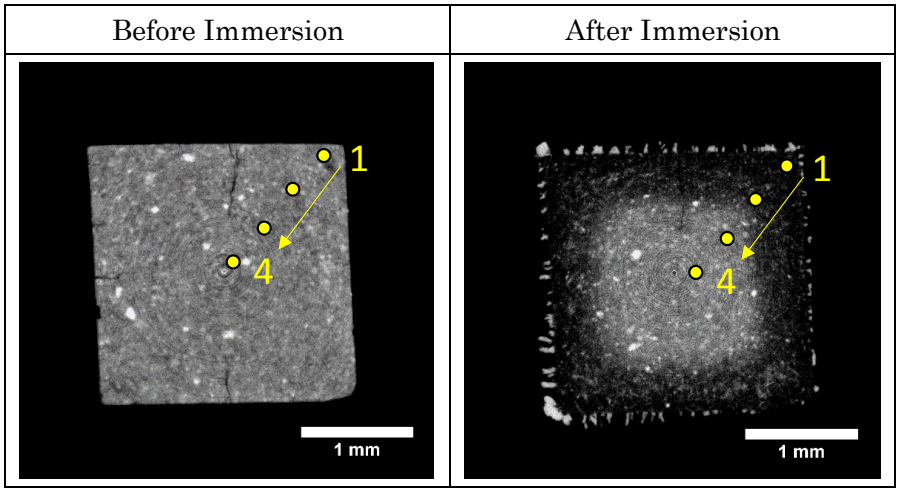


Figure 5-10 Cross sectional images at center heights of 800℃.

5.4.2 Image processing

In this study, all the CT images were consistently converted to 8bit gray scale images by setting the minimum and maximum to -2 and 8, respectively. Figure 5-9 shows the histograms of each sample in 8bit scale and the way to determine the thresholds. Compared with histograms before and after immersion, the peak of cement paste in C-NH, C-2, and C-4 shifted slightly to lower values than that of before immersion. Moreover, it can be said that the peak of cement paste in 600°C and 800°C was separated into two peaks. These shifts can be discussed as followings.

Saito et al. showed the conceptual diagram of calcium leaching evaluated by an electrochemical technique, as shown in Figure 5-10 [2]. It indicates that the states of cement matrix can be expressed as four phases; Only SiO_2 exists in phase 1; C-S-H with decreased C/S ratio remains in phase 2; C-S-H with normal C/S ratio exists in phase 3; both C-S-H and Portlandite (CH) remains in phase 4. According to this diagram, obtained CT images can be confirmed that; phase 1 is shown represented in the edge of C-8, phase 2 is shown represented in the edge of C-6, and both phase 3 and phase 4 are shown represented in the center of all samples. Phase 3 and phase 4 are not distinctive from the CT measurement because the peak of Portlandite was not shown in histogram. Each threshold was determined to select the point of intersection in C-6-A and C-8-A. Threshold of air and Phase 1 is 82, the intersection between the right end of air peak and GSV axis in C-6-A. That of Phase 1 and Phase 2 is 130, the intersection between profile of C-6-A and C-8-A, and that of Phase 2 and Phase 3 was determined 155, the intersection between the first peak and second peak in the profile of C-6-A. Total leaching area could be extracted from the CT images dependent on these thresholds, segmented air as black, phase 1 as red, phase 2 as green and phase 3 and 4 as white color.

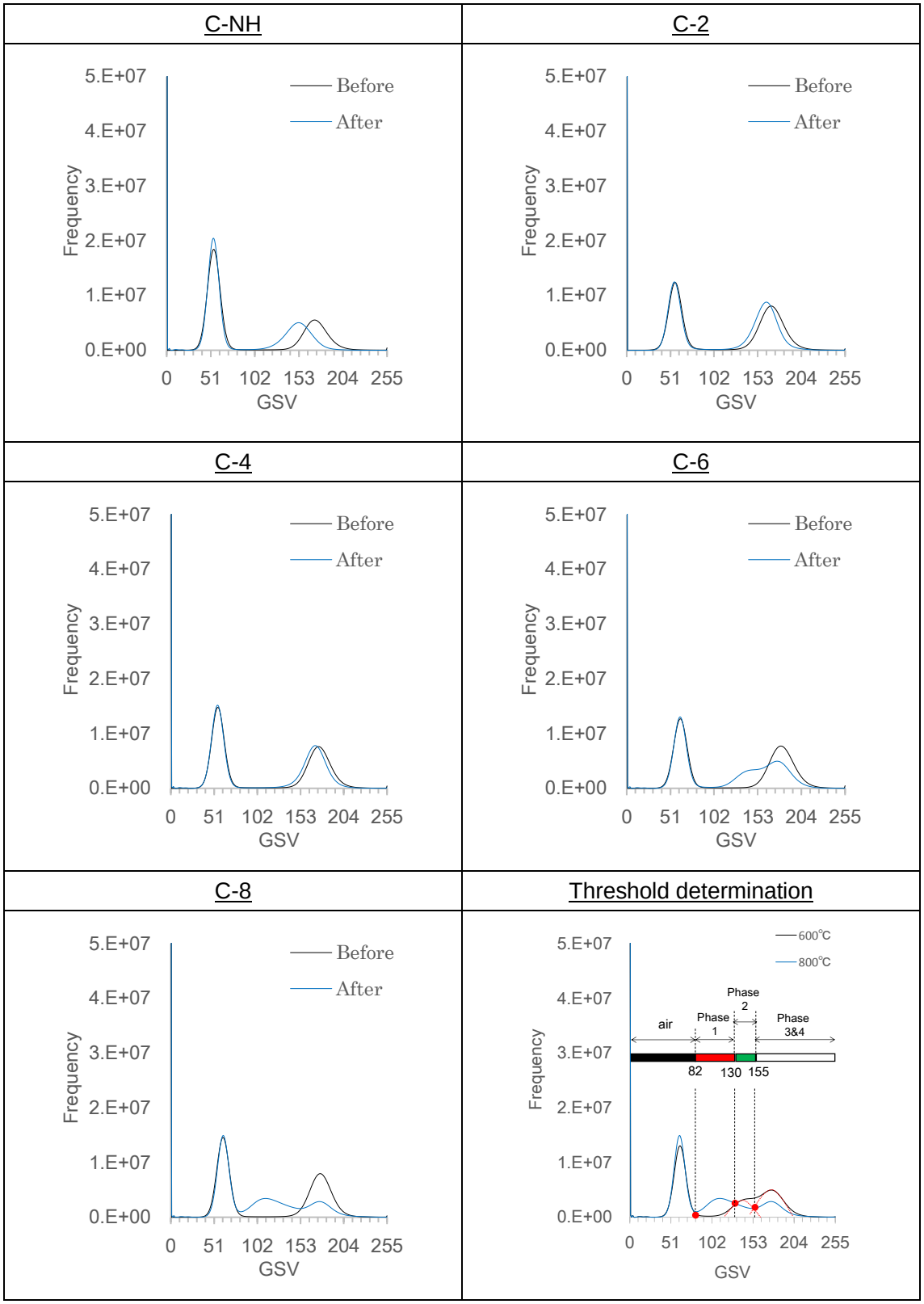


Figure 5-11 Histograms of each sample before and after immersion and threshold determination for phase segmentation

Cathode Side — Anode Side

Area Division	Phase 1	Phase 2	Phase 3	Phase 4
Phase Composition	SiO_2	C-S-H	C-S-H	C-S-H, CH
Ca/Si ratio in C-S-H		low	normal	normal

Figure 5-12 Schematic diagram of alteration mechanism with calcium leaching (revised Ref. [2])

5.4.3 Evaluation of leaching front

Figure 5-11 ~ 5-15 show the segmented images of each sample. First, it can be seen that leaching effect was observed equally from edge to center but blocked in some side of C-2 and C-6 sample. This might be derived from attaching epoxy on the side of samples accidentally when attaching themselves to jigs. From segmented images, leaching front was measured by taking average of arbitrary 4 points. Figure 5-16 shows the leaching front for each sample. According to this graph, C-4 exhibited no leaching front. This might be because of the fact that the clogging of the whole range of pores by the carbonation test [3]. After that, heating procedure produced so-called condition of internal autoclaving in cement paste [4]. This is particularly true for dense cement paste because low permeability resists moisture flow [5]. Therefore, additional hydration of unhydrated cement grains occurred effectively and thus increased the resistance of leaching in C-4 sample more than C-NH. A comparison of other

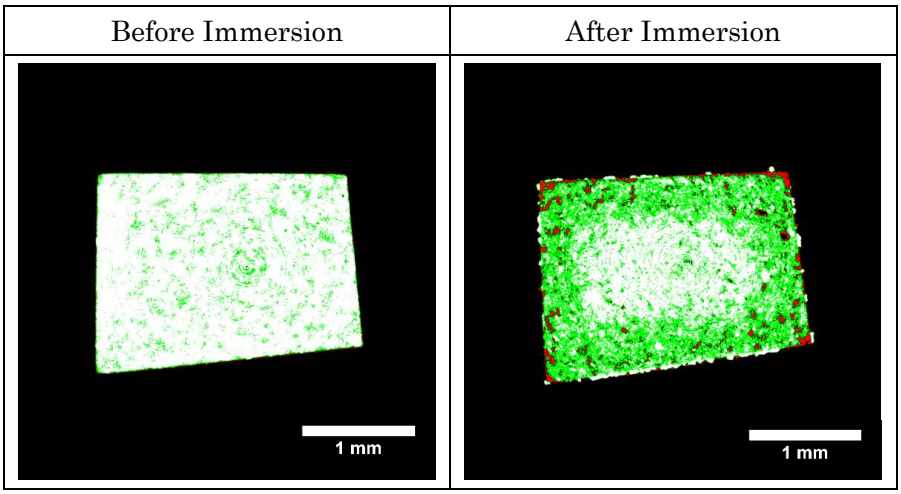


Figure 5-13 Visualization of leaching area: NH

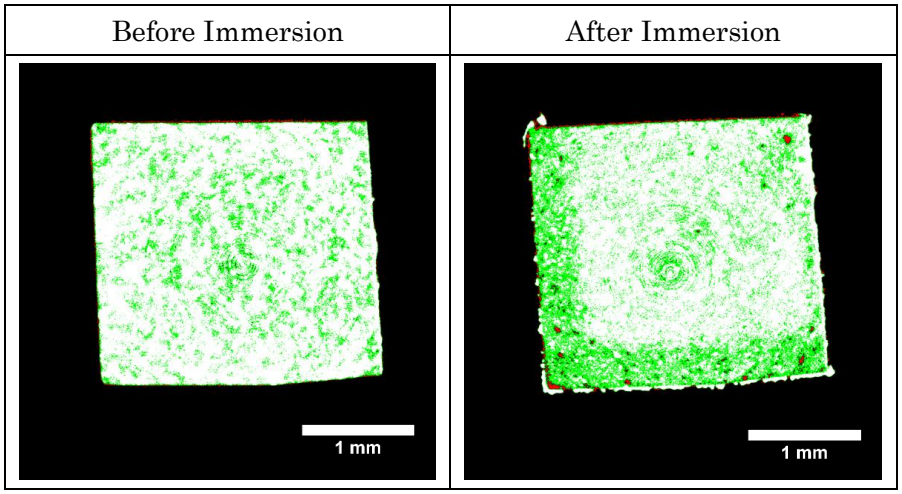


Figure 5-14 Visualization of leaching area: 200℃

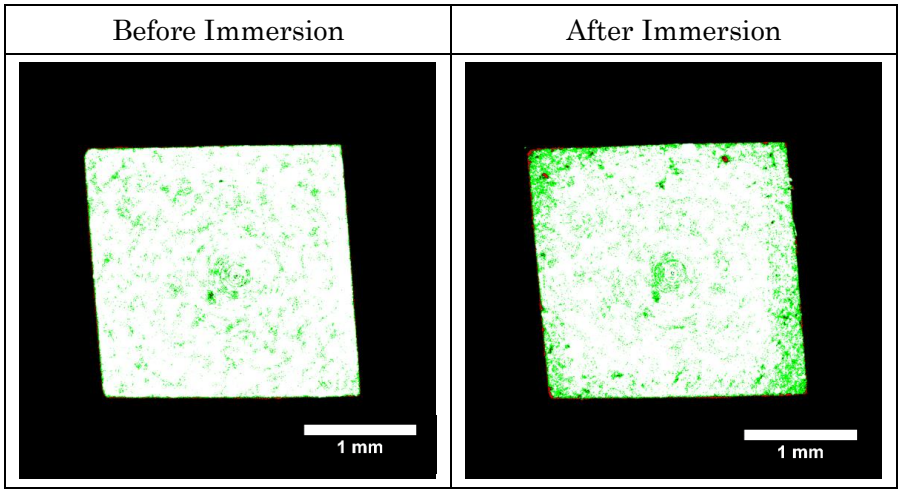


Figure 5-15 Visualization of leaching area: 400℃

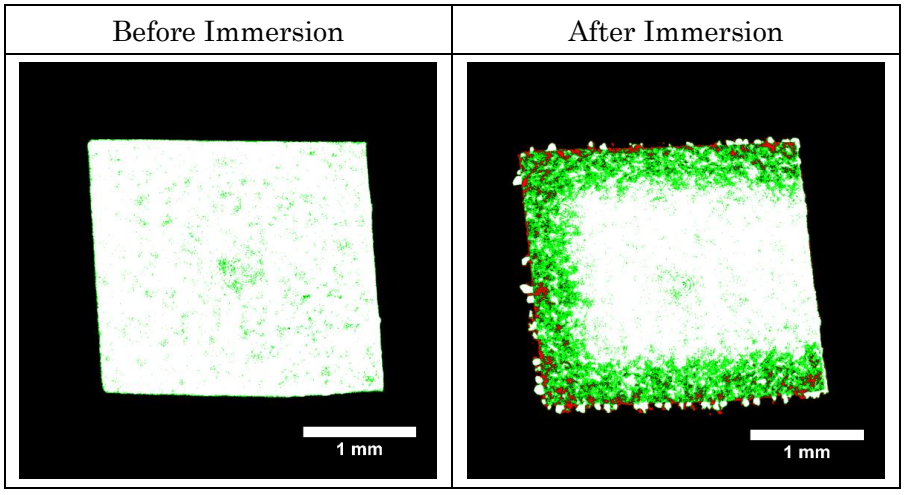


Figure 5-16 Visualization of leaching area: 600℃

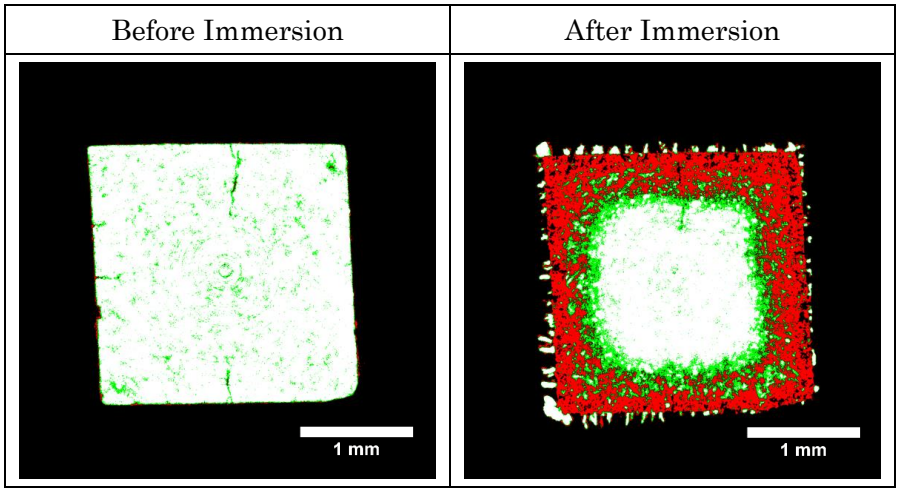


Figure 5-17 Visualization of leaching area: 800℃

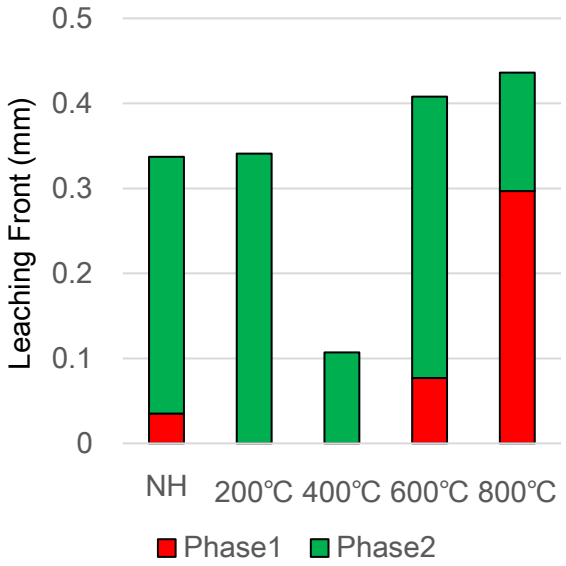


Figure 5-18 Leaching front for each sample measured from segmented images

samples showed that C-NH and C-2 resulted in 0.34 mm in leaching depth, and leaching depth of C-6 became deeper, 0.41mm including increased phase 1. The surface of C-8 altered to phase 1 mostly, and the depth is 0.44mm.

5.4.4 Results of XRD measurement

Regions of interests were determined for XRD measurements as point 1 to point 4 from the corner to the center (shown in Fig. 5-4 ~ 5-8 as circle).

Figure 5-17 ~ 5-21 show the XRD profiles of each sample before and after immersion test for

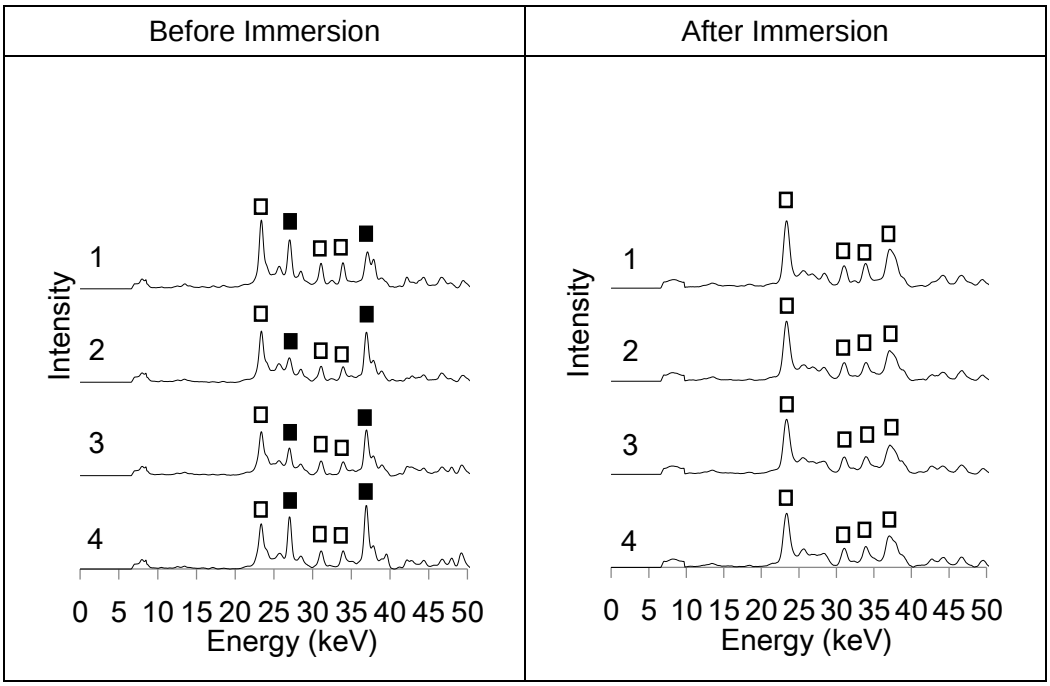


Figure 5-19 XRD profile: NH (alite:▲, belite:○, portlandite:■ , calcite:□ , vaterite:♦ , lime:●)

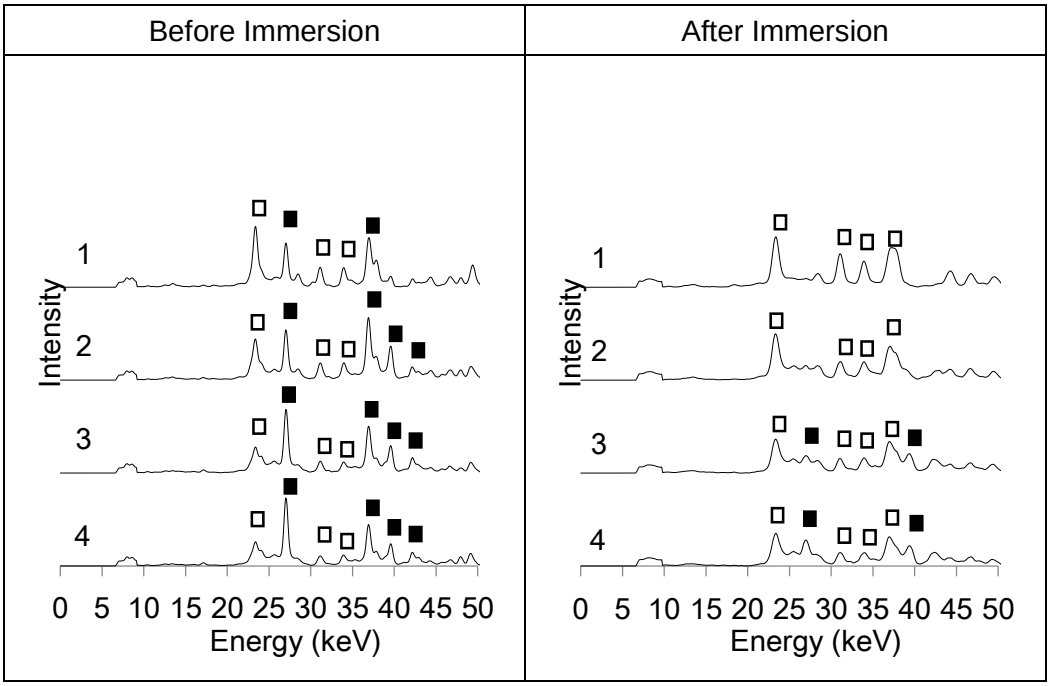


Figure 5-20 XRD profile: 200℃ (alite:▲, belite:○, portlandite:■ , calcite:□ , vaterite:♦ , lime:●)

the Point 1 to Point 4. With regard to C-NH, the peaks of both Portlandite and Calcite can be seen at all points before immersion and the peaks of Portlandite disappeared after immersion. It indicates that Portlandite dissolved into water from all area. In the case of C-2, similar trend can

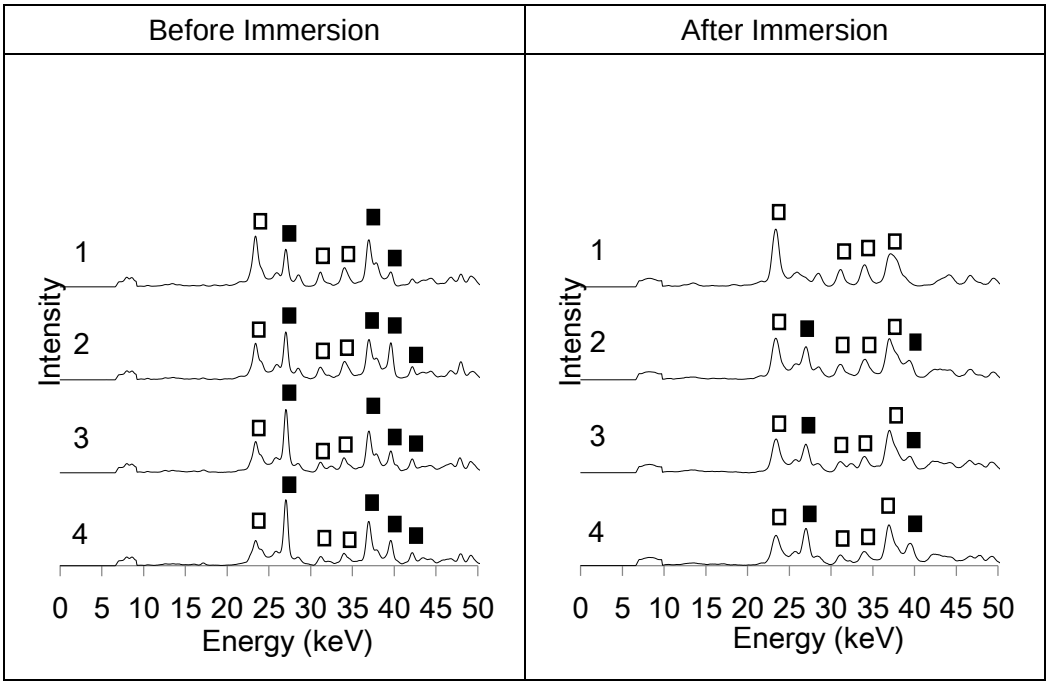


Figure 5-21 XRD profile: 400℃ (alite:▲, belite:○, portlandite:■ , calcite:□ , vaterite:♦ , lime:●)

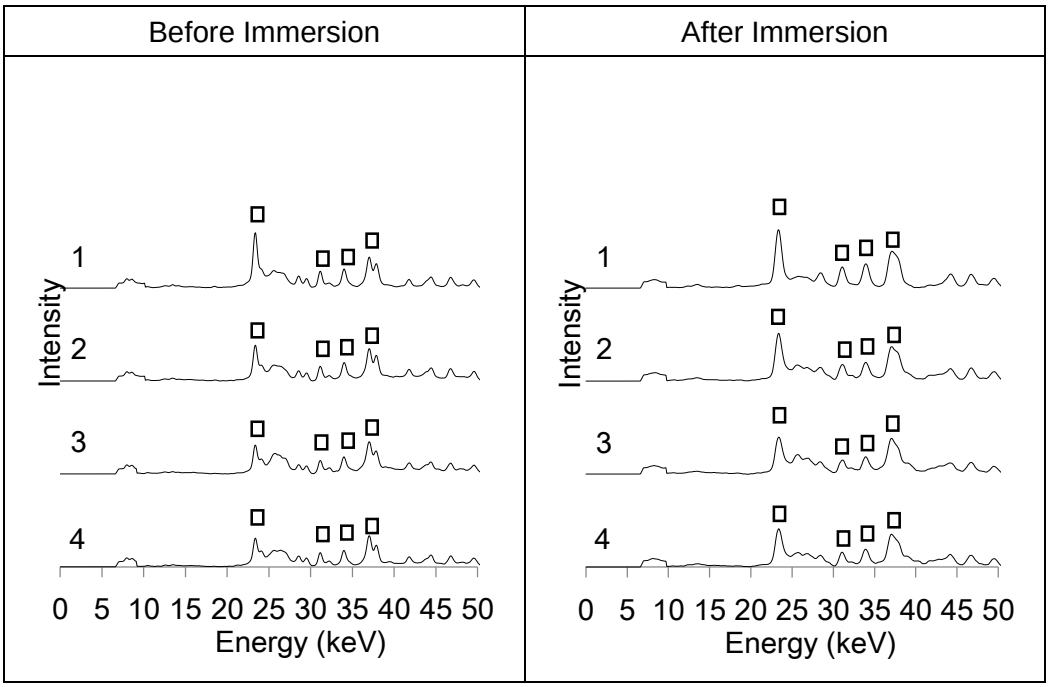


Figure 5-22 XRD profile: 600℃ (alite:▲, belite:○, portlandite:■ , calcite:□ , vaterite:♦ , lime:●)

be seen in C-4; the weakened peaks of Portlandite were observed in Point 2, 3 and 4. This result confirmed increase of resistance against leaching as shown in CT results. The profiles of C-6 show that almost all no change can be seen before and after immersion and the peaks of Calcite

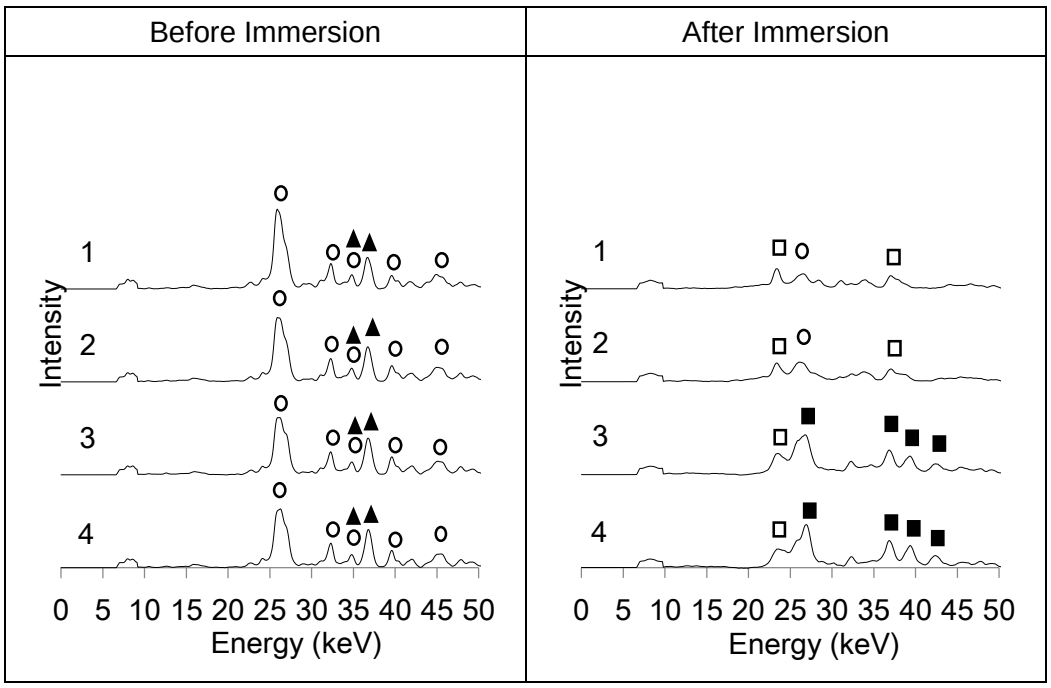


Figure 5-23 XRD profile: 800℃ (alite:▲, belite:○, portlandite:■ , calcite:□ , vaterite:♦ , lime:●)

can be detected but the peaks of Portlandite cannot be detected. It indicates that the initial presence of Portlandite affected rapid dissolution of C-S-H. Concerning the profiles of C-8, the peaks of Alite and Belite were found clearly before immersion at all points. It was considered that these productions derived from the decomposition of C-S-H. After immersion, however, the peaks of Portlandite can be seen at Point 3 and 4 and only tiny peaks of Calcite and Belite were observed at Point 1 and 2. Moreover, the peaks of Alite and Belite disappeared at all. These indicate that clinker-based minerals were rehydrated to produce Portlandite in all depth meanwhile the dissolution of the Portlandite produced by the rehydration occurred in Point 1 and Point 2.

5.5 EFFECT OF ENVIRONMENT AFTER HEATING

5.5.1 Cross section image

Figure 5-22 ~ 5-24 show cross sectional image of both samples at each measurement time at given height. Each slice was processed a matrix size into 1400×1400 pixels. Compared between 1st and 2nd measurement, occurrence of crack generation is significant for both measurements. It can be said that cracks are concentrated around aggregate, which is derived from the difference of thermal expansion coefficient between the aggregate and cement paste. Moreover, crack are formed in the aggregate of W sample. It can be considered that the difference of elastic modulus is affected or bond strength between aggregate and cement paste is high. According to the

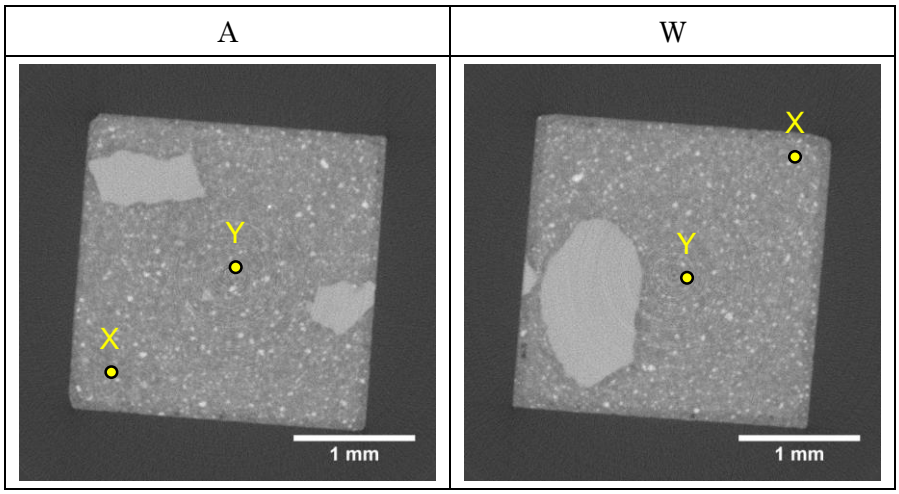


Figure 5-24 Cross sectional images at 1st measurement

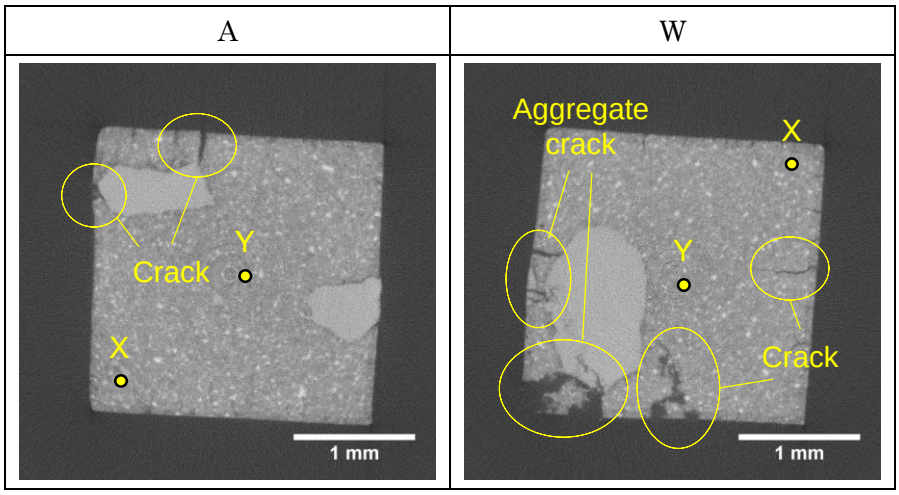


Figure 5-25 Cross sectional images at 2nd measurement

difference between 2nd and 3rd measurement, the formation of new crack can be observed in some area. On the other hand, disclosure of crack can be found in W sample, which might be derived from the effect of water re-curing.

5.5.2 Quantitative analysis of crack generation

To quantify the amount of crack generation, Region of Interest (ROI) was set in the center of each sample, which consists of continuous 800 slices. With stacking up all slices, 3D images in the scanning area can be obtained. The way to extract the aggregate and crack area follows the method described in Section 3.3. Figure 5-25 shows the 3D image of ROI and extraction of aggregate and crack.

Table 5-3 shows the results of information about aggregate and crack. According to this result,

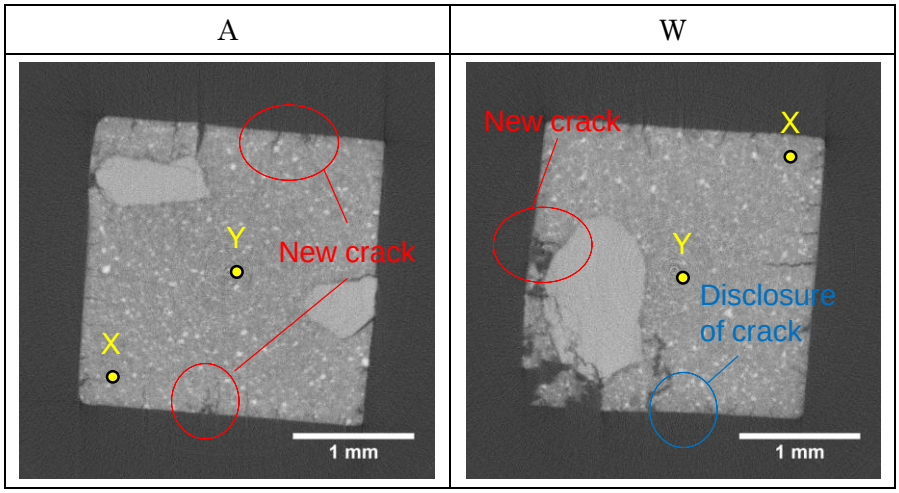


Figure 5-26 Cross sectional images at 3rd measurement

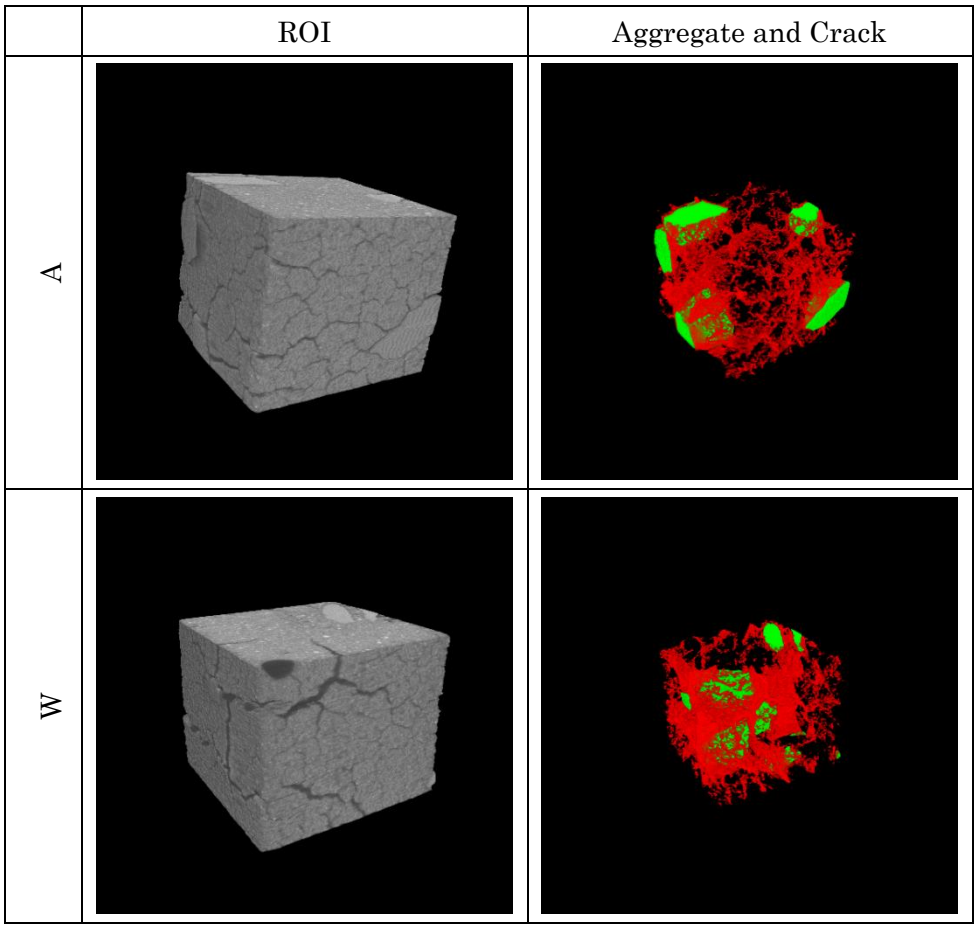


Figure 5-27 3D image of the ROI and aggregate and crack

crack ratio is in proportion to aggregate ratio. Increasing rate of sample A is about 6.4 times larger than that of W. This implies that water re-curing have an effect on restraining propagation

Table 5-3 Quantitative results of aggregate and crack

Sample		A	W
Aggregate ratio		0.047	0.062
2nd	Crack ratio	0.025	0.048
	Mean crack width (mm)	0.026	0.029
	Maximum crack width (mm)	0.098	0.083
3rd	Crack ratio (3rd)	0.035	0.051
	Mean crack width (mm)	0.026	0.030
	Maximum crack width (mm)	0.10	0.074
Increasing rate of crack ratio		0.4	0.063

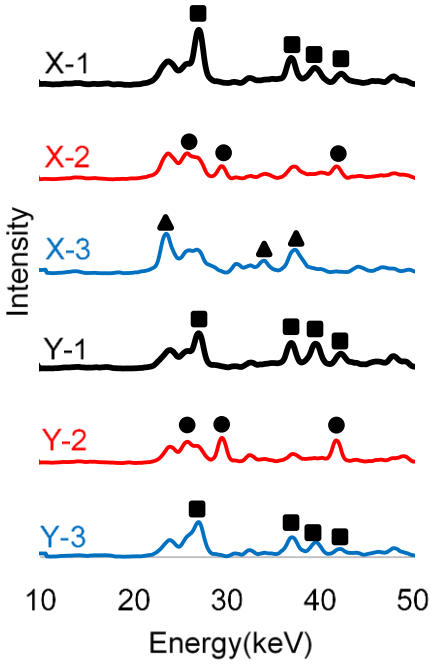


Figure 5-28 XRD profile: Sample A (calcite:▲, lime:●, portlandite:■)

of crack. According to mean crack width, almost all no change can be seen between 2nd and 3rd measurement. On the other hand, with regard to maximum crack width, sample A becomes larger whereas sample W becomes smaller. Henry et al. [7] pointed out the reduction of total pore volume after water re-curing because of the healing of connected pore space. This fact confirmed that disclosure of crack occurs by re-curing in water in this experiment.

5.5.3 Results of XRD measurement

As shown in Figure 5-22 ~ 5-24, XRD measurement point were set on the surface and center of

cement paste as Point X and Point Y, respectively. Then, the measurements were carried out at each measurement time. Figure 5-26 and 5-27 show XRD profiles for each sample. From Figure 5-26, XRD profiles of X-1 and Y-1 exhibit distinct peaks of portlandite. On the other hand, the peaks of lime can be found in the profiles of 2nd times, which means that the decomposition of portlandite occurred and lime generated at high temperature. The peaks of calcite are distinct in the profile of X-3 whereas the peaks of portlandite can be seen in that of Y-3. It derives from that calcite generated due to the contact with carbon dioxide of air outside specimen at Point X, and portlandite with less crystalline was reformed due to the reaction of lime with water vapor when cooling procedure [6]. Figure 5-27 indicated that same trend as sample A can be found out at 1st and 2nd measurement; the peaks of portlandite can be seen in the profiles of both points at 1st measurement and those of lime can be seen at 2nd measurement. This mechanism is derived from same reaction above explained. At 3rd measurement, the profiles of both points have same peaks of portlandite. It derived from that portlandite was reformed due to the contact with water, and this fact can be considered to restrain crack propagation.

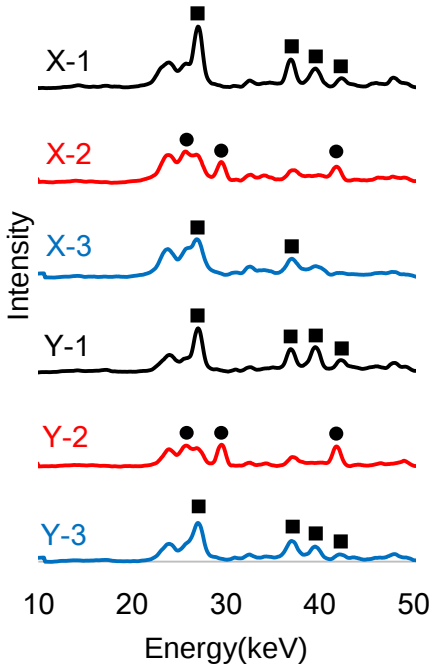


Figure 5-29 XRD profile: Sample W (calcite:▲, lime:●, portlandite:■)

5.6 SUMMARY

This chapter firstly explained the alteration mechanism of cement paste after exposed to high temperature for a long time. It was clarified that the decomposition of portlandite occurred after heated more than 12 hours. Next, the alteration mechanism of carbonated cement paste after the exposure to various maximum temperatures and immersion in pure water was investigated by non-destructive integrated CT-XRD method. CT image analysis revealed that the carbonated cement paste heated at 400 °C exhibited the largest resistance against leaching in water immersion. It appeared to be due to the densification of the internal structures. Moreover, while alite and belite were generated in the cement paste due to heating at 800 °C, they could rehydrate themselves and form portlandite by immersion in pure water. Subsequently, however, its dissolution occurred at the surface layer and the structure of cement hydration system became the most coarsened.

Moreover, this chapter included the investigation of quantitative crack analysis after heating and after re-curing in air or water. The obtained results indicated the reduction of increasing rate of crack propagation by water re-curing. XRD analysis figured out that calcite was generated at the surface of sample whereas portlandite was formed at the center of sample by air re-curing soon after heating. On the other hand, portlandite was confirmed at both surface and center of sample by water re-curing. Therefore, microstructure recovery was demonstrated from both geometrical and chemical analysis.

REFERENCES

[1] Architectural Institute of Japan (2017). “Guide book for fire-resistive performance of structural materials.” Maruzen publishing. (in Japanese)

[2] Saito, H., Tsuji, Y., and Kataoka, H. (2000). “A model for predicting the leaching degradation of cement hydrate.” *Concrete Research and Technology*, 11(1), 51-59. (in Japanese)

[3] Morandeau, A., Thiery, M., and Dangla, P. (2015). “Impact of accelerated carbonation on OPC cement paste blended with fly ash.” *Cement and Concrete Research*, 67, 226-236.

[4] Saad, M., Abo-El-Enein, S. A., Hanna, G. B., and Kotkata, M. F. (1996). “Effect of temperature on physical and mechanical properties of concrete containing silica fume.” *Cement and Concrete Research*, 26(5), 669-675.

[5] Ma, Q., Guo, R., Zhao, Z., Lin, Z., and He, K. (2015). “Mechanical properties of concrete at high temperature-A review.” *Construction and Building Materials*, 93, 371-383.

[6] Castellote, M., Alonso, C., Andrade, X., Turrillas, X., and Campo, J. (2004). “Composition

and microstructural changes of cement pastes upon heating, as studied by neutron diffraction." *Cement and Concrete Research*, 34(9), 1633-1644.

[7] Henry, M., Darma, I. S., and Sugiyama, T. (2014). "Analysis of the effect of heating and re-curing on the microstructure of high-strength concrete using X-ray CT." *Construction and Building Materials*, 67, 37-46.

CHAPTER 6 CONCLUSIONS

6.1 GENERAL CONCLUSIONS

In this thesis, research efforts have been given to clarify the microscopic mechanism of fire damage and the effect of water as a post heat treatment by use of newly method, non-destructive integrated CT-XRD method. Firstly, the development of this new method was explained followed by the proposal of microscopic image analysis method and verification of its XRD measurement by comparison with conventional powder XRD technique. Next, the effect of water attack was evaluated using deteriorated mortar specimen and discussed from microscopic viewpoint. Finally, the effect of water on damaged cementitious materials by high temperature was studied by doing immersion of purified water after heating at various maximum temperature.

Based on this study, general conclusions are summarized as follows.

1. Phase segmentation algorithm from CT images of mortars with different aggregates was developed, which can separate the phases into aggregate, cement paste, and void including crack. Two image filtering methods; one is anisotropic diffusion filtering to extract aggregate area and the other is un-sharp mask filtering to extract crack area, are utilized.
2. Regardless of limitation to detect the intensity peaks in the range of less than 25°, non-destructive integrated CT-XRD method can evaluate the peak positions and thus evaluate microscopic alteration of internal structure in non-destructive manner. In addition, minerals of aggregate inside sample can be identified properly.
3. In the cement paste heated at 600 °C, the presence of portlandite was observed in the profile of the CT-XRD. It can be considered that the portlandite was reformed during cooling. However, its formation was hardly observed in the profile of powder XRD. Hence the portlandite with less crystalline nature might be destroyed in the process of the grinding to prepare the powder.
4. Alteration of deteriorated mortar due to water flow was investigated by using non-destructive integrated CT-XRD method and it was found that Portlandite in the cement paste around aggregate near crack was dissolved after 4 days' water flow. The corresponding region of the paste was disappeared after 3.5 months' water flow.
5. In case of that the cement paste was exposed to 400°C, the decomposition of portlandite was observed when exposed for 12 hours or more and crack amount also increased

correspondingly.

6. From CT image analysis for specimens before and after immersion, the cement paste that was carbonated and then heated at 400 °C exhibited the largest resistance against leaching in water immersion. It appeared to be due to the densification of internal structures.
7. While alite and belite were generated in the cement paste due to heating at 800 °C, they could rehydrate themselves and form portlandite by immersion in pure water. However, its dissolution occurred at the surface layer and the structure of cement hydration system most coarsened.
8. Quantification analysis of crack geometry revealed that water re-curing for damaged sample due to high temperature was effective to restrain of crack propagation. Simultaneous XRD measurement implied that this is because of reformation of portlandite.

6.2 RECOMMENDATIONS FOR FUTURE RESEARCH

6.2.1 Application of non-destructive integrated CT-XRD method

This research program demonstrated the vast array of experimental possibilities offered by the application of non-destructive integrated CT-XRD method. Throughout this experimental process, it became clear that this methodology can provide the distribution of constituents of cementitious materials. This fact can lead to significant benefits for conducting advanced research.

Some of the most useful study areas are in computational deterioration modeling based on X-ray CT images. Through the combination of image data with material characteristics, any damage trends could be mathematically quantified and directly implemented to link mechanical performance which was roughly modeled by other conventional method.

On the other hand, as for XRD analysis, there are still much rooms remaining in both qualitative and quantitative evaluation. As discussed in Chapter 3, limitation to detect the intensity peaks exists, which cannot allow us to observe AFm or AFt phases. Some anions of these phases can be substituted by other anions like chloride ions or sulfate ions, which indicate the penetration of these or not in cement hydration products. Therefore, the evaluation of these phases enables us to clarify the alteration mechanism more precisely. In addition, this can lead to do quantitative analysis; one of representative method is Rietveld method. To realize the application of this method is surely valuable to reveal the alteration modeling of every intrusion factors.

6.2.2 Alteration of cementitious materials subjected to high temperature and continuous contact with water

In this thesis, the uncovered problems of alteration mechanisms subjected to high temperature

and water were addressed. The new findings from this research is worthy for cement and concrete research field. However, the followings points are still remained to discuss more.

In Chapter 4, the alteration of water attack to deteriorated mortar is introduced and significant damage action is revealed. However, the effect of difference between water flow and immersion is still unclear. Moreover, it cannot be clarified that the difference between cement paste and mortar, that is to say the existence of interfacial transition zone affects the alteration mechanism or not. Water flow includes the physical pressure on cementitious materials and thus affect the deterioration behavior. In addition, this has an effect on the mechanism of transportation phenomena. This point should be discussed more to make an accurate prediction by comparing water flow test with immersion test.

Moreover, Chapter 5 explains the effect of water on alteration of cementitious materials as post heating process. However, the experimental work using mortar was not discussed sufficiently in this point. It should be considered that how the presence of aggregate and the stress of water flow affect degradation behavior to make a scenario after concrete is damaged by high temperature.

APPENDIX A IMAGE FILTERING

A.1 Filtering

A.1.1 Anisotropic Diffusion

Anisotropic diffusion algorithm was implemented using one of the plugins of ImageJ known as anisotropic diffusion 2D. This algorithm plays a role in removing noise while preserving the edges. Table A-1 shows the variable numbers which can be adjusted in our operation of anisotropic diffusion. The left side in Figure A-1 shows raw image dataset to indicate the effect of any processing as shown in following sections. Image size was processed into 1400×1400 pixels. The reference line which is the basis of evaluation are drawn in the horizontal direction starting from x=400 and y=450, and the length is set as 700 pixels. The right side in Figure A-1 indicates the GSV value corresponding to the position of drawn line.

Table A-1 Variable number and initial settings [with short notation]

Variable number	Initial settings
Number of iterations [N]	20
Smoothings per iteration [S]	1
Diffusion limiter along minimal variations [D min]	0.5
Diffusion limiter along maximal variations [D max]	0.9
dt (Time step)	20
Edge threshold height [E]	5

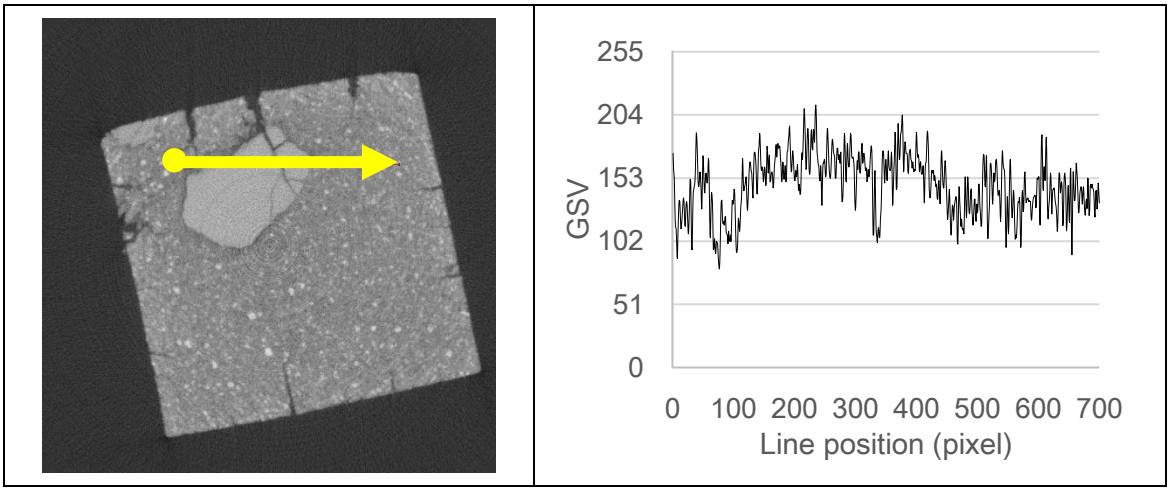


Figure A-1 Initial image dataset for anisotropic diffusion filter processing (left: The image with reference line, right: Line profile corresponding to the line)

A.1.1.1 Effect of number of iterations

Figure A-2 shows the results of image processing which can argue the effect of number of iterations. The numbers of other items are fixed as shown in Table A-1.

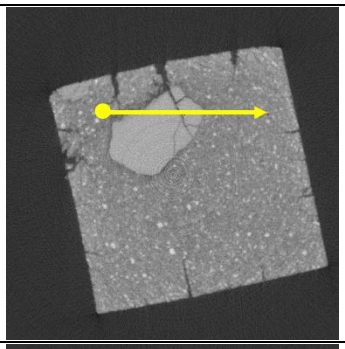
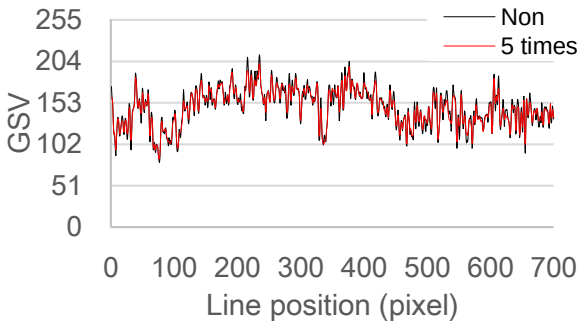
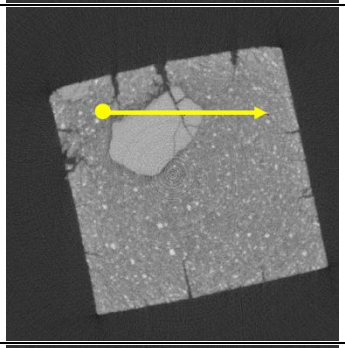
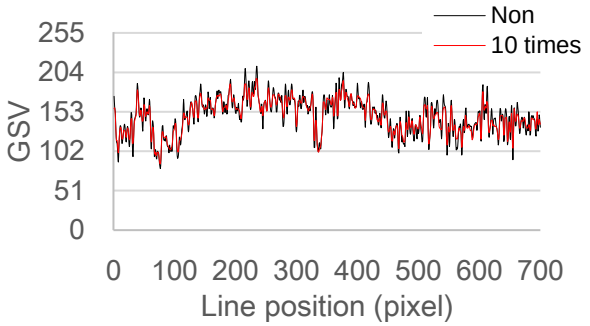
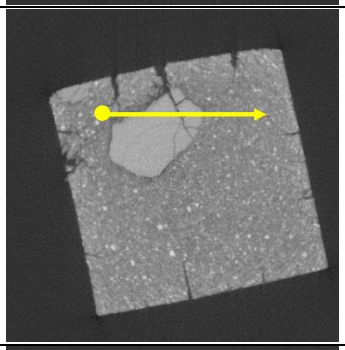
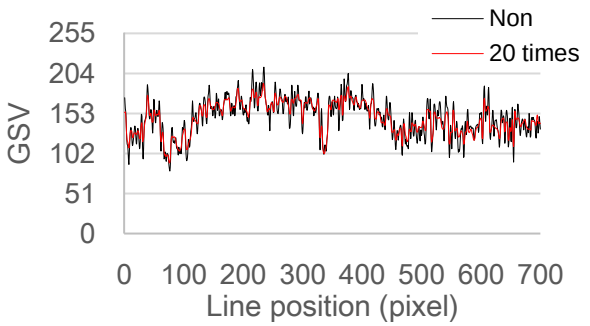
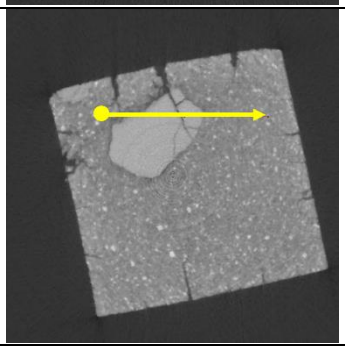
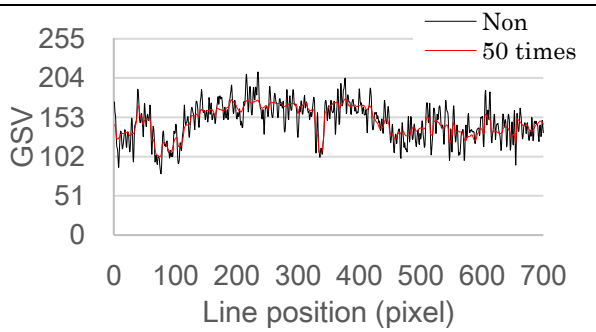
N	Image	Line profile
5		
10		
20		
50		

Figure A-2 The effect of number of iterations

A.1.1.2 Effect of smoothing per iteration

Figure A-3 shows the results of image processing which can argue the effect of smoothing per iteration. The numbers of other items are fixed as shown in Table A-1.

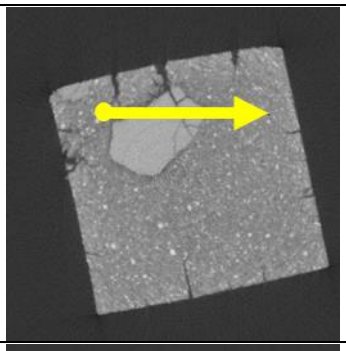
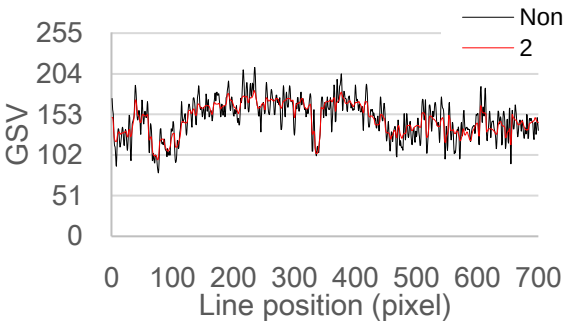
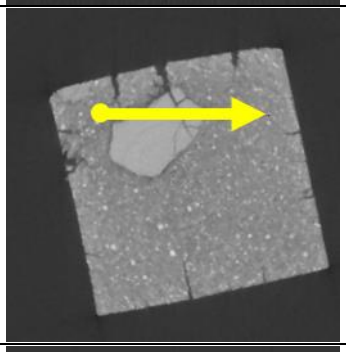
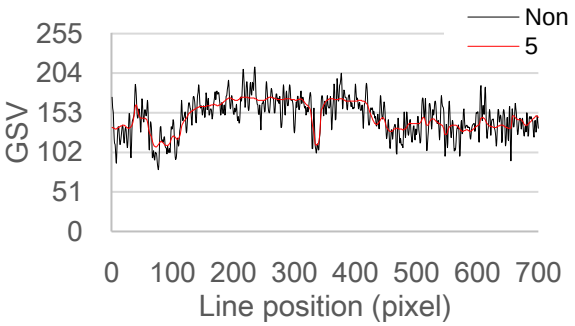
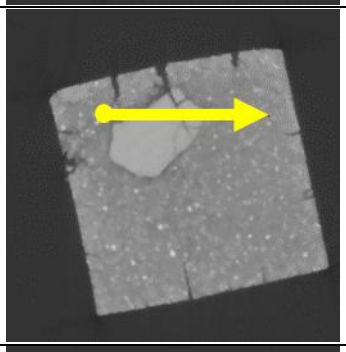
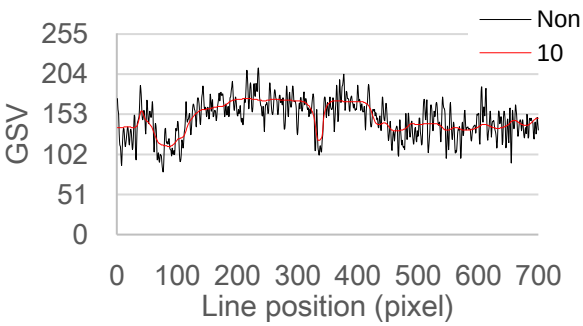
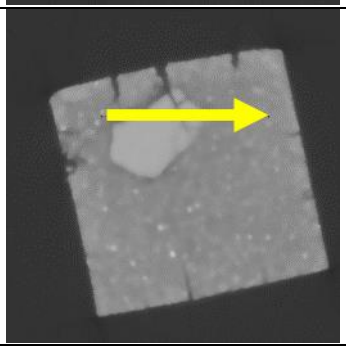
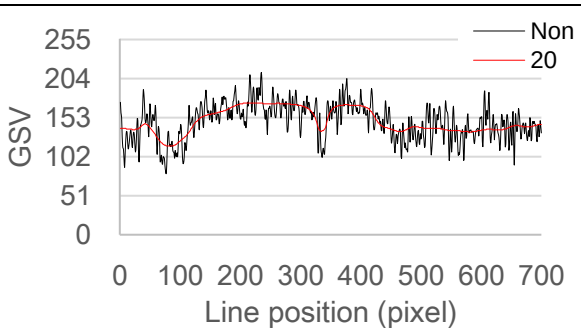
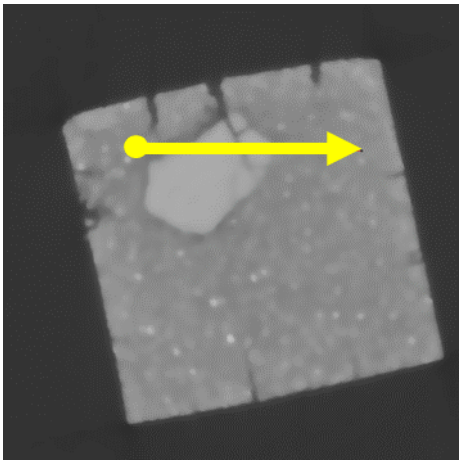
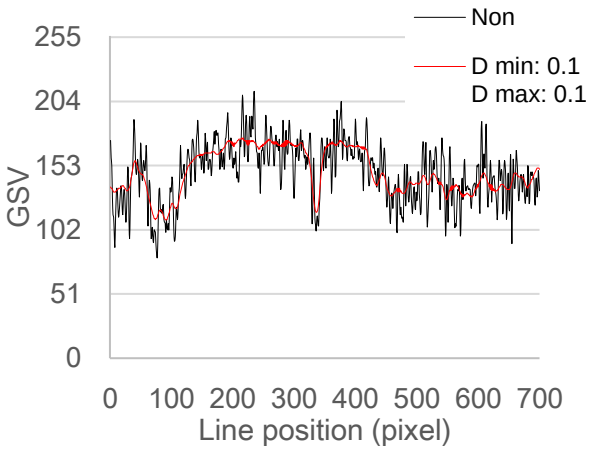
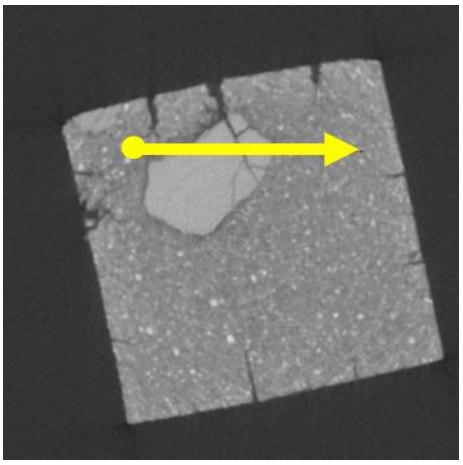
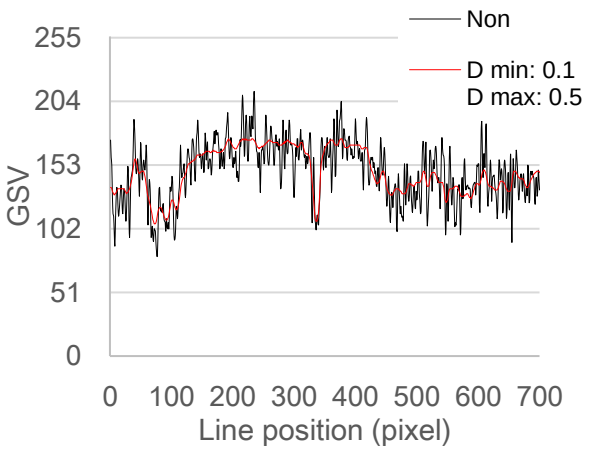
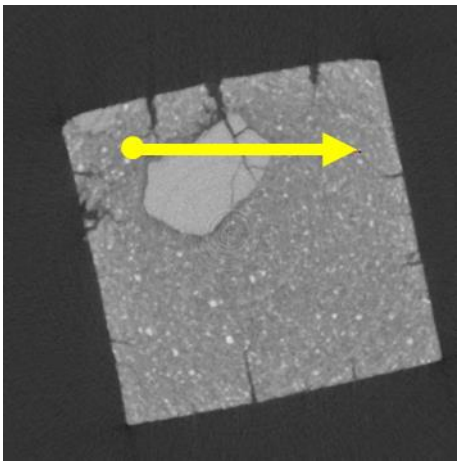
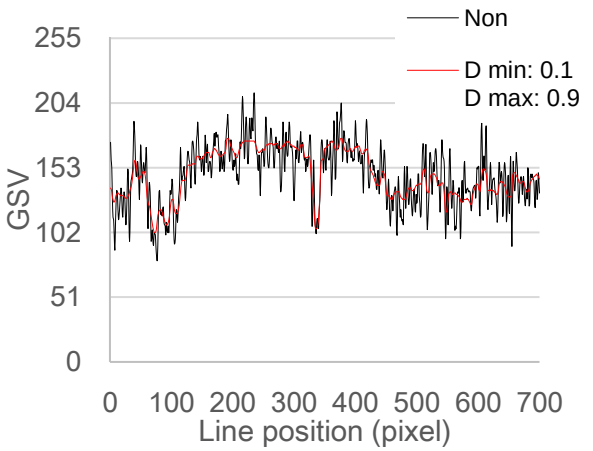
S	Image	Line profile
2		
5		
10		
20		

Figure A-3 The effect of smoothing per iteration

A.1.1.3 Effect of diffusion limiter

Figure A-4 shows the results of image processing which can argue the effect of diffusion limiter. The numbers of other items are fixed as shown in Table A-1.

D min D max	Image	Line profile
0.1 0.1		
0.1 0.5		
0.1 0.9		

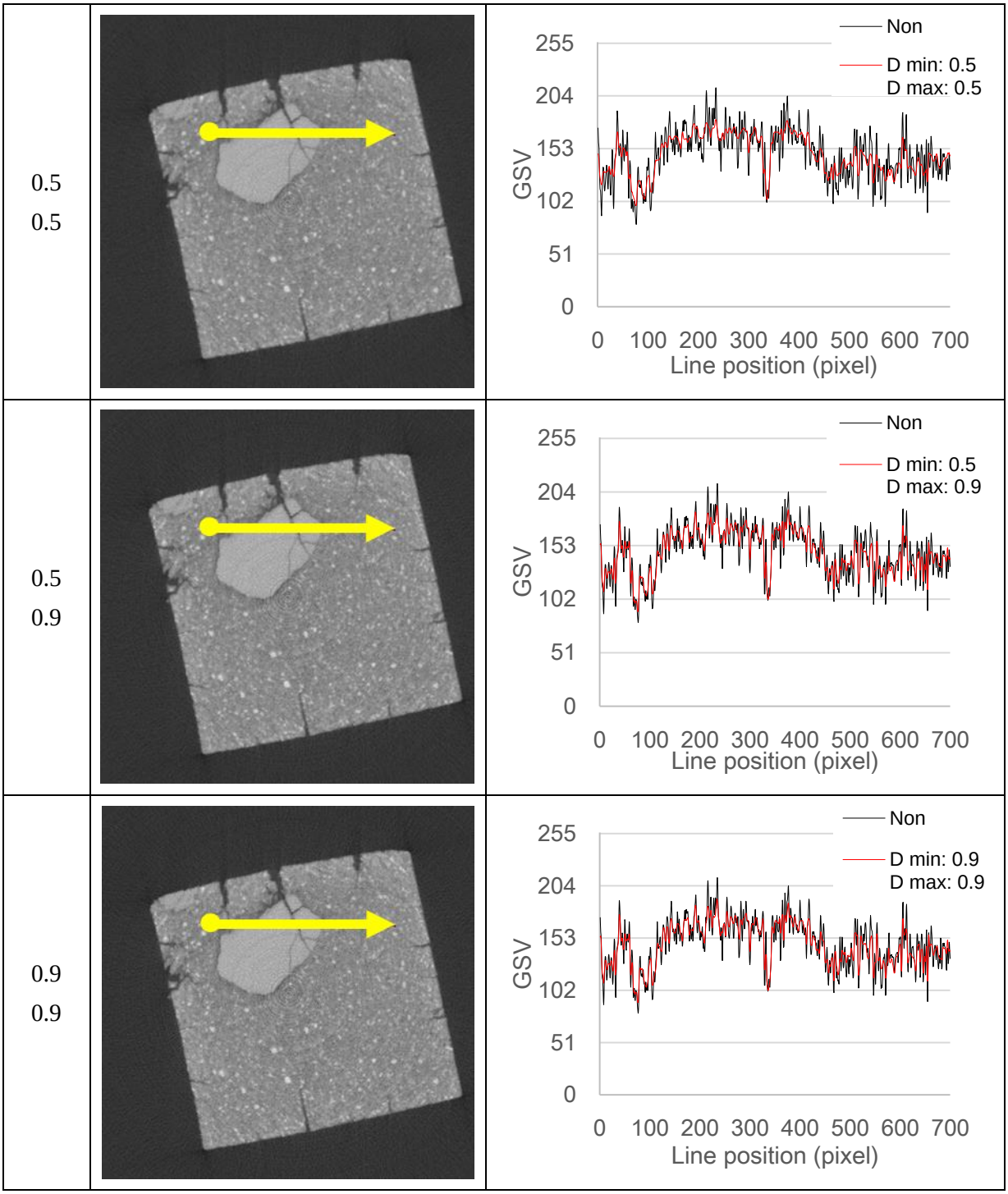


Figure A-4 The effect of diffusion limiter

A.1.1.4 Effect of time steps

Figure A-5 shows the results of image processing which can argue the effect of time steps. Other items are fixed as shown in Table A-1.

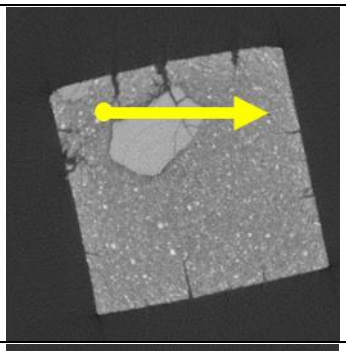
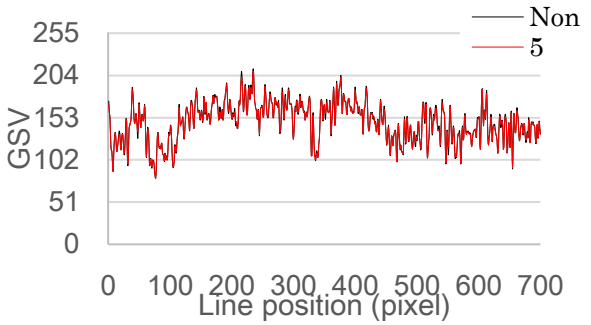
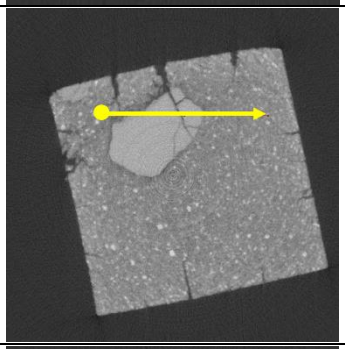
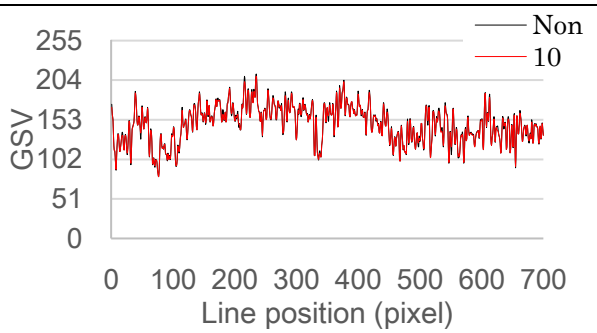
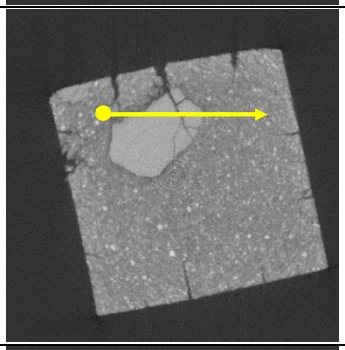
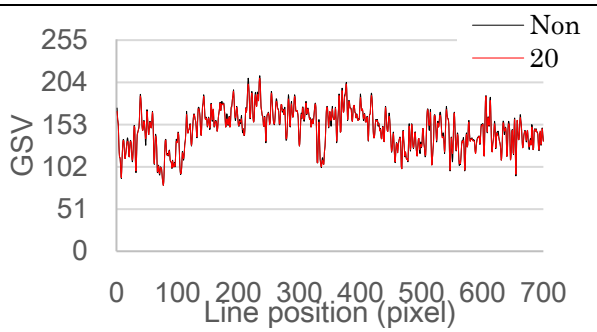
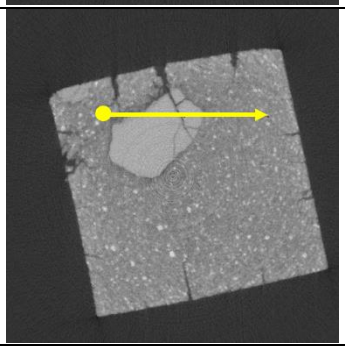
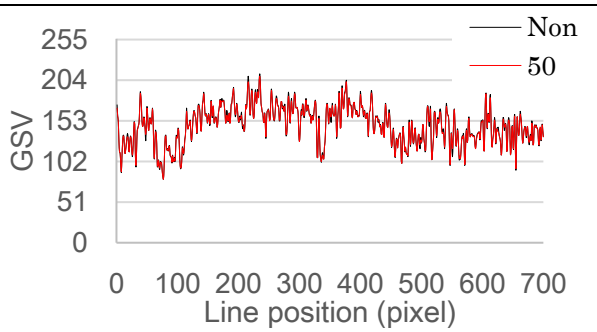
dt	Image	Line profile
5		
10		
20		
50		

Figure A-5 The effect of time steps

A.1.1.5 Effect of edge threshold height

Figure A-6 shows the results of image processing which can argue the effect of edge threshold height. The numbers of other items are fixed as shown in Table A-1.

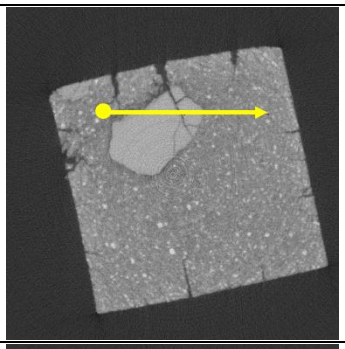
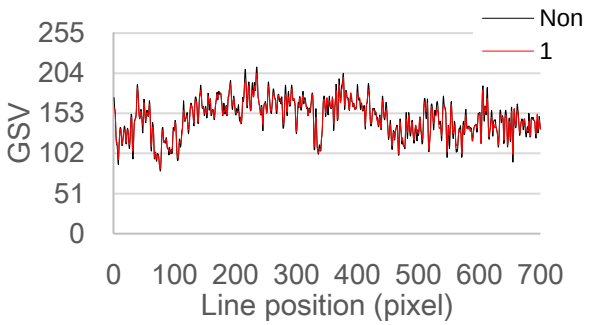
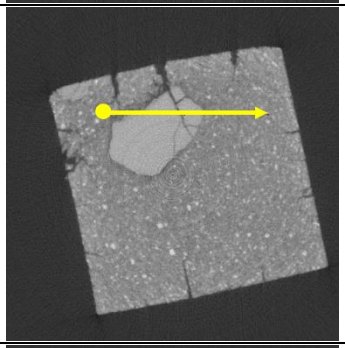
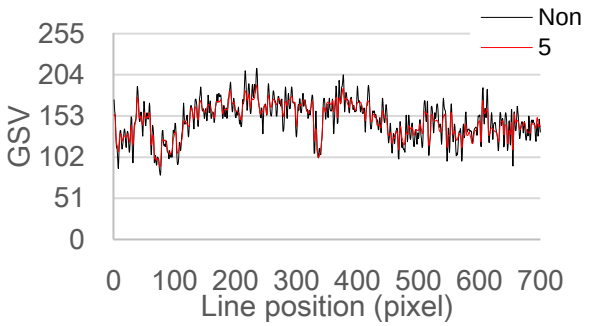
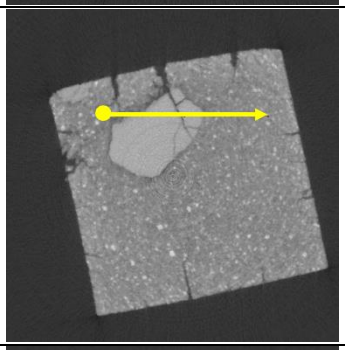
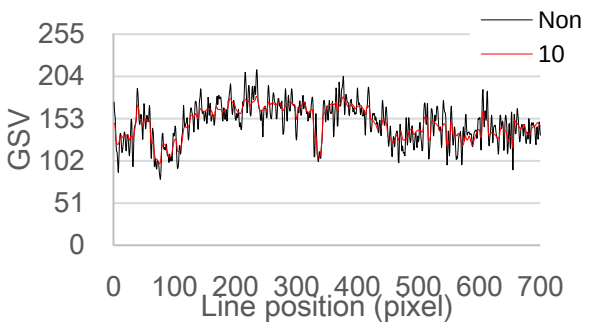
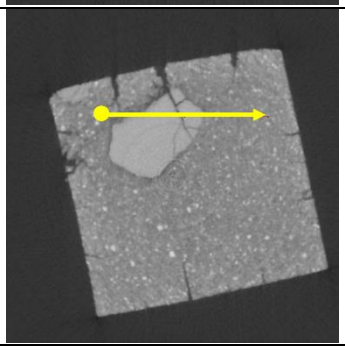
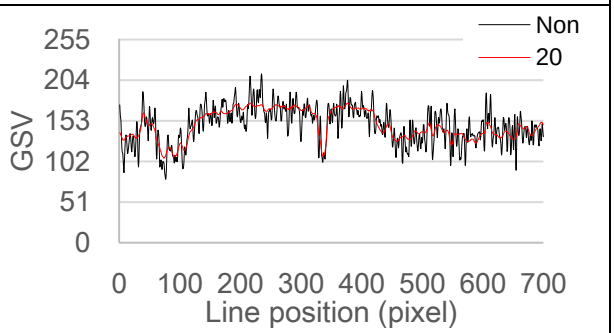
E	Image	Line profile
1		
5		
10		
20		

Figure A-6 The effect of edge threshold height

A.1.2 Unsharp mask

Unsharpmask was implemented using one of the functions of ImageJ known as unsharp mask in filters. Unsharp masking subtracts a blurred copy of the image and rescales the image to obtain the same contrast of large (low-frequency) structures as in the input image. This is equivalent to adding a high-pass filtered image and thus sharpens the image. Table A-2 shows the variable number and initial settings which can be adjusted in our operation of unsharp mask. Radius is the standard deviation (blur radius) of the Gaussian blur that is subtracted. Mask Weight determines the strength of filtering, whereby Mask Weight=1 would be an infinite weight of the high-pass filtered image that is added. The left side in Figure A-7 shows the image dataset to be processed to indicate the effect of any processing as shown in following sections. The image filtered as N=50, S=1, Dmin=Dmax=0.1, dt=20, and E=5 was used. The reference line which is the basis of evaluation are drawn same as A.1.1. The right side in Figure A-7 indicates the GSV value corresponding to the position of drawn line.

Table A-2 Variable number and initial settings [with short notation]

Variable number	Initial settings
Radius [R]	1.0
Mask Weight [M] (0.1~0.9 are available)	0.6

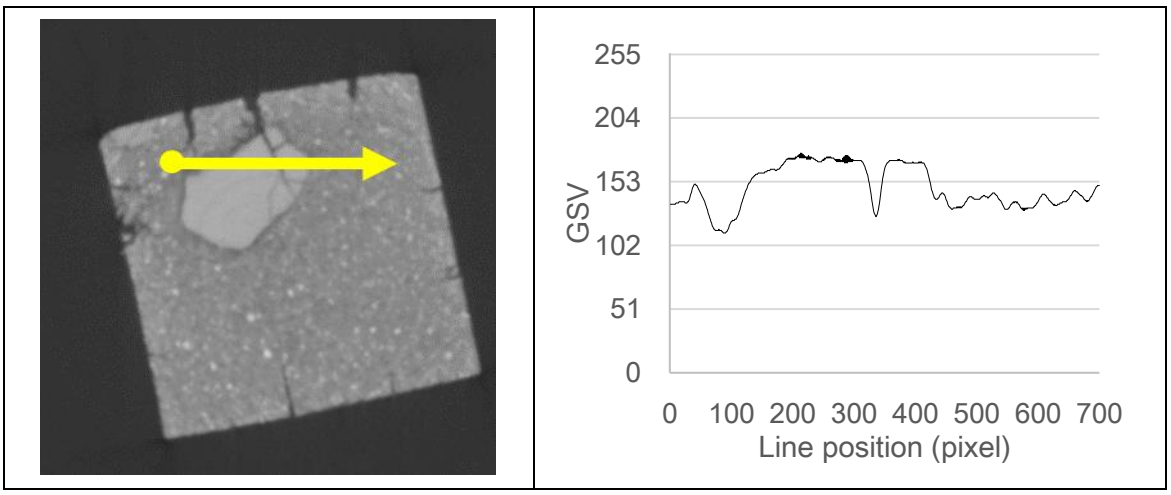


Figure A-7 Initial image dataset for unsharp mask filter processing (left: The image with reference line, right: Line profile corresponding to the line)

A.1.2.1 Effect of radius

Figure A-8 shows the results of image processing which can argue the effect of radius.

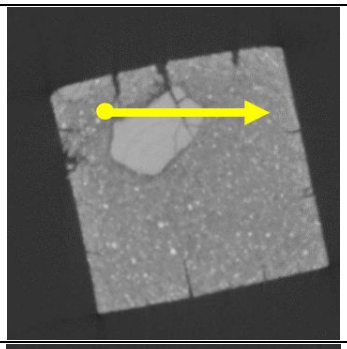
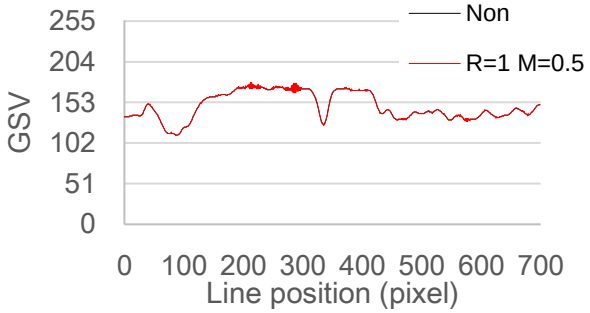
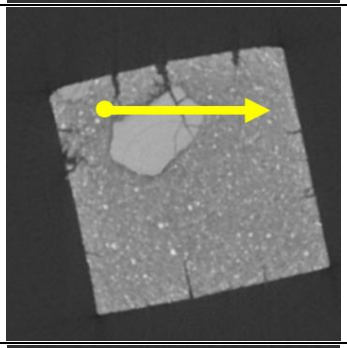
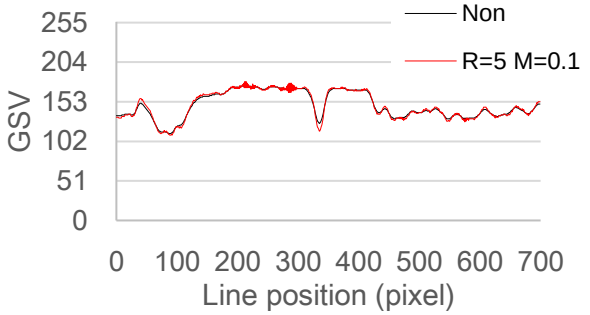
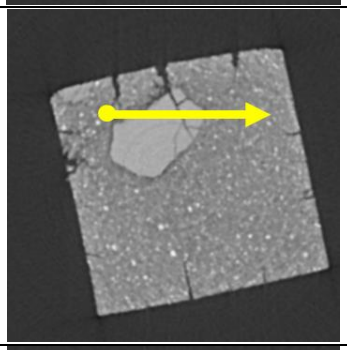
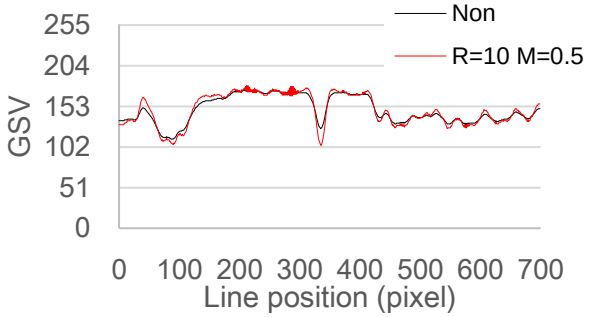
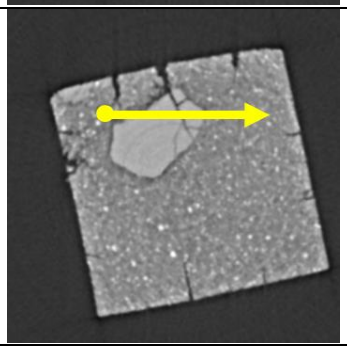
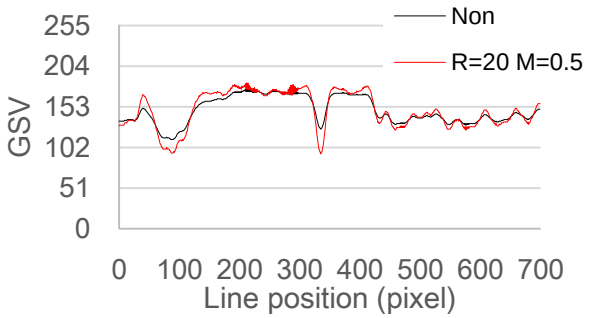
R M	Image	Line profile
1 0.5		
5 0.5		
10 0.5		
20 0.5		

Figure A-8 The effect of radius

A.1.2.2 Effect of mask weight

Figure A-9 shows the results of image processing which can argue the effect of number of mask weight.

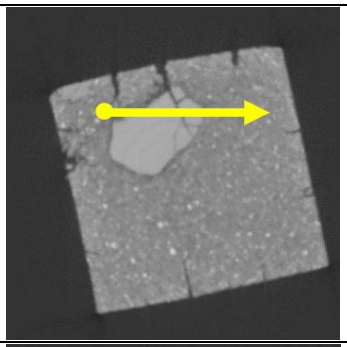
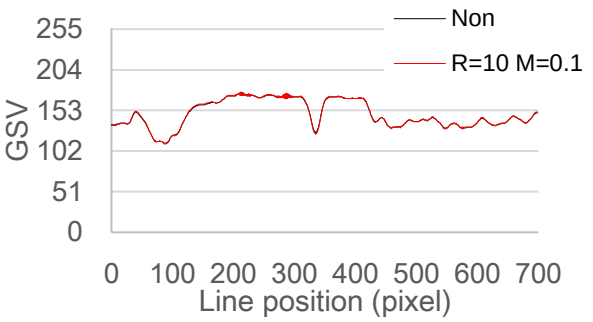
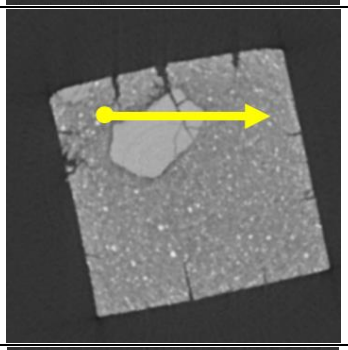
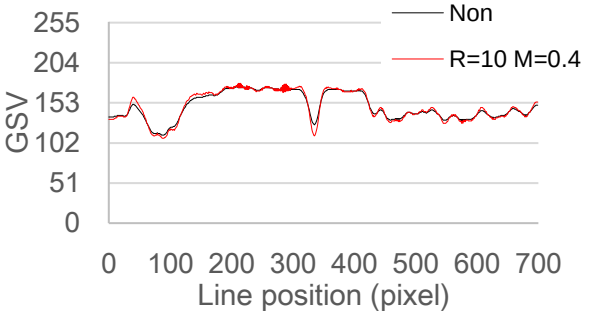
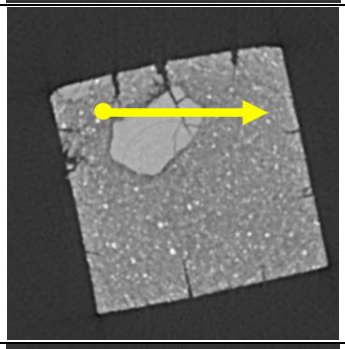
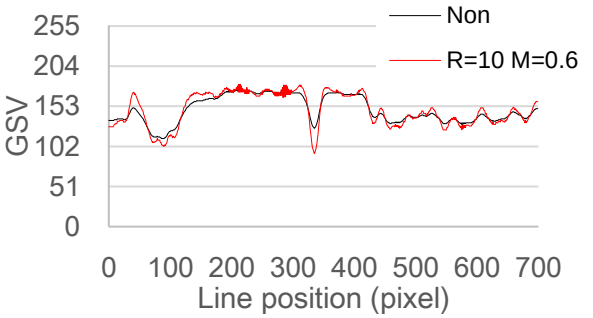
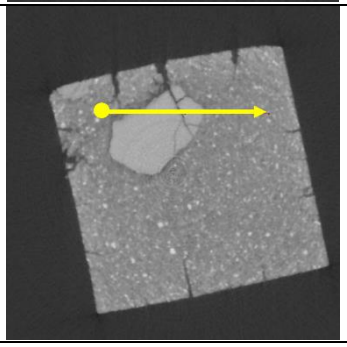
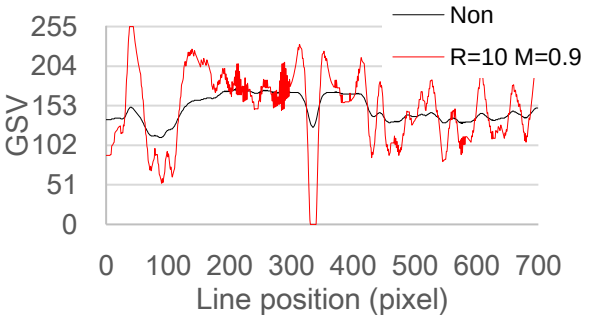
R M	Image	Line profile
10 0.1		
10 0.4		
10 0.6		
10 0.9		

Figure A-9 The effect of mask weight

APPENDIX B EFFECT OF DURATION TIME OF HEATING ON LEACHING

To investigate the time dependency of duration time, a slight different experiment from Experiment 1 as described in Chapter 5 as conducted. Sample was the same as the explained in Section 5.2.1.1. Cement paste with only the Ordinary Portland Cement was used in this experiment with a water to cement ratio of 0.6. After about 1 year curing, the hardened cement pastes were cut and carbonation test was provided in the same procedure written in Section 3.3.2. 12 hours added to duration time of maximum temperature in this heating test.

B.1 200°C

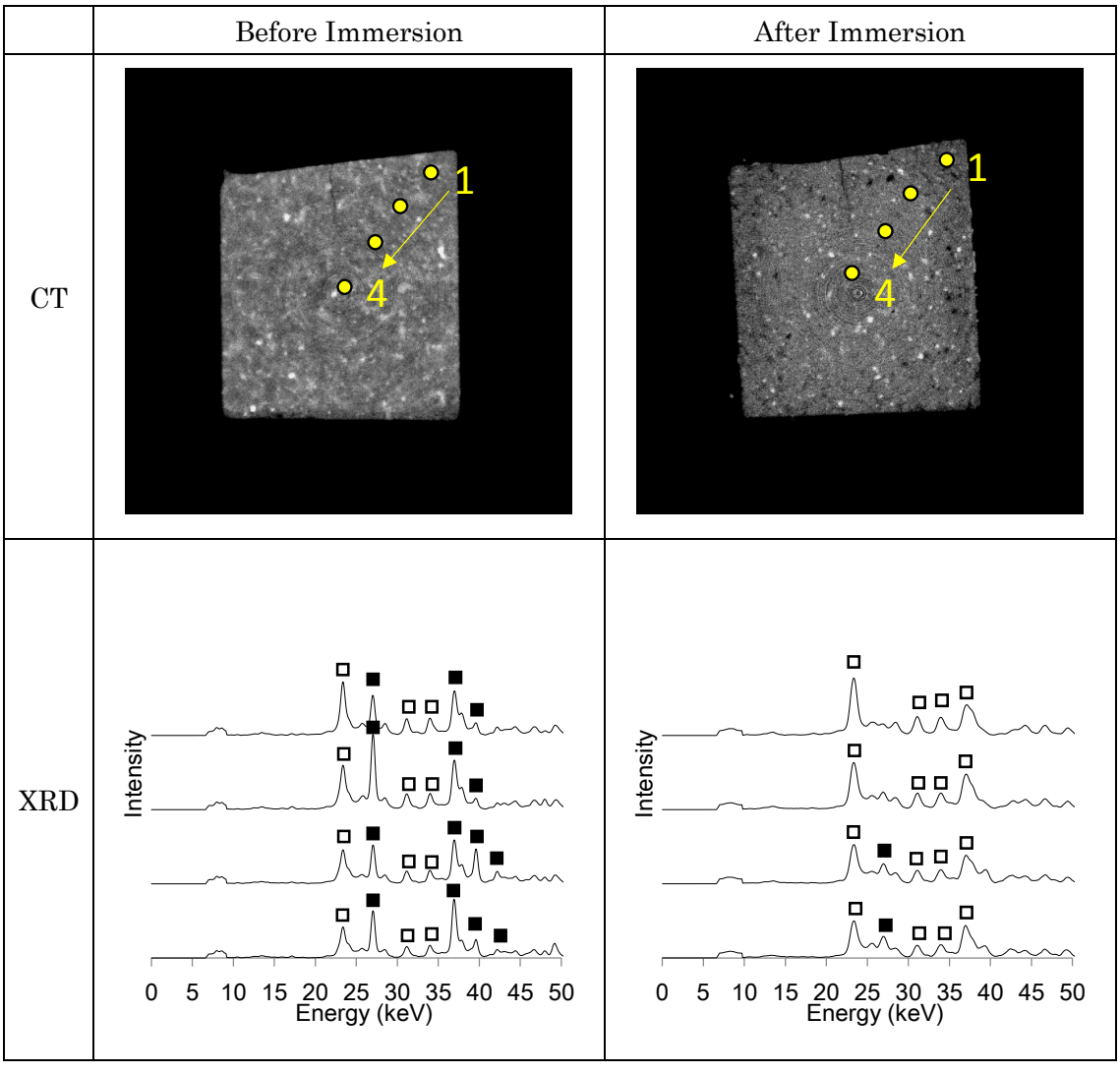


Figure B-1 Dataset of 200°C for 12 hours

B.2 400°C

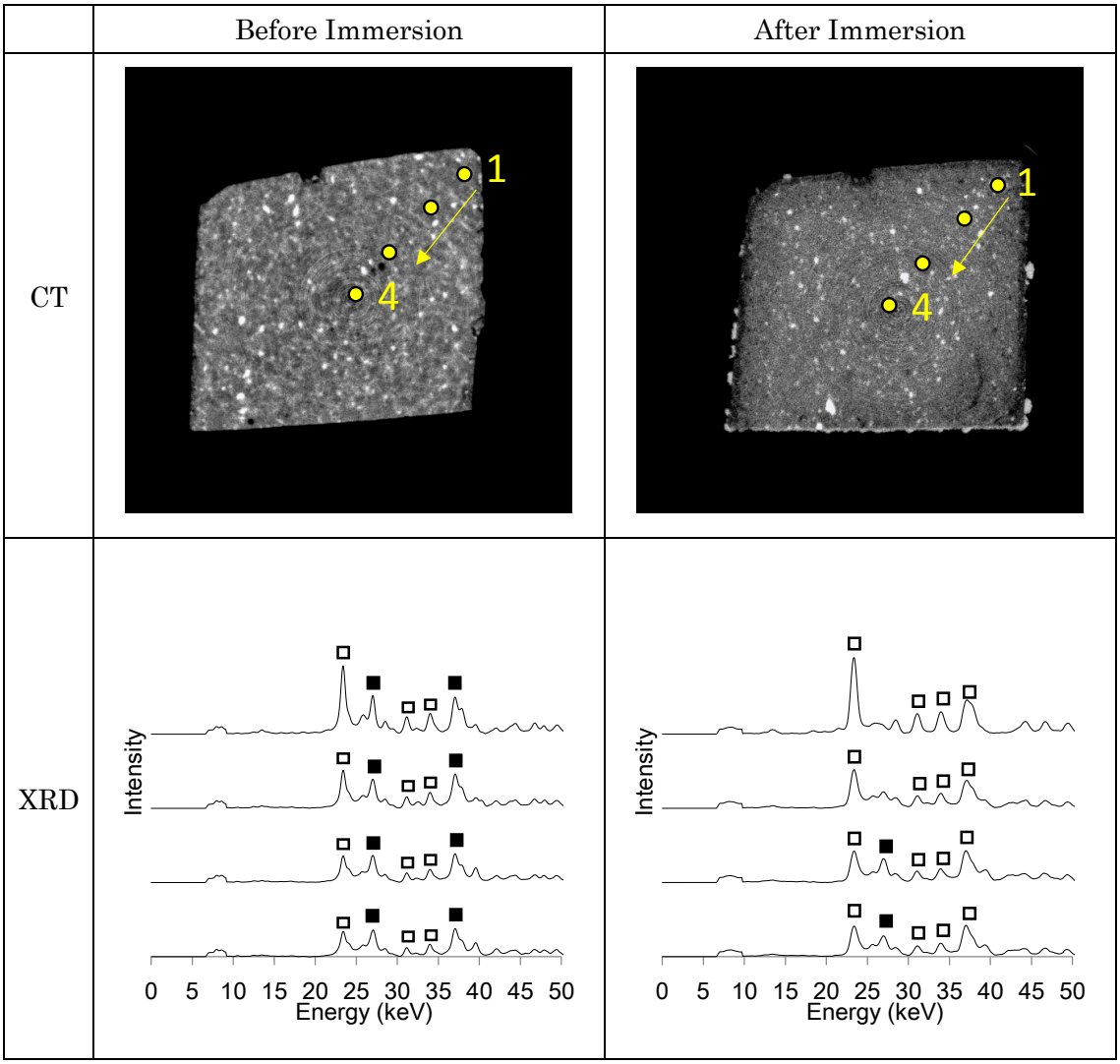


Figure B-2 Dataset of 400°C for 12 hours

B.3 600°C

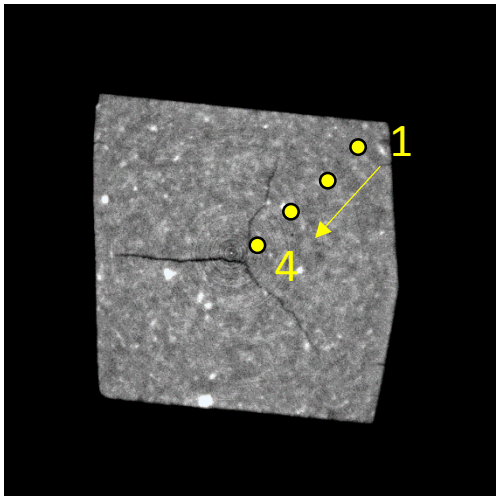
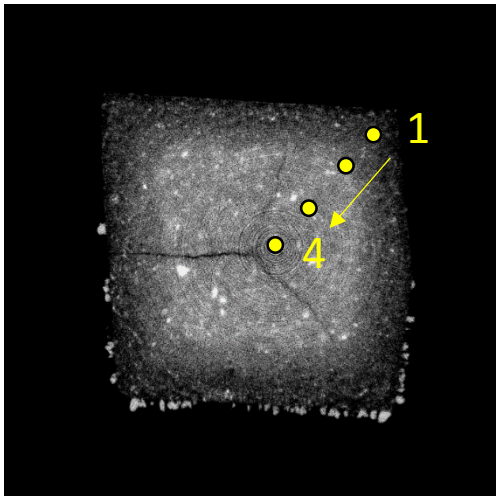
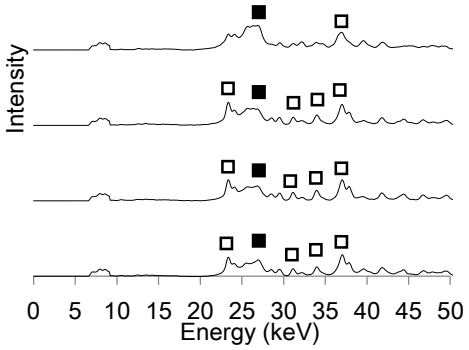
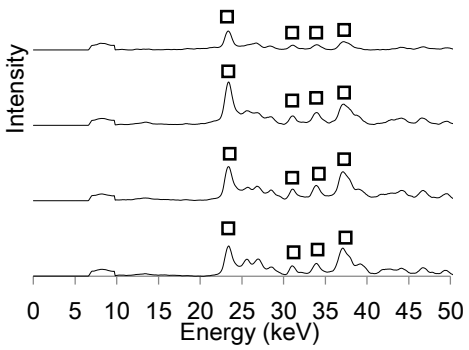
	Before Immersion	After Immersion
CT		
XRD		

Figure B-3 Dataset of 600°C for 12 hours

B.4 800°C

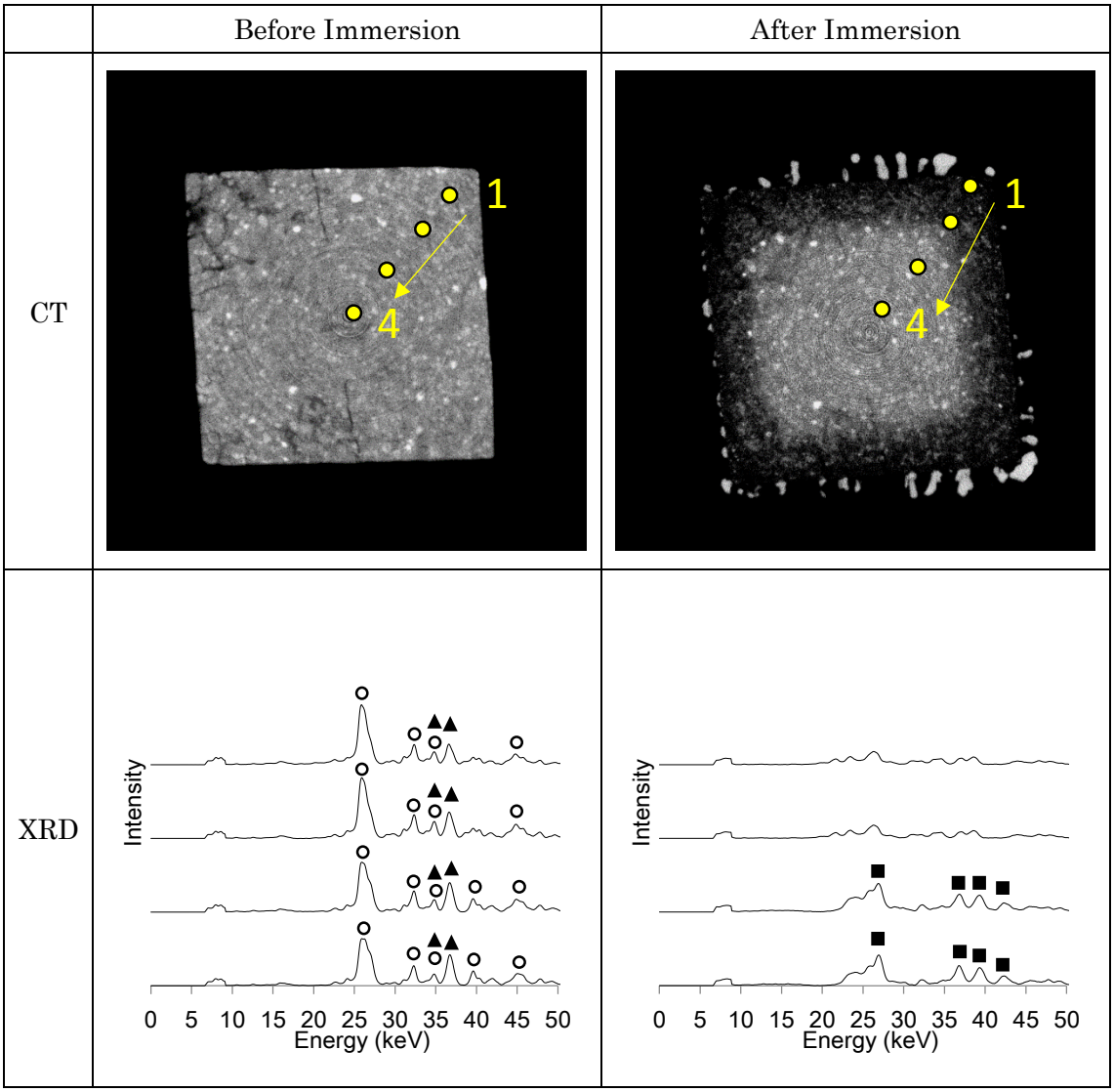


Figure B-3 Dataset of 800°C for 12 hours

APPENDIX C IMPROVEMENT OF CT-XRD SYSTEM

From the second half of 2017, the system was slightly changed to improve the image quality. Figure C-1 describes the comparison of cross section image obtained by old system and

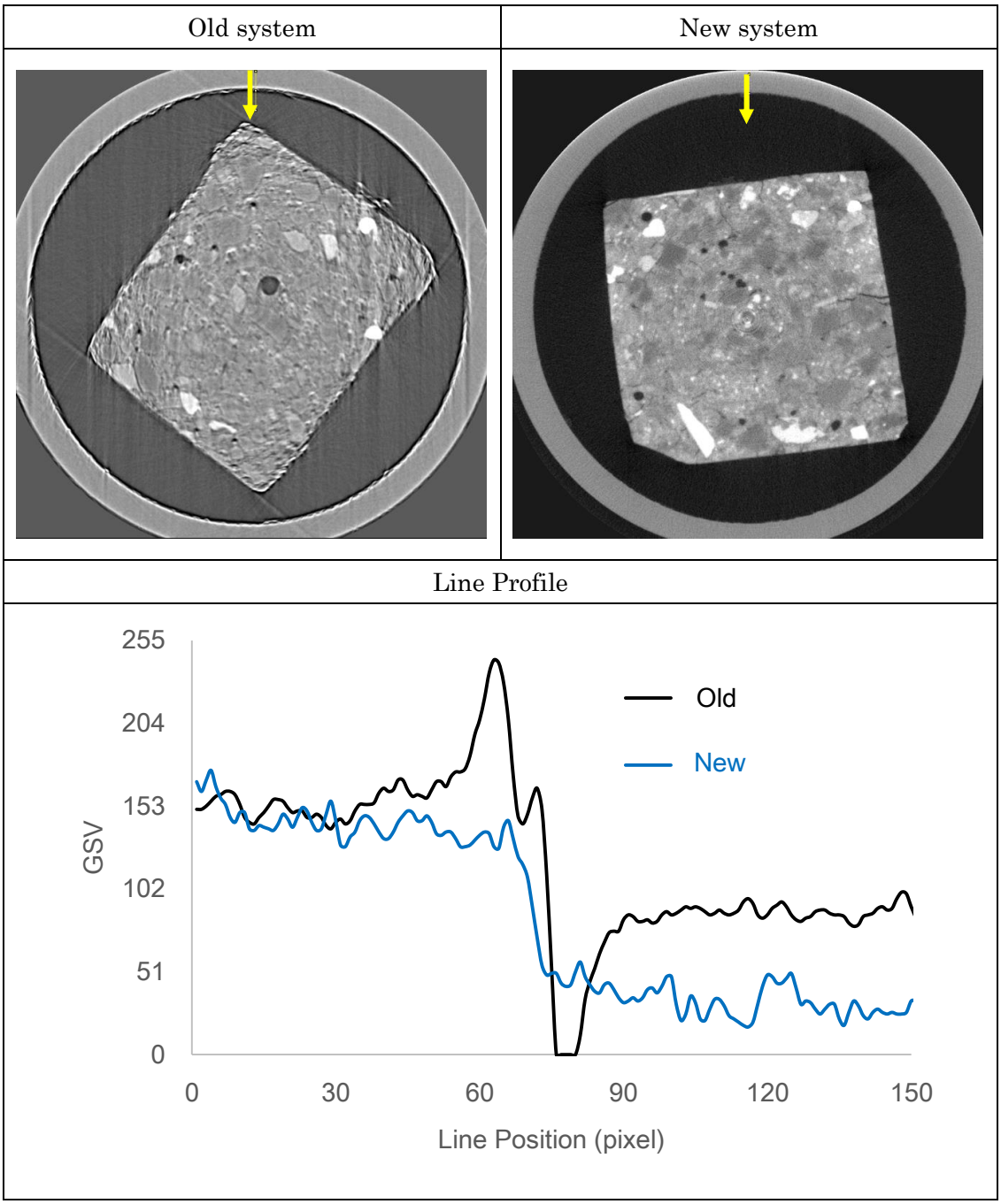


Figure C-1 Effect of changing system of the CT-XRD for CT measurement

new one. Fluctuation of GSV on edges can be reduced in new one's line profile.

From the first half of 2017, the height of Slit 1 was changed from 0.15 mm to 0.30mm. Moreover, the fixed diffraction angle between sample and detector was also changed from 10° to 5°. The effect of changing system of the CT-XRD for XRD measurement is shown in Figure C-2. The peak in profile obtained from new system (θ=5°) becomes sharper than old one (θ=10°).

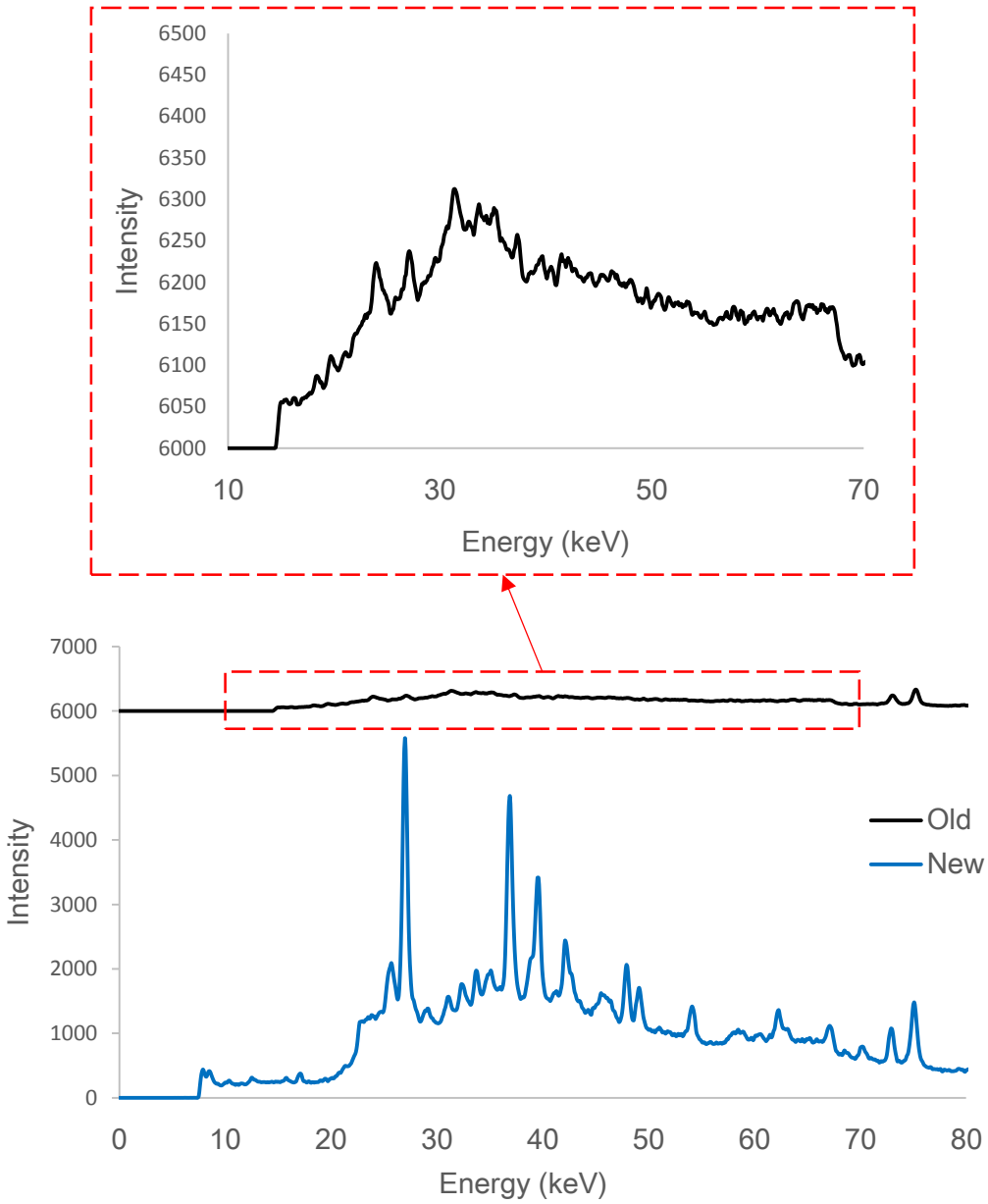


Figure C-2 Effect of changing system of the CT-XRD for XRD measurement

APPENDIX D EFFECT OF AGGREGATE ON CRACK BEHAVIOR BY HEATING

The research was conducted to investigate the alteration and crack behavior in microscopical view under high temperature using natural aggregate. Mortar sample was used with a water to cement ratio of 0.6 using tap water. Ordinary Portland cement was used with the density of 3.16 g/cm^3. The sand that was used in this specimen is aggregate produced in Shizunai-river. The particle size was adjusted to 0.3 mm or less. The above materials were weighed such that the aggregate volume ratio was 20 %. After mixing, the materials were molded into metal mold in the size of 40×40×160 mm. After 1 days, samples were demolded and cured into water. After 8 months curing, the bulk specimen was cut into the prism in the size of 2.5×2.5×5 mm for non-destructive integrated CT-XRD method followed by heating test described in the next section. Then, samples were attached to the specified aluminum jig.

Heating test was carried out using electric furnace with a temperature control program. Figure D-1 shows the temperature program in this experiment. The rate of temperature increase was set at 10 °C/min until target maximum temperature. The maximum temperature was maintained for 2 hours and the rate of heat decrease was also set at 10 °C/min. The target maximum temperature is 400, 600, 800, 1000 °C, respectively. Weight loss and length decrease were examined after extracting the sample. Weight was measured by using electronic balance which is measurable in the unit of 0.1 mg and length was measured by using micrometer which is measurable in the unit of 1 μm. The setup conditions were set same as Section 3.2.3. Figure D-1

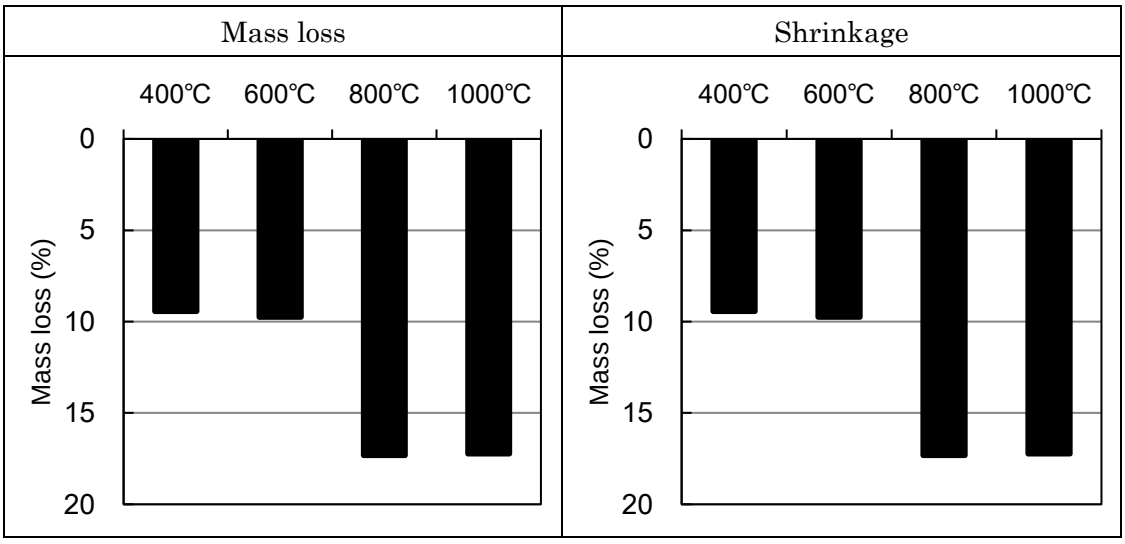


Figure D-1 Reduction ratio at each maximum temperature

shows the result of mass loss and shrinkage. It can be said that the mass loss is about 10 % at 400 and 600 °C, and about 17 % at 800 and 1000 °C. As for the shrinkage, the value is about 1.0 % at 400 and 600 °C. However, in case of 800 °C, the ratio is 3.8 %, and 4.7 % in case of 1000 °C, respectively.

Figure D-2 shows the cross sectional image in the center height of each specimen. These images show that void, clinker mineral, cement paste, and aggregate can be observed. Relatively large air voids are included, which indicates entrapped airs which was caught up during the beginning of hydration. Some unique aggregates can be seen representatively shown in 800 °C. These

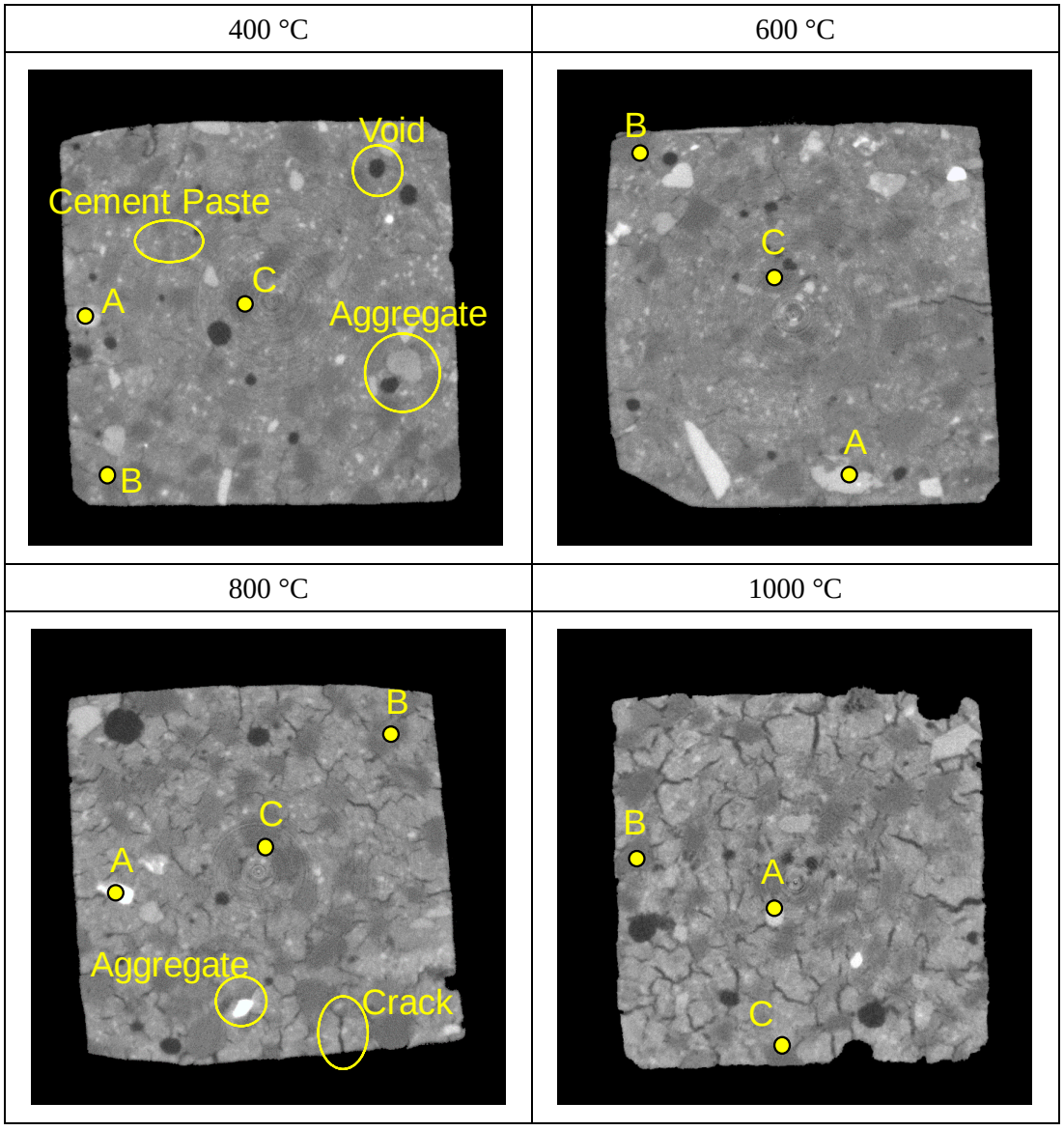


Figure D-2 Cross sectional images at center heights. The markers indicate the position of XRD measurement

aggregates can be considered as Hematite, which is one of the components of Shizunai-river sand. These are shown in white color because the density of Hematite is by far higher than that of Quartz, which is main component of the sand. As discussed in the results of XRD measurements, Hematite and Quartz were identified. Therefore, it can be said that the results are consistent. According to maximum temperature, a little amounts of cracks were observed at the outside edge of sample of 400 and 600 °C. However, many minute cracks can be observed inside of sample of 800 and 1000 °C. It is known that Quartz can be transitioned at 573 °C from α-phase to β-phase reversibly, which have an effect on expansion of volume by about 6 %. Therefore, it can be considered that these crack generation occurred inside the sample.

Figure D-3 indicates the GSV histograms of ROI for each sample. There is no significant difference between 400 and 600 °C. The peaks are found out at the value of 55 and 137, which corresponds to the peak of air and cement paste, respectively. In this experiment, the peak of Quartz is not shown clearly. This might be because a density of quartz has little difference compared with cement paste or the volume is as low as 20 %. As for 800 °C, the cement paste's derived peak spread to the higher value side. In case of 1000 °C, it can be said that the peak spread to further higher side. As discussed in the next section, the generation of Ferrite, Belite, and Lime was suggested at more than 800 °C, which has the about 1.0~1.5 higher density of those minerals than that of ordinary cement hydrate system. Therefore, these peaks are positioned at higher position.

The XRD profiles based on points indicated in Figure D-2 are shown below. The measured points are selected as Point A on characteristics point (like aggregate) and as Point B and Point C on cement paste. In case of 800 °C, Point A was selected on the aggregate with white color. Identification was carried out to compare the profile by subtracting the background from the

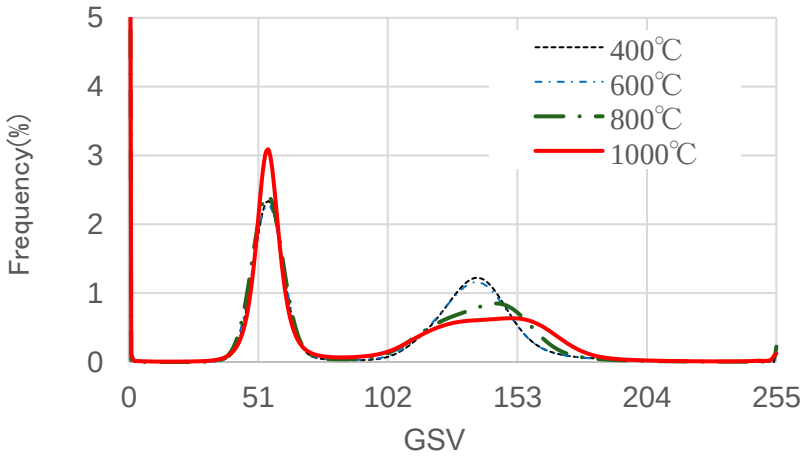


Figure D-3　GSV Histogram

obtained diffraction profile with the theoretical profile calculated by lattice constants of target minerals. Figure D-4 shows the XRD profiles of each sample. With regard to 400 °C, the peaks of quartz can be checked in Point A. From Point B and Point C, multiple peaks of Portlandite were observed. Therefore, it can be said that its decomposition was not observed because the maximum temperature is low and duration time was short. Some peaks of Quartz were also

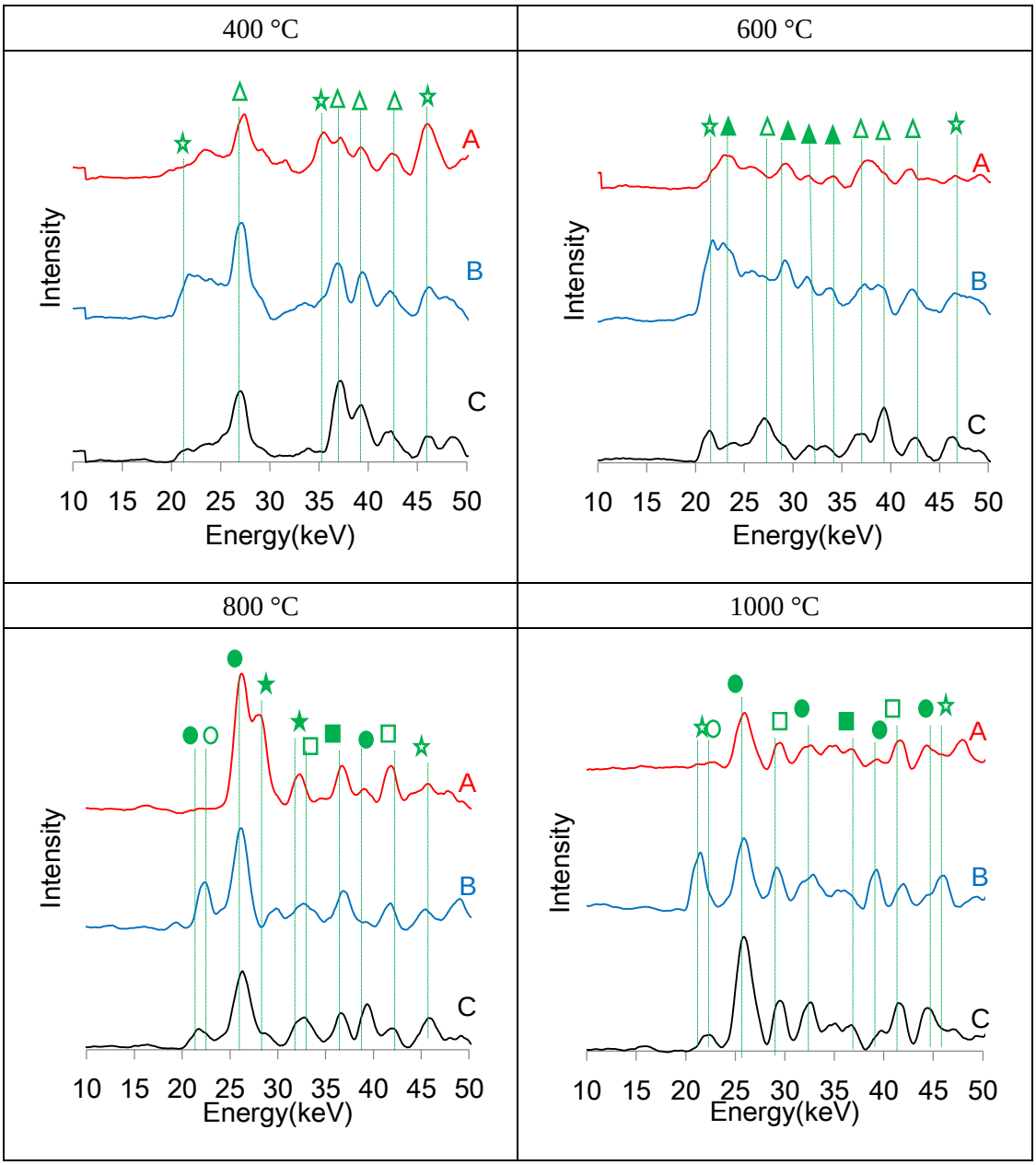


Figure D-4　XRD profiles of all samples by the CT-XRD
(△: Portlandite, ▲: Calcite, ○: C_3S, ●: C_2S, □: Lime, ■: C_4AF, ☆: Quartz, ★: Hematite)

observed in both Point B and Point C, which indicates that there exists aggregate in the ROI. As for 600 ℃, the profile of Point A has little peak of Quartz and many peaks of Calcite, which is similar to Point B. This indicates that there exists much amount of Cement paste in ROI. On Point C near the center of sample, the peaks of Portlandite are very significant. Thus, it implied that the decomposition of Portrandite progressed followed by the generation of Calcite at outside of sample. At 800 ℃ sample, the profile of Point A, which is positioned at white aggregate color, has both cement paste's derived peak and Hematite's peak. In the profile of Point B and Point C, there are the peaks of Belite, Lime, Ferrite and Alite. It can be considered that this result is derived from the decomposition of Portlandite and C-S-H. In the lower right corner, the profiles of 1000 ℃ are shown. The profile of Point A has significant much peaks of cement pastes, which are Belite, Lime, Ferrite, and Alite. On Point B and Point C, there are much peaks of above mentioned minerals with small peaks of Quartz.

Above discussed, the reason of peak shift as indicated in Figure D-3 confirmed the generation of Belite, Lime, Ferrite, and Alite, which is consistent with past researches.

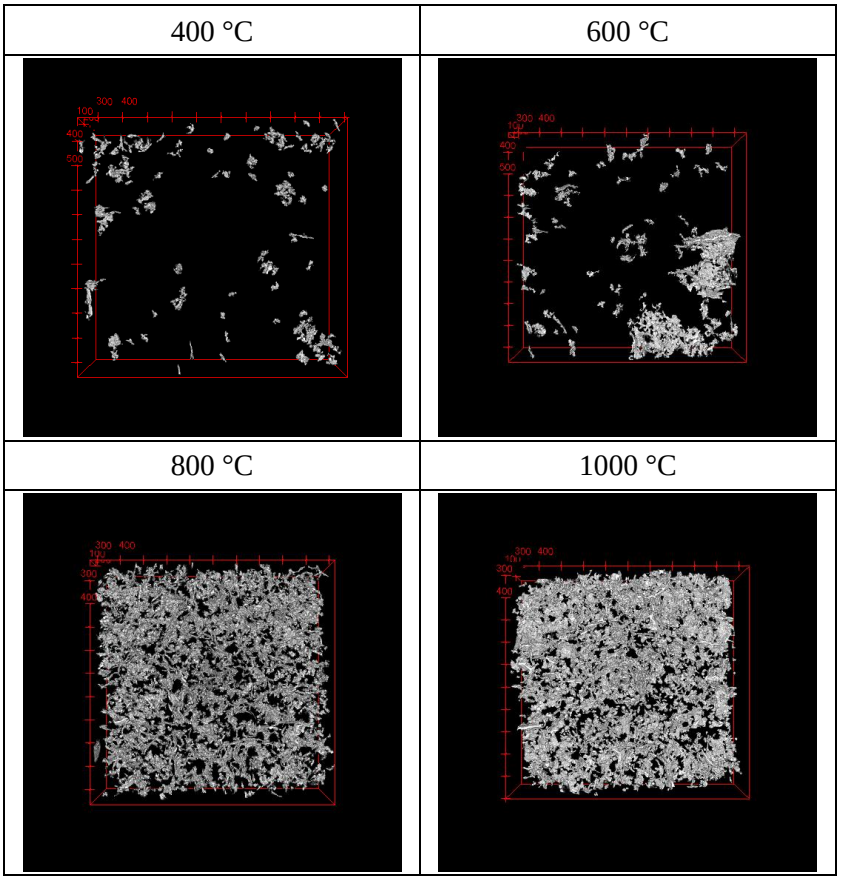


Figure D-5　Cross sectional images at center heights. The markers indicate the position of XRD measurement

Table D-1　Crack ratio and tortuosity

Sample	Crack ratio	Tortuosity	
		Maximum	Average
400°C	0.0011	2.40	1.35
600°C	0.010	2.45	1.26
800°C	0.034	3.35	1.31
1000°C	0.021	3.23	1.35

Extraction of crack area was carried out. Region of interest was processed into 1600×1600 in cross section, and 300 slices centering on the center height. Crack area was extracted by image processing from cross sectional image. Image processing was carried out to apply ImageJ and SLICE program. Figure D-5 shows that 3D images of extracted crack. Cracks are shown from cross sectional view. This indicates that crack is was observed at outside edge of sample of 400 and 600 °C. Moreover, crack area was distributed in all area at more than 800 °C. However, slightly more cracks can be observed in the sample of 800 °C than that of 1000 °C. Table D-1 shows the crack ratio and crack tortuosity. It indicates that crack ratio of 800 °C is higher than that of 1000 °C. It is derived from length reduction of 1000 °C is higher than 800 °C, which indicates that more shrinkage of cement paste occurs the closure of crack. Moreover, maximum value of tortuosity of 800 and 1000 °C is higher than that of 400 and 600 °C. However, there is no significant difference in the average value. Cracks were generated in both cement paste and surrounding aggregate. Cracks generated in surrounding aggregates contributes to higher maximum value. However, by far more minute cracks were generated in cement paste area. Therefore, it can be considered that each average value is almost all same.